DIPARTIMENTO DI INGEGNERIA INDUSTRIALE

Dottorato di Ricerca in Ingegneria Meccanica

XI Ciclo N.S. (2009-2012)

"Development of Solid Oxide Fuel Cell stack models for monitoring, diagnosis and control applications"

Ing. Dario Marra

Il Tutor

Ch.mo Prof. Cesare Pianese

Il Co-Tutor

Dr. Ing. Marco Sorrentino

Il Coordinatore

Ch.mo Prof. Vincenzo Sergi

Alla mia famiglia,
alle persone a me care
e a tutti coloro che
nonostante le difficoltà
perseguono i propri obiettivi

Table of Contents

Abstract ..... *vii*

Aknowledgements ..... *ix*

Nomenclature ..... *x*

List of Figures ..... *xiii*

List of Tables ..... *xviii*

INTRODUCTION *19*

Literature review on SOFC stack models **21**

Contributions **29**

Thesis overview **30**

CHAPTER 1 SOFC principle *31*

1.1 Working principle **31**

1.2 Cell material **33**

1.3 Fuel Cell Typologies **35**

CHAPTER 2 One-Dimensional SOFC Stack Modeling *37*

2.1 1-D model description **37**

2.1.1. Eletrochemical submodel 39

2.1.2. Simplified polarization losses sub-model 42

2.1.3. Conservation equations in co-flow configuration 43

2.1.4. Conservation equations in counter-flow configuration 50

2.2 IEA model validation **52**

2.3 Cross-validation **57**

2.3.1. Results 58

2.4 Diagnostic application **62**

2.4.1. Degradation model: parameter identification 62

2.4.2. Model setup 63
2.4.3. Results 64

CHAPTER 3Grey-box SOFC Stack modeling 69

3.1 Lumped model 69
3.1.1. Stack heat flows sub-models 73

3.2 Lumped model results 86

CHAPTER 4Black-box SOFC Stack modeling 91

4.1 Neural networks 91
4.1.1. Recurrent Neural Network 92
4.1.2. Neural Networks Learning approach 92
4.1.3. Optimal network dimension 95

4.2 Steady-state Neural Network model of HEXIS SOFC stack 96
4.2.1. Neural Network input selection 97
4.2.2. Steady-state Neural Network 101
4.2.3. Training and Test data sets definition 102
4.2.4. Results 106

4.3 Recurrent Neural Networks models of TOPSOE and VTT (HTC) SOFC stacks 112
4.3.1. Topsoe Stack RNN 112
4.3.2. VTT (HTc) Stack RNN 116
4.3.3. Results 120

CHAPTER 5Conclusions 125

CHAPTER 6APPENDIX 127

Fault diagnosis 127

6.1 Fault Tree Analysis 130

6.2 Fault Detection and Isolation process 132

References 135

Abstract

In the present thesis different SOFC stack models have been presented. The results shown were obtained in the general framework of the GENIUS project (GEneric diagNosis Instrument for SOFC systems), funded by the European Union (grant agreement n° 245128). The objective of the project is to develop "generic" diagnostic tools and methodologies for SOFC systems. The "generic" term refers to the flexibility of diagnosis tools to be adapted to different SOFC systems.
In order to achieve the target of the project and to develop stack models suitable for monitoring, control and diagnosis applications for SOFC systems, different modeling approaches have been proposed. Particular attention was given to their implementability into computational tools for on-board use. In this thesis one-dimensional (1-D), grey-box and black-box stack models, both stationary and dynamic were developed. The models were validated with experimental data provided by European partners in the frame of the GENIUS project.
A 1-D stationary model of a planar SOFC in co-flow and counter-flow configurations was presented. The model was developed starting from a 1-D model proposed by the University of Salerno for co-flow configuration (Sorrentino, 2006). The model was cross-validated with similar models developed by the University of Genoa and by the institute VTT. The cross-validation results underlined the suitability of the 1-D model developed. A possible application of the 1-D model for the estimation of stack degradation was presented. The results confirmed the possibility to implement such a model for fault detection.
A lumped gray-box model for the simulation of TOPSOE stack thermal dynamics was developed for the SOFC stack of TOPSOE, whose experimental data were made available in the frame of the GENIUS project. Particular attention was given to the problem of heat flows between stack and surrounding and a dedicated model was proposed. The black-box approach followed for the implementation of the heat flows and its reliability and accuracy was shown to be satisfactory for the purpose of its applications. The procedure adopted turned out to be fast and applicable to other SOFC stacks with different geometries and materials. The good results obtained and the limited calculation time make this model suitable for implementation in diagnostic tools. Another

field of application is that of virtual sensors for stack temperature control.
Black-box models for SOFC stack were also developed. In particular, a stationary Neural Network for the simulation of the HEXIS stack voltage was developed. The analyzed system was a 5-cells stack operated up to 10 thousand hours at constant load. The neural network exhibited very good prediction accuracy, even for systems with different technology from the one used for training the model. Beyond showing excellent prediction capabilities, the NN ensured high accuracy in well reproducing evolution of degradation in SOFC stacks, especially thanks to the inclusion of time among model inputs. Moreover, a Recurrent Neural Network for dynamic simulation of TOPSOE stack voltage and a similar one for a short stack built by HTc and tested by VTT were developed. The stacks analyzed were: a planar co-flow SOFC stack (TOPSOE) and a planar counter-flow SOFC stack (VTT-HTc).
All models developed in this thesis show high accuracy and computation times that allow them to be implemented into diagnostic and control tool both for off-line (1-D model and grey-box) and for on-line (NN and RNNs) applications. It is important noting that the models were developed with reference to stacks produced by different companies. This allowed the evaluation of different SOFC technologies, thus obtaining useful information in the models development. The information underlined the critical aspects of these systems with regard to the measurements and control of some system variables, giving indications for the stack models development.
The proposed modeling approaches are good candidates to address emerging needs in fuel cell development and on-field deployment, such as the opportunity of developing versatile model-based tools capable to be generic enough for real-time control and diagnosis of different fuel cell systems typologies, technologies and power scales.

Aknowledgements

I wish to address my special thanks to Prof. Cesare Pianese and Dr. Marco Sorrentino for their constant and essential support to my work during these years. They have represented and represent for me reference points that supported me even in difficult times. A special thanks goes to Prof Gianfranco Rizzo and Prof. Ivan Arsie for their help and their availability.
The results presented were obtained in the framework of the European Community's Seventh Framework Programme (FP7/2007-2013) for the Fuel Cells and Hydrogen Joint Technology Initiative under grant agreement n° 245128 (Project - GENIUS, GEneric diagNosis Instrument for SOFC systems). A thanks go to all the participants of the GENIUS project, particularly to Philippe Mocoteguy, as coordinator of the project; Jari Kiviaho, Antti Pohjoranta, Boris Iwanschitz, Andreas Mai, Kresten Juel Nikolaj Laut Jensen and Stefan Pofahl for their technical support and the data that they provided me for my PhD Thesis.
I want to thank my family for their constant presence, their love and support that have always given me and continue to give me.
The final thanks go to my “roommates” (staff and Ph.D. students) in the EPOLAB Laboratory of the Department of Industrial Engineering at University of Salerno.

Nomenclature

A	Electroactive area [cm^2]
AU	Air Utilization
AFC	Alkaline Fuel Cell
APU	Auxiliary Power Unit
ASR	Area Specific Resistance [Ωcm^2]
CPO	Catalytic Partial Oxidation
$DMFC$	Direct Methanol Fuel Cell
E_{Nernst}	Nernst ideal potential [V]
$\dot{E}$	Energy rate [W]
F	Faraday constant [C/mol]
FU	Fuel Utilization
G	Gibbs free energy [J/mol]
h	Molar specific enthalpy [J/mol]
j	Current density [mA/cm^2]
$\bar{j}$	Average current density [mA/cm^2]
j_0	Exchange current density [mA/cm^2]
j_{as}	Anode limiting current density [mA/cm^2]
j_{cs}	Cathode limiting current density [mA/cm^2]
K_{stack}	SOFC stack – lumped heat capacity [J/K]
l	Thickness [cm]
$\dot{m}_{air,ca,in}$	Cathode inlet air mass flow [g/h]
$\dot{m}_{CH_4,CPO,in}$	CPO inlet CH_4 mass flow [g/h]
$\dot{m}_{fuel,an,in}$	Anode inlet fuel mass flow [g/h]
$MCFC$	Molten Carbonate Fuel Cell
MSE	Mean Squared Error
N	Number of epochs
NN	Neural Network

n_e	number of electrons
$\dot{n}$	Molar flux [mol/s]
p_{H_2}	Hydrogen partial pressure [Pa]
p_{H_2O}	Water partial pressure [Pa]
p_{O_2}	Oxigen partial pressure [Pa]
PEMFC	Polymeric Electrolyte Membrane Fuel Cell
PAFC	Phosphoric Acid Fuel Cel
$\dot{Q}$	Heat flux [W]
R	Universal gas constant [J/mol/K]
$\dot{r}$	Reaction rate [mol/s]
SOFC	Solid Oxide Fuel Cell
t	Time [s]
T_{air}	Air Temperature [K]
T_{fuel}	Fuel Temperature [K]
T_{stack}	Stack Temperature [K]
V_{Act}	Activation losses [V]
V_{Conc}	Concentration losses [V]
V_{Ohm}	Ohmic losses [V]
V_s	Stack Voltage [V]
x_{CH_4}	Methane molar concentration [%]
x_{CO}	Monoxide molar concentration [%]
x_{CO_2}	Dioxide molar concentration [%]
x_{H_2O}	Water molar concentration [%]
x_{O_2}	Oxigen molar concentration [%]
y	Experimental data
$\hat{y}$	Network estimated output

Greek symbols

Δ	Change
α	Charge transfer coefficients

λ	Excess of air fed to the SOFC
θ	Neural Network-parameters vector [/]
σ	Ionic/electronic conductivity [S/cm]

Superscript

i	i-th computational element

Subscript

air	Air
an	Anode
ca	Cathode
cond	Conductive
conv	Convective
el	Electrolyte
fuel	Fuel
in	Inlet
out	Outlet
ox	Oxidation reaction
prod	Products
react	Reactants
s	Solid
stack	Stack

List of Figures

Fig. 1.1 – SOFC basic principle 32
Fig. 1.2 - Conductivities of major SOFC electrolytes as function of average operating temperature (Ormerod, 2003). 35
Fig. 2.1 – Cell computational discretization for counter flow configuration. 39
Fig. 2.2 – Discretized mass balance at the i-th element for co-flow configuration. 45
Fig. 2.3 – Energy balance at the i-th element for co-flow configuration. 47
Fig. 2.4 - Discretized mass balance at the i-th element for counter-flow configuration. 51
Fig. 2.5 - Energy balance at the i-th element for counter-flow configuration. 52
Fig. 2.6 – Comparison between stack temperature profiles in co-flow and counter flow configurations (case 1 of IEA validation) 56
Fig. 2.7 - Comparison between current density profiles in co-flow and counter flow configurations (case 1 of IEA validation) 56
Fig. 2.8 - Comparison between CH_4 molar faction profiles in co-flow and counter flow configurations (case 1 of IEA validation) 57
Fig. 2.9 – The average cell voltage estimated by the compared models. The x-axis refers to the simulation experiments of Tab. 2.4 and the model number given in the legend refers to either a metallic solid configuration (1) or a ceramic solid configuration (2). 59
Fig. 2.10 - The maximum cell temperature estimated by the compared models. The x-axis refers to the simulation experiments of Tab. 2.4 and the model number given in the legend refers to either a metallic solid configuration (1) or a ceramic solid configuration (2). 59
Fig. 2.11 – Example of current density profiles on the cell, estimated by the compared models, in conditions: current density 0.35

A/cm^2, fuel utilization 60%, inlet gas temperature 750 °C and ceramic solid phase. 60
Fig. 2.12 - Example of cell temperature profiles on the cell, estimated by the compared models, in conditions: current density 0.35 A/cm^2, fuel utilization 60%, inlet gas temperature 750 °C and ceramic solid phase. 60
Fig. 2.13 - Example of current density profiles obtained from simulation experiments in solid phase configuration (top) and in ceramic configuration (bottom) in the operating conditions: current density 0.35 A/cm^2, fuel utilization 60%, inlet gas temperature 750 °C. 61
Fig. 2.14 – Degradation parameter identification scheme 63
Fig. 2.15 - Cell resistivity spatial distribution in normal and faulty conditions for a global increase of electrolyte resistivity. 65
Fig. 2.16 - Cell temperature spatial distribution in normal and faulty conditions 66
Fig. 2.17 - Cell resistivity spatial distribution in normal and faulty conditions for a local increase of electrolyte resistivity 66
Fig. 3.1 – Lumped model control volume: 1° principle scheme. 70
Fig. 3.2 – Stack heat flows model scheme 73
Fig. 3.3 – Steady-state points selection in the data set 1 of TOPSOE stack 77
Fig. 3.4 – Comparison of heat losses model coefficient K_1 vs Time calculated by regression and by energy balance. 78
Fig. 3.5 - Comparison of heat losses model coefficient K_1 calculated by regression and by energy balance. 78
Fig. 3.6 - Comparison of heat losses model coefficient K_2 vs Time calculated by regression and by energy balance. 79
Fig. 3.7 - Comparison of heat losses model coefficient K_1 calculated by regression and by energy balance. 79
Fig. 3.8 - Comparison of heat losses model Q vs Time calculated by regression and by energy balance. 80

Fig. 3.9 - Comparison of heat losses model Q calculated by regression and by energy balance. *80*
Fig. 3.10 - Comparison of heat losses model Q vs Time in dynamic conditions calculated by regression and by energy balance on the data set 1 of TOPSOE stack. *82*
Fig. 3.11 - Comparison of heat losses model Q vs Time in dynamic conditions calculated by regression and by energy balance on the data set 1 of TOPSOE stack – time window [2000-8000] min. *83*
Fig. 3.12 - Comparison of heat losses model Q vs Time in dynamic conditions calculated by regression and by energy balance on the 2nd test round of TOPSOE stack – time window [12500-20000] min. *83*
Fig. 3.13 - Comparison of heat losses model Q vs Time in dynamic conditions calculated by regression and by energy balance on the data set 1 of TOPSOE stack – time window [2685-2775] min. *84*
Fig. 3.14 - Comparison of heat losses model Q vs Time in dynamic conditions calculated by regression and by energy balance on the data set 2 of TOPSOE stack, before introduction of coefficient proportional to ASR. *85*
Fig. 3.15 - Comparison of heat losses model Q vs Time in dynamic conditions calculated by regression and by energy balance on the data set 2 of TOPSOE stack, after introduction of coefficient proportional to ASR. *85*
Fig. 3.16 – Comparison between measured and simulated air temperature at cathode outlet in the data set 1 of TOPSOE stack. *87*
Fig. 3.17 - Comparison between measured and simulated air temperature at cathode outlet in the data set 1 of TOPSOE stack, time window [2000-8000] min. *87*
Fig. 3.18 - Comparison measured and simulated air temperature at cathode outlet between in the data set 1 of TOPSOE stack, time window [12250-14750] min. *88*

Fig. 3.19 - Comparison measured and simulated air temperature at cathode outlet between in the data set 1 of TOPSOE stack, time window [18300-20100] min. 88
Fig. 3.20 - Comparison between measured and simulated air temperature at cathode outlet in the data set 2 of TOPSOE stack. 89
Fig. 3.21 – Relative error between measured and simulated air temperature at cathode outlet in the data set 2 of TOPSOE stack. 89
Fig. 4.1 – NOE Recurrent Neural Network scheme. 92
Fig. 4.2 – Comparison between training and test error vs number of training iteration (adapted from Patterson, 1995). 95
Fig. 4.3 - a) stack sketch; b) metallic interconnect (MIC); c) electrolyte supported cell (ESC) (Mai et al., 2011). 97
Fig. 4.4 - Stack Voltage vs Current Density at different operating hours (Training_set, VI profiles). 100
Fig. 4.5 - Sketch of the input-output model; the structure of the neural networks is described into section 2. 101
Fig. 4.6 - NN MSE of training-set and early stopping test-set vs number of epochs. 102
Fig. 4.7 - VI curves and long term Voltage data (Training_set). 105
Fig. 4.8 - Comparison between measured and simulated stack voltage on Test_set_1 (VI curves). 107
Fig. 4.9 - a) Comparison between measured and simulated stack voltage for Test_set_1 (VI curves) at 2353 hours; b) Comparison between measured and simulated stack voltage for Test_set_1 (VI curves) at 3433 hours. 108
Fig. 4.10 - Comparison between measured and simulated VI profiles for the Training_set. 109
Fig. 4.11 - Comparison between measured and simulated stack voltage for Test_set_2 (VI curves). 109
Fig. 4.12 - Comparison between measured and simulated stack voltage for Test_set_2 (VI curves) at 2136 hours. 110

Fig. 4.13 - Comparison between measured and simulated stack voltage for Test_set_3 (long term). *110*
Fig. 4.14 - Comparison between measured and simulated stack voltage for Test_set_4 (long term). *111*
Fig. 4.15 - Topsoe stack voltage (experimental output). *114*
Fig. 4.16 - Topsoe stack voltage splitting into training and test set. *114*
Fig. 4.17 - Topsoe RNN inputs. *115*
Fig. 4.18 - Schematic of Topsoe RNN architecture. *116*
Fig. 4.19 - Schematic of VTT (HTc) RNN architecture. *117*
Fig. 4.20 - VTT (HTc) stack voltage (experimental output). *118*
Fig. 4.21 – VTT (HTc) stack voltage splitting into training and test set. *118*
Fig. 4.22 - VTT (HTc) RNN inputs. *119*
Fig. 4.23 - Comparison between measured and simulated TOPSOE stack voltage (training set). *121*
Fig. 4.24 - Comparison between measured and simulated TOPSOE stack voltage (test set). *121*
Fig. 4.25 - Comparison between measured and simulated TOPSOE stack voltage (test set), time window [4000-6000] min. *122*
Fig. 4.26 - Comparison between measured and simulated VTT (HTc) stack voltage (training set). *122*
Fig. 4.27 - Comparison between measured and simulated VTT (HTc) stack voltage (test set). *123*
Fig. 4.28 - Comparison between TOPSOE and VTT (HTc) load time history investigated in the 2nd test round *123*
Fig. 6.1 – Fault Diagnosis scheme. *128*
Fig. 6.2 - Fault Tree example developed through a top-down approach (refer to Tab. 6.1 for the list of symbols). *132*
Fig. 6.3 – Fault Signature Matrix. *133*
Fig. 6.4 – Fault Detection and Isolation process scheme. *134*

List of Tables

Tab. 1.1 – Main features of the mayor fuel cell typologies (sources: Moran and Shapiro, 2004; Fuel Cell Handbook, 2002; Rajashekara, 2000; Larminie and Dicks, 2003, Topsoe, 2002 *36*
Tab. 2.1 – Operating conditions for IEA validation. *53*
Tab. 2.2 – One-dimensional model validation with IEA benchmark in counter and co-flow configurations (case 1). *54*
Tab. 2.3 - One-dimensional model validation with IEA benchmark in counter and co-flow configurations (case 2). *55*
Tab. 2.4 – Simulation experiments conditions *58*
Tab. 2.5 – 1-D model setup for degradation parameter identification. IEA Benchmark (Braun, 2002) *64*
Tab. 2.6 - Values of K for a global and local increase of 20% of *67*
Tab. 3.1 – Experimental data sets provided by TOPSOE *72*
Tab. 3.2 – Heat flows model parameters identified. *75*
Tab. 4.1 - Main specifications of the 5-cells test rig. *97*
Tab. 4.2 - Features of the experimental data-sets used for neural *105*
Tab. 6.1 - Fault Tree symbols and related descriptions. *131*

Introduction

Solid Oxide Fuel Cells have gathered a large attention in the last decades, mainly for the potential applications as stationary power generators and APUs for transportation use (ground, marine, air). SOFC attractiveness lies on both the high energy conversion efficiency and the zero toxic emission levels (only the CO_2 released by the hydrogen production process is a concern). Other advantages are: modularity, fuel flexibility and low noise (Sorrentino et al., 2009 (a); Huanga et al., 2009; Singhal and Kendall, 2004). Moreover, the high working temperatures provide additional positive features, such as potential use of SOFC in highly efficient cogeneration applications. SOFCs are also suitable for internally reforming the fuel (e.g. natural gas, propane, methanol, gasoline, Diesel, etc.), thus making it possible to avoid the adoption of both highly sophisticated, expensive external reformer and to simplify fuel storage (Sorrentino et al., 2008).

The big challenges to promote the diffusion of SOFC-based energy conversion systems are mainly associated to production costs and durability. The achievement of these targets will surely contribute to promoting the technology and finally starting a mass production phase. Besides costs and performance, long-term stability is an important requirement for the commercial application of the SOFC technology. For stationary applications the commercial lifetime requirement is generally more than 40,000 h. In comparison, up to a 20,000 h lifetime with more frequent thermal cycles is required for auxiliary power units in transportation applications (Braun, 2002). However, these lifetime requirements have not been met yet: SOFC system prototypes still suffer from a low reliability of both the fuel cell itself and the complete system.

The state of health of the system is currently difficult to evaluate, because SOFC operating conditions lead to a variety of degradation mechanisms that weigh upon system lifetime. For the stationary applications, the chemical instability at the interfaces is one of the key issues, whereas the thermo-mechanical instability is important in the transportation applications because of frequent thermal cycles (Larmnie and Dicks, 2003). It is therefore essential to increase the understanding in SOFC systems degradation and faulty mechanisms (Arsie et al, 2010 (a)).

To guarantee the safe operation of fuel cell systems and to support the successful deployment of SOFC, it is necessary to make systematic use of specific computational tools for developing suitable control and diagnostic strategies.
The final aim of an SOFC fault diagnosis activity is to reach the required criteria for a commercial application, which, besides high lifetime and performance, include high reliability and safety and suitable costs as well.
The desire to guarantee system availability and reliability is the reason why Fault Diagnosis methodologies are applied to several different fields, ranging from passenger cars and trucks to aircrafts, trains and even to stationary systems, such as power and chemical plants (Isermann, 2004; Rizzoni et al. 2008)
With particular regard to diagnostics, designers and users always pay interest in preventing the occurrence of faults of any mechanism, machine or energy conversion system. To this end, several approaches can be taken, the most obvious of which is to stop the system whenever an abnormal functioning is observed, i.e., a fault is determined as a difference in the performance of the system from its expected behavior. The ability to detect the occurrence of any fault, and identify its cause, is a critical task.
The basic idea of the present thesis is to develop SOFC stack models of different typologies and with different model approaches to be Implemented into model-based diagnostic and control tools. The model-based fault diagnosis (described in the Appendix) is based on the comparison between the measured variables of a real system and those simulated by a model or a system of models that reproduce the real system under nominal conditions, without fault or malfunction. The comparison can be done in real time (on-line diagnosis) or not in real time (off-line diagnosis). The mathematical models for system monitoring require rapid calculation time and high accuracy in the simulations. In the case of on-line diagnosis calculation time must be less than the actual times, in the case of off-line diagnosis calculation times can be higher. A similar argument is made for model-based control applications. For diagnostic and control applications a fundamental aspect is represented by the models of the monitored system. In this thesis, different models of Solid Oxide Fuel Cell stacks are presented. The developed models have different physical content, with different complexity. Three types of models were analyzed: 1-D model, lumped grey-box model and black-

box models. The 1-D models have the dual characteristic of being able to be used in off-line diagnostic applications, as presented in CHAPTER 2, but can also represent a model generator of virtual experiments for the development of models with lower physical content (lumped models, black -box models), in which case one speaks of hierarchical approach (Sorrentino 2006, Sorrentino et al., 2008). In the next section an extensive literature research for SOFC stack models developed is performed.

Literature review on SOFC stack models

In the past decades, a great number of researchers investigated on SOFC modeling and on the simulation of internal process making use of physical representations. The models range from zero-dimensional (0-D) to three-dimensional (3-D) with different features and point to different research objectives. From the viewpoint of model function, 2-D and 3-D modeling is typically concerned with the cell and stack design issues while 0-D and 1-D modeling is aimed at control purposes (at system-level) such as prediction of both the transient and steady-state performance of fuel cell/stack and establishing the optimal operating condition (Braun, 2002). Moreover, high dimensional models require information about material properties or electrochemical parameters that are not always available or might be difficult to determine. Even so, high dimensional models are still helpful to learn the operation behaviour of fuel cells of different geometry and very useful for creating training data for black-box modeling.

Physical models are mainly based on the knowledge of physic-chemical characteristics (electrically, chemically and kinematically), thus also called as “white” models. They presents a high generalizability level that enables modeling SOFC stacks of different geometric features, but require a high computational effort. In contrast, there is another approach only based on experimental database (no requirement for any physical property), known as the black-box modeling. Black-box models are developed particularly for control-oriented applications, i.e. system monitoring, online control and diagnosis. Nevertheless, the high dependency upon experimental data makes these models less generalizable. Finally, grey-box modeling are partially physical and

partially empirical, falling in between white and black-box approaches.
For the research target of the present thesis (i.e. diagnostic and control applications) low dimensional models (0- and 1-D) are more appropriate due to the less computational time in comparison with the high dimensional ones (2- and 3-D). Therefore the literature review on SOFC stack models was focused on 1-D, 0-D (grey-box) and black-box models.

1-D SOFC stack models

In 1-D model, the fuel cell is usually treated as a set of layers including interconnects, air channel, electrodes, electrolyte and fuel channel (Bove and Ubertini, 2008). Both gas composition and flow rate in each channel are assumed to be constant and their mean values are used in the simulation. For planar SOFC, the main dimension corresponds to the gas channel and the direction is determined by the gas flow. It is necessary to note that the fuel cell with cross-flow design cannot be simulated by 1-D models. For tubular SOFC, the kept dimension is usually the tube axis which coincides with the direction of the fuel and oxidant flow (Bove and Ubertini, 2006).
Magistri et al. (2004) built a one-dimensional model for tubular SOFC, where the cell coordinate x is the axis of the tube and its origin corresponds to the bottom of the cell. The main hypotheses of the single cell model are: 1) the cell is adiabatic, 2) the cell voltage is uniform and all the chemical reactions within the anodic stream are at equilibrium, 3) the electrochemical reaction of H_2 is taken into consideration; the electrochemical reaction with CO is neglected. The cell model includes: electrochemical performance, equilibrium of reforming and shifting chemical reactions, mass balances at the anode and cathode, energy balances of gases flows, energy balance of the tube and of the solid positive-electrolyte-negative (PEN) structure. In the paper, the 1-D model was described and the results were compared to the 0-D model simulation proposed by Costamagna et al., (2001). In both models, the input data are: geometrical characteristics, operating conditions, inlet flow conditions and gas and material properties. The models comparison showed that the temperature inside the stack was not uniform and, although the average value was acceptable, the maximum values were too high.
In Gubner et al., (2003, 2005) a so-called dynamic behaviour model of an SOFC was developed and verified. The model was capable of

reproducing the I-V-behaviour and the temperature distribution in the gas flow direction inside a cell operating under either co- or counter-flow mode. It was found to be sufficiently accurate for rapid system simulation (Gubner et al., 2006). The model enabled, e.g., designing the gas flow rates according to the maximum drawn current density and thereby to prevent overheating of cell.

Aguiar et al. (2004) developed a 1-D dynamic model for anode supported intermediate temperature planar SOFC with direct internal reforming. This model predicted the SOFC characteristics both in steady-state and in transient operations. It is based on a mass and energy balances and coupled to an electrochemical model. For the mass balance the molar flux in the gas channels in the flow direction was considered. In the fuel channel, three reactions are taken into account: 1) methane steam reforming; 2) water gas-shift; 3) and hydrogen electrochemical oxidation. In the air channel only the reduction reaction of O_2 was considered. In the energy balance were included: the released heat from electrochemical reactions and Ohmic losses; the convective heat transfer between cell components and gas streams; and the in-plane heat conduction through cell components. The thermal flows between the PEN and the interconnect components were supposed to be conductive and radiate. However, in the gas channels, they were assumed to be convective in the gas flow direction and from the gas channels to the solid parts (perpendicular to flow direction).

Jiang et al. (2006) set up a 1-D dynamic model for a tubular SOFC with external reforming. The cell was divided into elements along the flow direction. For each element, in the 4 control volumes (CVs) separated along perpendicular axis: the fuel, the solid, the reaction air and the preheated air CVs. Several assumptions were made for the thermal model: 1) for every element, the temperature within each CV was uniform; 2) the radiation and the conduction heat transfer were not taken into account; 3) the convective heat transfer was assumed as the only cause of the temperature gradient in the gas streams. The heat generated for the reactions (shifting, reforming and electrochemical) and the Ohmic losses were computed. The cell voltage at each element was uniform. An equivalent circuit was built to evaluate the influence of the current path length to the Ohmic loss. This model was capable of predicting SOFC characteristics in both the steady and the transient conditions and showed a good reliability. Results from the model showed that high pressure

could improve the cell performance whereas higher operating temperature reduced both the Nernst potential and the irreversible losses (Ohmic, activation and concentration).

Sorrentino (2006) developed a 1-D steady-state model for co-flow planar SOFC. The model was divided into three sub-models: 1) mass balance; 2) energy balance; 3) voltage. The model was based on the control volume approach, according to which the cell was discretized in CVs in the flow direction and divided into three layers: anode channel, cathode channel and cell (solid layer). The cell was assumed to be isopotential and the pressure drop across the fuel and air channels was neglected. The raditive heat transfer and the heat conduction in the solid layer were neglected and the stack was assumed to be adiabatic. The heat convection between solid layer and gas streams and the energy transfer due to the reactants and products were considered dominant in the energy balance. The model showed a good accuracy in the simulation of SOFC states and variables. It was adopted to generate SOFC stack data to be used in a hierarchic modeling approach for control-oriented applications (Sorrentino et al., 2008).

Cheddie et al. (2007) upgraded a 0-D real time model to a dynamic 1-D model in order to predict more accurately the temperature and pressure variations along the gas flow direction. The real time capability was maintained by setting up several simplifications: the current density distribution was considered uniform and there was no need to compute the cell current iteratively, thus resulting in a reduction of computational effort. The overpotentials at each node were replaced by the average one across the cell. It was assumed that neither time lag nor dynamic transient occurred in the voltage change after a current variation, so the transient states were not taken into account. The gas concentration was considered dependent only on partial pressure rather than both pressure and temperature. In thermal model, the heat generation was assumed to occur in the PEN only. The heat conduction was negligible in the fluid phase due to the fact that the thermal conductivity is much higher in the solid regions than in the fluid phases. The 1-D model with 21 nodes was proven to require 3.8 ms of computational time for each iteration. The model validation showed that the limiting assumptions did not lead to the significant simulating difference when comparing with a more comprehensive 1-D model without these assumptions.

Kang et al. (2009) modified a 1-D dynamic model for a planar SOFC with

internal reforming by integrating two simplifications: 1) the PEN, interconnects and gas channels were integrated together along the perpendicular direction, that is, the SOFC is considered to have only one temperature layer; 2) the current density distribution is considered to be uniform within the SOFC, and the cell voltage is determined by the average gas molar fractions and cell temperature. These two simplifications are similar to the assumptions in Cheddie's modeling and by introducing them, the SOFC model was greatly simplified in form.

Grey-box SOFC stack models

The main purpose of the 0-D (grey-box) modeling is to develop model-based tools aiming at optimal design, management, control and diagnosis of SOFC units destined to a wide application area (Sorrentino et al., 2009 (a)). These models are suitable for massive use when the main characteristics of the system are already available. Therefore the lack of some physical knowledges (i.e. space description) is compensated by introducing other information such as empirical data. Therefore grey-box models mix phenomenological description with simplified assumptions and practical information In lumped models spatial variations are not taken into account (the transformations are considered to define output variables from input ones). In such an approach, the single elements, for instance, compressors, heat exchangers, fuel reformer, partial oxidizers, and contaminant removal apparatus are simulated through independent sub-models (Bove et al., 2006). Furthermore, they allow being easily calibrated and modified for new developed materials.
The grey-box approach is based on a priori knowledge concerning the process and on the mathematical relations which describe the behavior of the system. The starting point is a specific model structure based on physical relations. The construction procedure of a grey-box model based on mathematical relations can be divided into different sub-tasks: basic modeling, conduct experiment of the process, calibration and validation (Sohlberg et al., 2003). In order to optimize design, control and diagnosis of SOFC systems, with particular regard to the management of energy and mass flows during system start-up and load changes, it is important to simulate SOFCs in transient conditions. The development of these models should meet the compromise between satisfactory accuracy and affordable computational burden. The above compromise can be easily

achieved by 0-D (i.e. lumped) modeling approaches (Bhattacharyya et al., 2009).

Costamagna et al., (2001) described a hybrid system where the SOFC was simulated with the 0-D model approach. The balance equations were written as macroscopic balances, in form of finite equations. The equations expressed a balance between inlet and outlet flows of mass and energy in each component of the system; under suitable assumptions, they allowed the evaluation of the average values of the physical-chemical variables of each components and the electrochemical performance of the group itself.

In Campanari's 0-D SOFC model (Campanari, 2001), the cell voltage was a function of the current density, the operating temperature and pressure as well as the reactants and product composition.

Bove et al. (2005) built a macro model in which the Ohmic polarization depends upon the material properties only. The open circuit voltage and the activation polarization were related to gas concentration while the concentration polarization was ignored. The mean current density was regarded as an input variable.

Ferrari et al., (2004) and Magistri et al., (2006) made a transient analysis of hybrid system based on SOFC. This system was mainly composed of three parts: the stack; the anodic recirculation system with fuel feeding and the cathodic side (air side) where turbo-machinery; and heat exchangers. These researches allowed a deep investigation of the Fuel Cell Stack integrated with reformer and post-combustor models.

An Interesting lumped approach was followed by Sedghisigarchi and Feliachi (Sedghisigarchi et al., 2004 (a)) for control and stability enhancement of SOFC-based distributed generators (Sedghisigarchi et al., 2004 (b)). Nevertheless, in Sedghisigarchi et al., (2004 (a)) average cell temperature was assumed as state variable, thus not allowing to provide some basic information for balance of plant analysis, such as temperature of exhaust gases.

Sorrentino et al., (2008) proposed a hierarchical modeling approach to derive a control-oriented lumped model of planar SOFC. The model proposed is capable of simulating temperature and voltage dynamics as function of the main operating variables (i.e. current density, fuel and air utilizations, inlet and outlet temperatures) accurately. The contribution of (Sorrentino et al., 2008), differently than (Sedghisigarchi et al., 2004 (a)), does take into account temperature variation across the channels, thus

being suitable to perform, at low computational cost, accurate balance of plant analyses, including heat exchangers sizing (Bhattacharyya et al., 2009). Thus, Sorrentino and Pianese (Sorrentino et al., 2009 (a)) proposed to extend the lumped approach presented in (Sorrentino et al., 2008) to the modeling of a fully integrated SOFC-APU (i.e. auxiliary power unit). This latter contribution was also proven to be valid for the development of model-based diagnostics tools for mobile SOFC APUs (Sorrentino et al., 2009 (a)).
The 0-D approach was also applied to transient modeling of tubular SOFC by Hajimolana et al., (2009), to develop suited strategies aimed at controlling voltage and cell-tube temperature by properly acting on both temperature and pressure of the inlet air flow.
Sorrentino and Pianese, (2009 (b)) presented a grey-box model of a SOFC unit. The core part of the model is the fuel cell stack, made of planar co-flow SOFCs and surrounded by a number of auxiliary devices, namely air compressor/blower, regulating pressure valves, heat exchangers, pre-reformer and postburner. As a consequence of low thermal dynamics characterizing SOFCs, a lumped-capacity model is proposed to describe the response of fuel cell and heat exchangers to load change.

Black-box SOFC stack models

Most of existing models (1-D, 0-D) are based on physical conversion laws and governing equations (Wang et al., 2011; Yakabe et al. 2001; Recknagle et al. 2003; Xue et al. 2005). Although being useful for design analysis and optimization of SOFC, they are too complex for control and diagnosis of SOC system. This drawback impelled some researchers to attempt black-box methods (Arriagada et al., 2002; Chakraborty, 2009; Entchev et al., 2007; Goldberg, 1989; Huo et al., 2006; Huo et al., 2008 Jang, 1993; Milewski et al., 2009). The black-box are input-output (i.e. mapping) models, derived through statistical data-driven approach. Contrary to physical models, they are not based on explicit physical equations but use large databases with experimental data, which represent the behaviour of the system as function of different operating, control and state variables. Any black-box model is built without exploiting any physical law but use only a set of input-output pairs for training procedure is used, instead. Black-box models range from classical regression based approaches to complex artificial intelligence based ones (e.g. Neural

Network). It has been demonstrated that the black-box models based on artificial intelligent approaches are very suitable for non-linear systems (Patan, 2008). However, such models require a large amount of experimental data (i.e. training examples), which should well represent the behaviour of the system; therefore, the experimental burden for collecting meaningful data may become excessive. Although the experimental load is the main drawback of artificial intelligence-based modeling techniques, their intrinsic high accuracy represents the most attractive characteristic. These two opposite features lead to the main trade-off to deal with when approaching the modeling problem to be solved.

Arriagada et al. (2002) proposed a non-linear fuel cell model by using artificial neural networks (ANNs) for evaluating SOFC performance; their model is a two-layer feed-forward network whose outputs are air flow, current density, temperatures of outlet air and fuel, average solid and reversible voltage. The model was trained via backpropagation algorithm with a reduced amount of input and correct output data pairs generated by a physical cell model. Comparing the outputs of the ANN model with that of the physical model, the average values of the errors are well below 1% and the maximum below 4%. Besides the accuracy, the ANN models are much faster and easier to use and suitable for the generation of performance maps.

Milewski et al. (2009) used the same ANN structure of Arriagada et al. (2002) to simulate the SOFC behaviour (they exploited experimental data for training and testing process). This SOFC model predicts the output cell voltage making use of 9 input parameters (current density, cathode inlet O_2 and N_2 flow densities, anode H_2 and He flow density, anode thickness, anode porosity, electrolyte thickness and electrolyte temperature). A hyperbolic tangent sigmoid transfer function was used as the neuron activation function in the first layer, whereas a linear transfer function was used in the output layer. The testing results show that the ANN can be successfully used in modeling the single solid oxide fuel cell. However, its practical development suffered from some drawbacks such as the existence of local minima in the cost function to be minimized during parameter identification and over-fitting.

Contributions

In the present Thesis different models of SOFC stacks are presented. The models are developed with the purpose of being implemented into diagnosis and control applications for SOFC systems. For this reason, the modeling approach adopted is control-oriented type and 1-D, grey-box and black-box models, both stationary and dynamic have been developed. Specifically, the following models have been developed:

1. 1-D stationary model of a planar SOFC in co-flow and counter-flow configurations. The model has been derived from a 1-D model developed by the University of Salerno (UNISA) Sorrentino, (2006). The model has been cross-validated with similar models developed by the University of Genoa (UNIGE) and by the institute VTT of Espoo (Helsinki, Finland).
2. Grey-box model for the simulation of the thermal dynamic of a planar co-flow SOFC stack produced by TOPSOE.
3. A black-box model based on a steady-state neural network to simulate the stack voltage of a radial co-flow SOFC stack produced by HEXIS.
4. Black-box models based on recurrent neural networks to simulate the stack voltage of two SOFC stacks: one produced by TOPSOE and another one produced by HTc and tested by VTT.

The purpose of this thesis is to give an overview of the models and methodologies adopted for control and diagnosis applications. The models developed have been validated with experimental data provided by European manufactures. The research activity has been conducted as part of the GENIUS project, funded by the European Union. The objective of the project is to develop diagnostic tools and methodologies for SOFC systems. In the general framework of the GENIUS project this thesis is part of the development of mathematical models aimed at the definition of model-based diagnosis.

Thesis overview

The present thesis is structured as follows:

CHAPTER 1: SOFC principle and different fuel cell technologies and materials description.

CHAPTER 2: One-dimensional stack model description and cross-validation with similar models.

CHAPTER 3: Development and experimental validation of a grey box lumped model for stack thermal dynamic simulation.

CHAPTER 4: Development and experimental validation of black-box stack models based on Neural Network and Recurrent Neural Network.

CHAPTER 5: Conclusions.

CHAPTER 6 Appendix: Description of the Fault Diagnosis technique based on *Fault Tree Analysis.*

CHAPTER 1 SOFC principle

1.1 Working principle

Fuel cells are electrochemical devices capable of converting the chemical energy held by a hydrogen-rich fuel into electricity. Such conversion is direct, in that no intermediate combustion occurs (Rajashekara, 2000). Fuel cell working principle was discovered by Friedrich Schönbein, who found the fuel cell principle in 1838. Based on Schönbein publication Grove started his research and built the first fuel cell in 1839 (Larminie and Dicks, 2003). With referenc to SOFC, a single cell consists of three main components: an anode, a cathode and a solid electrolyte separating the two electrodes. Oxygen and hydrogen (i.e. the reactants) are supplied to cathode and anode, respectively (see Fig. 1.1). Under electrical load, at the cathode surface the presence of perovskite catalyst enables oxygen ionization (Eq. (1.1)). The solid electrolyte allows the flux of oxygen ions to the anode, where they electro-oxidize hydrogen, thus releasing heat, water and electrons (Eq. (1.5)). Since electrolyte material ensures quasi-zero electronic conductivity, electrons are forced to flow through interconnect and external load towards the cathode, thus closing the electrical loop. In a SOFC the oxygen ions are formed at the cathode where the oxygen of the supplied air is reduced, whereas at anode hydrogen rich gas is oxidized releasing electrons and water (Eq. (1.2)), as sketched in Fig. 1.1. At the anode hydrogen rich gas must be supplied (any gas composition is tolerated by the anode materials except sulfur compounds), in case of methane fuel, for example, in the presence of steam must be considered other two reactions at the anode: steam-reforming (Eq. (1.3)) and water-gas shift (Eq. (1.4)) reactions. This feature allows the use of any reformate gas from either methane or liquid fuels, therefore the gas composition may affect the performance of the cell. Another distinctive characteristic of SOFC is the high operating temperature (usually > 700°C), which represents a relevant feature allowing the use of these systems for cogeneration of heat for practical applications. On the other hand, the high temperatures involved do not

allow tight transient operations. This entails changes in the thermal regime, which in turn may cause mechanical stresses in the materials.

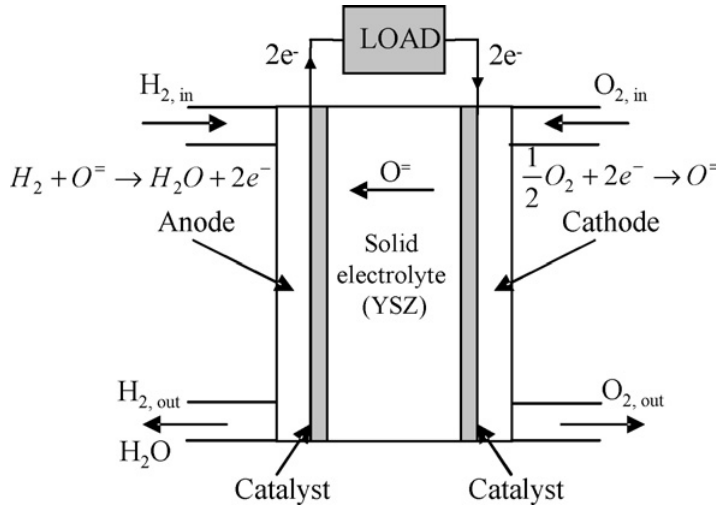

Fig. 1.1 – SOFC basic principle

$$\frac{1}{2}O_2 + 2e^- \rightarrow O^{2-} \qquad \textit{(cathode)} \qquad (1.1)$$

$$H_2 + O^{2-} \rightarrow H_2O + 2e^- \qquad \textit{(anode)} \qquad (1.2)$$

$$CH_4 + H_2O \rightarrow 3H_2 + CO \qquad \textit{(anode)} \qquad (1.3)$$

$$CO + H_2O \rightarrow CO_2 + H_2 \qquad \textit{(anode)} \qquad (1.4)$$

$$H_2 + \frac{1}{2}O_2 \rightarrow H_2O + 2e^- + heat \qquad \textit{(fuel cell)} \qquad (1.5)$$

To obtain the target electrical power, several cells are assembled together to form a stack, whose voltage and current outputs depend on the proper combination of parallel and series electrical connections among the cells. Moreover, to guarantee the proper operations of the stack some devices (i.e. balance of plant – BoP) are required to provide the right amount of

reacting gases (i.e. air and reformate/hydrogen) as well as to manage the outflow hot gases for heat recovery. Besides the pre-reformer, which provides the reformate gas to the anode, the standard equipments of the BoP are: a blower for cathodic air supply; a set of heat exchangers, for inlet gases heating and outlet gases heat recovery; a post burner, to convert the residual anodic gas chemical energy into heat; a set of valves, for the fluid and thermal managements guaranteeing both performance optimization and thermal stresses control of the stack materials. The complex interaction among BoP and stack requires well-designed control strategies to optimize system (Stack and BoP) performance as well as advanced diagnosis algorithms for fault management to avoid failures, which in turn may improve lifetime (Arsie et al., 2010 a; Sorrentino and Pianese, 2011; Marra et al., 2011).

1.2 Cell material

Specific materials must be selected for electrolyte, electrodes and interconnects. Basically, due to the high working temperatures (i.e. in the range 650-1000 °C), all components are made of ceramic-based materials. Nowadays, the most relevant material for SOFC electrolyte is Yttria Stabilized Zirconia (YSZ). Such compound is obtained by doping zirconia with yttria at very high temperatures (i.e. 2400 °C) (Ormerod, 2003). Through this process, a considerable number of oxygen ion vacancies are introduced in the original crystalline structure, thus significantly increasing the ionic conductivity at high temperatures (Bogicevic et al., 2001). Fig. 1.2 shows ionic conductivity as function of temperature for YSZ and other electrolyte materials. Larminie and Dicks (2003) indicated that a minimum value of 10^{-2} S cm^{-1} must be guaranteed to attain acceptable power densities. Therefore, YSZ-electrolyte SOFC (see the corresponding, gray-circled line in Fig. 1.2) has to be operated at temperature at least as high as 700÷750 °C (Weber and Tiffeè, 2004).
Anode in SOFCs must comply with conflicting requirements, such as high electronic conductivity, resistance to both reducing and oxidizing species, good thermal match with electrolyte and high porosity. These characteristics are achieved with nickel cermet anodes, obtained by adding nickel particles to YSZ. Thermal mismatch of components is a

major concern in SOFC, because the risk of mismatch increases with amount of nickel added. Therefore, a satisfactory compromise between the above mentioned features has to be found. Thermal mismatch is also one of the main motivations that push SOFC researchers to develop appropriate dynamic simulation tools (Selimovic et al., 2005). During transients, the intrinsic mismatch level may cause components crack if the temperature gradient rise across the cell is not adequately controlled. Another issue to be accounted for, when selecting anode material, is the low resistance of nickel, a noble metal, to carbon deposition. This is particularly a concern in case of internal reforming of methane. Researchers are currently working either on adding further dopants or introducing a separate catalyst for the activation of the methane reforming reaction (Ormerod, 2003). Regarding cathode materials, they are required to guarantee the same characteristics as anode ones, but in addition they must promote the formation of oxygen ions at the interface with the electrolyte. To this end, the majority of SOFC developers utilize a perovskite material, Strontium-doped Lanthanum Manganite (LSM). Similar considerations on thermal mismatch mentioned for anode must be taken in account for cathode as well (Ormerod, 2003). Finally, the primary requirement for interconnect is the high electronic conductivity. Considering the operating temperatures, ceramic materials such as lanthanum chromite are mainly used (Ormerod, 2003). For relatively low operating temperatures, such as in anode supported SOFCs, metallic interconnects also are suitable (Christiansen et al., 2005).

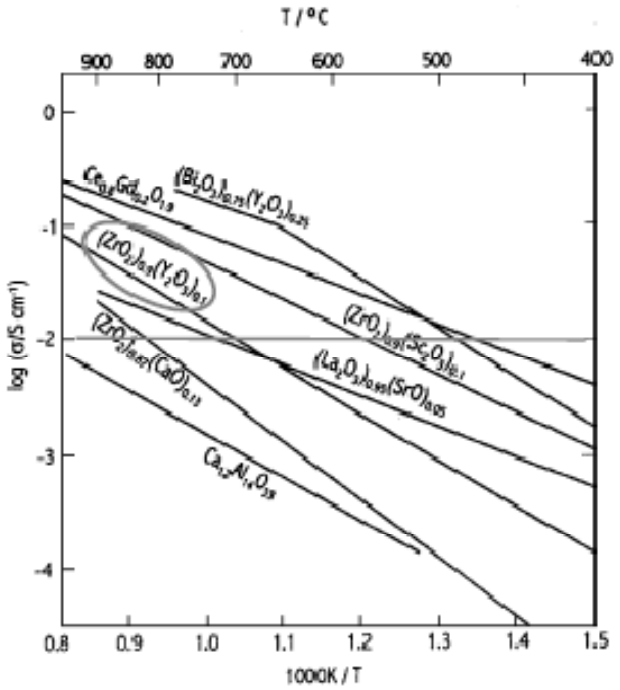

Fig. 1.2 - Conductivities of major SOFC electrolytes as function of average operating temperature (Ormerod, 2003).

1.3 Fuel Cell Typologies

Several fuel cell typologies are available, each one with distinguishing features and, thus, suitable for specific applications. Following a commonly used criterion (Fuel Cell Handbook, 2002), fuel cells are mainly categorized according to electrolyte type, as shown in Tab. 1.1. Among the fuel cells listed in the Tab. 1.1, it is worth mentioning that phosphoric acid fuel cells (PAFC) are the only typology that is already commercialized for high-power stationary applications (Okano, 2003). Nevertheless, the majority of actual researches focuses on PEMFC and SOFC, which are considered as the most promising fuel cells for both transportation and stationary applications (Sorrentino, 2006).

	PEMFC	DMFC	AFC
Electrolyte	Polymeric membrane	Polymeric membrane	Potassium hydroxide
Operating Temperature [°C]	60-100	30-100	65-220
Efficienncy [%]	35-50	20-40	45
Start-up	Fast (1 min)	Fast	Fast
Change carrier	H^+	H^+	OH^-
Catalyst	Platinum	Platinum	Platinum
Fuel Reforming	External (but pure H_2 is preferable)	No need of reforming, it runs with methenol	External
Appliclation fields	Automotive power and APU, portable power, small-scale stationary power	Portable power, Lap-top, phones	Space
	PAFC	**MCFC**	**SOFC**
Electrolyte	Liquid phoshoric acid	Liquid molten carbonate	Ceramic
Operating Temperature [°C]	150-220	600-700	600-1000
Efficienncy [%]	40	45-50	45-60
Start-up	Medium	Slow	Slow (20 min)
Change carrier	H^+	CO_3^-	O^-
Catalyst	Platinum	Nickel	Perovskite
Fuel Reforming	External	Internal or external	Internal or external
Appliclation fields	Large vehicle power, on-site cogeneration, stationary power	on-site cogeneration, stationary power	Automotive APU, heavy-dutyvehicle propulsion, marine and rail power, on-site cogeneration, stationary power

Tab. 1.1 – Main features of the mayor fuel cell typologies (sources: Moran and Shapiro, 2004; Fuel Cell Handbook, 2002; Rajashekara, 2000; Larminie and Dicks, 2003, Topsoe, 2002

CHAPTER 2 One-Dimensional SOFC Stack Modeling

The one-dimensional (1-D) modeling of SOFC stack allows achieving a satisfactory compromise between the conflicting needs of high model precision and affordable computational time. The knowledge of the spatial distributions of current, temperature and partial pressures in the flow direction allows for accurate prediction of cell performance. On the other hand, avoiding to solve the governing equations in the other dimensions results in significant reduction of computational time. The high physical content guaranteed by a 1-D approach provides considerable flexibility to account for different cell geometries, materials and fuel feeds. The above features are particularly useful to perform "virtual experiments" throughout the operating domain of an SOFC. Therefore, the recourse to a 1-D model is particularly promising for SOFC-related optimization problems, such as parameters identification for off-line control and diagnosis. The parameters identification can be useful for an adaptive control, or for a diagnostic application, considering for example the degradation of a SOFC stack.
In the next sections the entire 1-D model is described and the results relative to IEA validation (Braun, 2002) and a cross-validation with other similar models are presented. Finally, is reported a possible application for off-line diagnostic application of the 1-D model in case of degradation estimation in SOFC stack (Marra et al., 2010).

2.1 1-D model description

The one-dimensional (1-D) model developed and described in this work is an improvement of the cell model developed (Sorrentino, 2006). The model is written using the Matlab© programming language. The model maintains a similar structure of the previous one, particularly it consists of a set of sub-models, namely energy, material and electrochemical balance.

The model accounts for variations in the cell by discretizing the domain into computational elements along the cell length (Fig. 2.1). At each computational element, balances for mass, energy and electric potential are applied in a closed form. Main hypothesis assumed for the previous model are kept. More precisely, the cell is assumed to be isopotential (Braun, 2002) and fully-stirred conditions are considered at the element level. Assuming uniform distribution but no mixing of air and fuel feed gases, the two streams are treated separately as perfect gases. Pressure drop across the fuel and air channels is safely neglected (Burt et al., 2004). Moreover the cell is considered adiabatic.
The main contributions to the model improvement can be summarized as follows:

i) Introduction of the conductive heat exchange in the solid trilayer.
ii) Adoption of a different mathematical resolution of the systems equations.
iii) Extension of the model to counter flow configuration.

In the model developed the conductive heat exchange in the solid trilayer is considered. This allows to take into account the heat exchange due to effect of the temperature gradient in the streamwise direction. This is particular relevant in counter-flow configuration, and the model shows an improvement in the performance, as it will be shown in the cross-validation tests described in the paragraph 2.3.
In the previous model the computation starts at the inlet section of the fuel/air flows and marches forward in the streamwise direction (Braun, 2002; Haynes, 1999). This computation mode has been changed, developing a global method which accounts for the resolution of all the equations referring to all the computational elements simultaneously. The new computation mode has several advantages. First on all the model can be adopted for different cell configuration, particularly for counter flow configuration. This was not possible with the previous method because it requires, as initial step, the knowledge of the gases and temperature conditions in the first computational unit. This is not possible in the counter-flow configuration because the fuel and air inlet sections are opposite (Fig. 2.1). The global computation mode is an implicit method, thus resulting more stable with numerical issues. The disadvantage is only the cache memory requirement, which grows with N^2, while for iterative

marching technique the requirement is proportional to *N*, with *N* number of computational cells. This problem is not relevant because the model shows accurate results just with only 20 computational units, as shown in the result description. Finally this method reduces the computational time. After the introduction of the new numerical solution technique it is possible to simulate the cell in counter-flow configuration (achievable by changing some equations in the sub-models, as described in the following paragraphs). Therefore the generalization towards cell configuration has been generated in the fame of 1-D flows. Moreover the new computational configuration can be easily extended to 2-D configurations such as cross-flow.
The 1-D model developed is more flexible and generalizable and it can be adopted for different SOFC technologies.

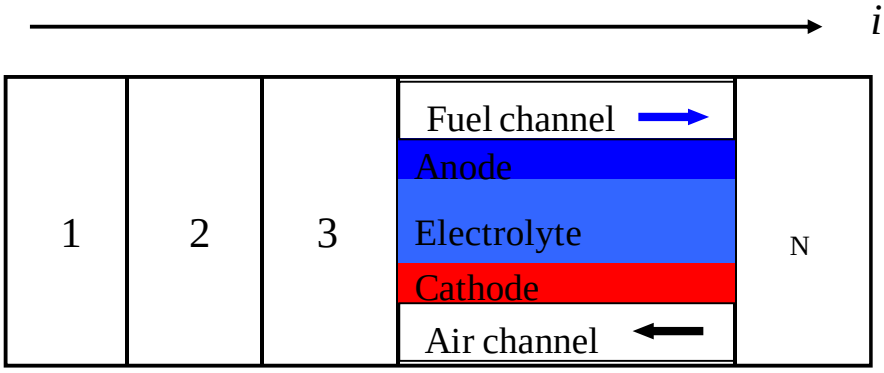

Fig. 2.1 – Cell computational discretization for counter flow configuration.

2.1.1. Eletrochemical submodel

The electrochemical sub-model evaluates SOFC voltage and power along the cell. For each element *i* the current density is calculated by Faraday's law:

$$J^i = \frac{\dot{r}_{ox}^i \cdot F \cdot n_e}{A^i} \tag{2.1}$$

where n_e is the number of electrons transferred per molecule of H_2 (i.e. $n_e = 2$), $\dot{r}^i_{ox}$ is the reaction rate (mol s^{-1}) of the electro-oxidation reaction and A^i (cm^2) is the area of the single computational element (i.e. $A^i = A/N$). Multiplying the current density of each element by A^i, the total current is found summing up the contributions from the N computational elements:

$$I_{SOFC} = \sum_{i=1}^{N} \left(J^i \cdot A^i \right) \tag{2.2}$$

With reference to Eqq. (1.1), (1.2), (1.5), the ideal potential difference between anode and cathode is evaluated using the Nernst equation:

$$E^i_{Nernst} = -\frac{\Delta G^i_{ox}(T^i_s)}{n_e F} - \frac{R_u T^i_s}{n_e F} \ln\left(\frac{p^i_{H_2O}}{p^i_{H_2}\sqrt{p^i_{O_2}}} \right) \tag{2.3}$$

There are three major forms of polarization losses: activation, Ohmic and concentration. A constant offset also contributes to the total polarization, which is the result of minor losses such as contact resistance, internal current and leaks. Following Chick et al., (2003), the offset was assumed equal to 0.07 V. The sum of the different polarizations results in the voltage drop from ideal Nernst potential to effective operating value. Since interconnect and electrodes are isopotential, cell voltage is constant over the whole cell and can be estimated as

$$V_{SOFC} = E^i_{Nernst} - V^i_{Act} - V^i_{Ohm} - V^i_{Conc} - V^i_{Offset} \tag{2.4}$$

The total power drawn from the SOFC is calculated as:

$$\dot{E}_{el} = V_{SOFC} \cdot I_{SOFC} \tag{2.5}$$

where I_{SOFC} is given by Eq. (2.2). The following three sub-sections deal with the modeling of activation, Ohmic and concentration polarization

losses.

Activation polarization

Activation polarization represents the energy barrier to be overcome to activate the electrochemical reactions occurring at the electrodes surface (Fuel Cell Handbook, 2002). This amount of energy inevitably causes a significant voltage loss, which is usually modeled through the non-linear relationship known as Butler–Volmer equation (Keegan, 2002):

$$V_{Act}^{i} = \frac{R \cdot T_s^i}{\alpha(T_s^i) \cdot F} \cdot \sinh^{-1}\left(\frac{J^i}{2J_0(T_s^i)}\right) \tag{2.6}$$

where α is the charge transfer coefficient and J_0 is the exchange current density.

Ohmic polarization

Ohmic polarization mainly depends on the electronic conductivity of electrodes and the ionic conductivity of the electrolyte. Such losses are estimated summing up the contribution from each SOFC part (i.e. anode, cathode and electrolyte), as follows:

$$\begin{aligned} V_{Ohm,k}^{i} &= \frac{l_k}{\sigma_k(T_s^i)} \cdot J^i \\ V_{Ohm}^{i} &= \sum_k V_{Ohm,k}^{i} \qquad k = [an, ca, el] \end{aligned} \tag{2.7}$$

Conductivities are estimated by means of correlations, proposed in literature (Chick et al., 2003) for second-generation ceramic SOFC, in which the materials of anode, cathode and electrolyte are, nickel-cermets, strontium-doped lanthanum manganite and yttria-stabilized zirconia, respectively:

$$\sigma_{an} = 1000 \tag{2.8}$$

$$\sigma_{ca}(T_s) = C_1(T_s^i)^2 - C_2 T_s^i + C_3 \tag{2.9}$$

$$\sigma_{el}(T_s) = C_4(T_s^i - 273)^2 + C_5(T_s^i - 273) + C_6 \tag{2.10}$$

Concentration polarization

As fuel is depleted, hydrogen and oxygen partial pressures decrease at anode and cathode, respectively. The depletion rate depends on average current density drawn from the cell. Therefore, as the current density increases, the partial pressures decrease and eventually an insufficient amount of reactants are transported to the electrodes. This results in significant losses until the voltage is reduced to 0 (Singhal and Kendall, 2003; Larminie and Dicks, 2003). The values at which such phenomenon occurs are known as anode and cathode limiting currents. This voltage loss, which is dominant at high current densities, is called concentration polarization and can be estimated as follows:

$$V_{Conc}^i = -\frac{R \cdot T_s^i}{2 \cdot F} \cdot \left[\frac{1}{2} \ln\left(1 - \frac{J^i}{J_{cs}}\right) + \ln\left(1 - \frac{J^i}{J_{as}}\right) - \ln\left(1 + \frac{p_{H_2}^i \cdot J^i}{p_{H_2O}^i \cdot J_{cs}}\right) \right] \tag{2.11}$$

The anode and cathode limiting currents (i.e. J_{as} and J_{cs} respectively) are computed as function of species diffusion coefficients, following the approach proposed in (Braun, 2002).

2.1.2. Simplified polarization losses sub-model

In the development of the 1-D model it was exploited a simplified polarization losses sub-model. This decision was taken for the purpose of reduce the computational burden.

The activation and concentration losses were approximated as being equal to the Ohmic loss of the electrolyte, thus the Eq. (2.4) is changed as follows:

$$V_{SOFC} = E_{Nernst}^i - V_{Ohm}^i - 2 \cdot V_{Ohm,el}^i \tag{2.12}$$

where V_{ohm} is computed through Eq. (2.7). The conductivities of anode, cathode and electrolyte are estimated using the following relationships suggested by IEA (Braun, 2002):

$$\sigma_{an,IEA} = \frac{95 \cdot 10^6}{T_s^i} \cdot \exp\left(\frac{-1150}{T_s^i}\right) \tag{2.13}$$

$$\sigma_{ca,IEA} = \frac{42 \cdot 10^6}{T_s^i} \cdot \exp\left(\frac{-1200}{T_s^i}\right) \tag{2.14}$$

$$\sigma_{el,IEA} = \frac{3.34 \cdot 10^4}{T_s^i} \cdot \exp\left(\frac{-10300}{T_s^i}\right) \tag{2.15}$$

2.1.3. Conservation equations in co-flow configuration

Conservation of mass, energy and electric potential are applied to each computational elements. Momentum equation was not considered since it is assumed that pressure drop across the cell can be neglected. The structure of models was conceived in such a way to account for internal reforming of a partially pre-reformed methane feed. The fuel flowing in the cell, which typically consists of a mixture of H_2, CH_4, CO and H_2O, undergoes steam reforming of CH_4 (Eq. (1.3)), water-gas shift reaction (Eq. (1.4)), and electrochemical oxidation of H_2 (Eq. (1.5)). The water gas shift reaction Eq. (1.4) is assumed to be in equilibrium, the corresponding equilibrium constant being equal to:

$$K_{shift}(T_s^i) = \exp\left(\frac{-\Delta G_{shift}(T_s^i)}{R \cdot T_s^i}\right) \tag{2.16}$$

The equilibrium constant can also be expressed as function of the species molar fractions, as follows (Massardo and Lubelli, 2000):

$$K_{shift} = \frac{x_{H_2} \cdot x_{CO_2}}{x_{CO} \cdot x_{H_2O}} = \frac{\left(\dfrac{\dot{n}_{H_2}^{i-1} + 3\dot{r}_{ref}^i + \dot{r}_{shift}^i - \dot{r}_{ox}^i}{\dot{n}_{tot}^{i-1} + 2\dot{r}_{ref}^i}\right) \cdot \left(\dfrac{\dot{n}_{CO_2}^{i-1} + \dot{r}_{shift}^i}{\dot{n}_{tot}^{i-1} + 2\dot{r}_{ref}^i}\right)}{\left(\dfrac{\dot{n}_{CO}^{i-1} + \dot{r}_{ref}^i - \dot{r}_{shift}^i}{\dot{n}_{tot}^{i-1} + 2\dot{r}_{ref}^i}\right) \cdot \left(\dfrac{\dot{n}_{H_2O}^{i-1} - \dot{r}_{ref}^i - \dot{r}_{shift}^i + \dot{r}_{ox}^i}{\dot{n}_{tot}^{i-1} + 2\dot{r}_{ref}^i}\right)} \tag{2.17}$$

where $\dot{r}_{ref}^i$, $\dot{r}_{shift}^i$ and $\dot{r}_{ox}^i$ are, the reaction rates (mol/s) of the methane

reforming Eq. (1.3) , water-gas shift Eq. (1.4) and electro-oxidation Eq. (1.5) reactions, respectively. $\dot{r}^i_{shift}$ is found solving the system of Eqq. (2.16), (2.17), while $\dot{r}^i_{ox}$ and $\dot{r}^i_{ref}$ are estimated via Faraday's law and the temperature/pressure dependent correlation proposed by Achenbach and Riensche, (1994):

$$\dot{r}^i_{ox} = \frac{J^i \cdot A^i}{F \cdot n_e} \tag{2.18}$$

$$\dot{r}^i_{ref} = 4274 \cdot p^i_{CH_4} \cdot A^i e^{-(82000/R/T^i_f)} \tag{2.19}$$

Electric potential balance

Since the interconnect and the electrodes are assumed to be isopotential, the voltage is constant over the whole cell, thus yielding the following balance to be solved for each computational element:

$$E^i_{Nernst} - V^i_{Act} - V^i_{Ohm} - V^i_{Conc} - V^i_{Offset} - V_{SOFC} = 0 \tag{2.20}$$

Material balance

Applying conservation of mass to a generic control volume Ω (see Fig. 2.2), the steady-state material balance for each specie *j* can be expressed as:

$$\int_\Omega \vec{\nabla} \cdot \vec{N}_j dV = 0 \qquad j = [H_2, CH_4, H_2O, CO, CO_2, N_2, O_2] \tag{2.21}$$

Anode and cathode are discretized in the flow direction as shown on Fig. 2.2, where inlet, outlet and source (or sink) molar flows are represented for the *i*-th element and the j_{an}-th and j_{ca}-th specie. Applying Eq. (2.21) to the discretized cell for all the species, the following material balances result:

$$anode: \quad \begin{cases} \dot{n}^{i}_{H_2} = \dot{n}^{i-1}_{H_2} + 3 \cdot \dot{r}^{i}_{ref} + \dot{r}^{i}_{shift} - \dot{r}^{i}_{ox} \\ \dot{n}^{i}_{CH_4} = \dot{n}^{i-1}_{CH_4} - \dot{r}^{i}_{ref} \\ \dot{n}^{i}_{H_2O} = \dot{n}^{i-1}_{H_2O} - \dot{r}^{i}_{ref} - \dot{r}^{i}_{shift} + \dot{r}^{i}_{ox} \\ \dot{n}^{i}_{CO} = \dot{n}^{i-1}_{CO} + \dot{r}^{i}_{ref} - \dot{r}^{i}_{shift} \\ \dot{n}^{i}_{CO_2} = \dot{n}^{i-1}_{CO_2} + \dot{r}^{i}_{shift} \end{cases} \tag{2.22}$$

$$cathode: \quad \begin{cases} \dot{n}^{i}_{N_2} = \dot{n}^{i-1}_{N_2} \\ \dot{n}^{i}_{O_2} = \dot{n}^{i-1}_{O_2} - 0.5 \cdot \dot{r}^{i}_{ox} \end{cases} \tag{2.23}$$

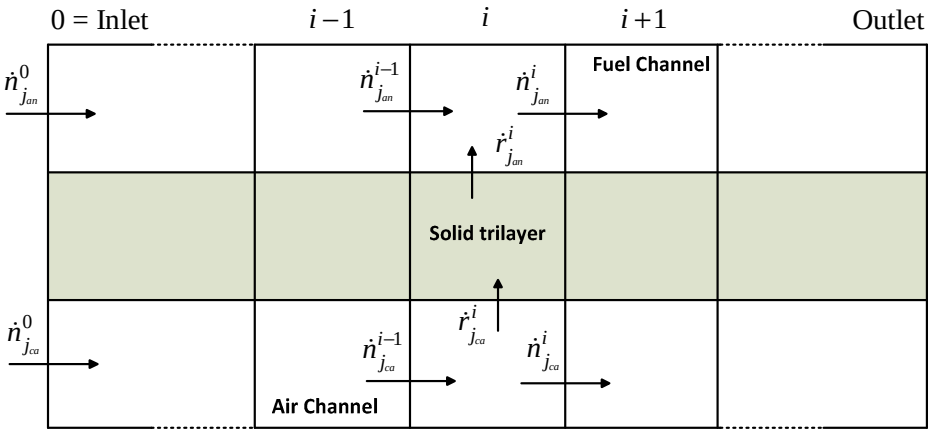

Fig. 2.2 – Discretized mass balance at the *i*-th element for co-flow configuration.

Boundary conditions of the system (2.22), (2.23) are the inlet flows, estimated according to the operating fuel utilization and excess air factors:

$$U_f = \begin{cases} \dfrac{\dot{n}_{H_2,react}}{\dot{n}^{0}_{H_2}} = \dfrac{\bar{J} \cdot A}{F \cdot n_e} \cdot \dfrac{1}{\dot{n}^{0}_{H_2}} & \textit{pure } H_2 \textit{ feed} \\ \dfrac{\dot{n}_{H_2,react}}{\dot{n}^{0}_{CH_4}} = \dfrac{\bar{J} \cdot A}{F \cdot n_e} \cdot \dfrac{1}{4\dot{n}^{pre}_{CH_4}} & \textit{refomate feed} \end{cases} \tag{2.24}$$

$$\lambda = \frac{\dot{n}^0_{O_2}}{\dot{n}^0_{O_2,sto}} = \frac{\dot{n}^0_{O_2}}{\frac{1}{2}\dot{n}_{H_2,react}} = \frac{\dot{n}^0_{air}}{4.76 \cdot \frac{1}{2}\dot{n}_{H_2,react}} \tag{2.25}$$

It is worth noting that the denominator of Eq. (2.24) for reformate feed equals 4 times the methane flow at pre-reformer inlet. This holds because for each CH_4 molecule, 4 H_2 molecules can be obtained, as indicated by reactions (1.3)-(1.5). The use of a pre-reforming stage, to partially pre-reform methane, is required to avoid sudden temperature decrease at cell inlet caused by the endothermic reaction (1.3).

Energy balance

The energy balance is applied by dividing the computational element into three separate control volumes, namely solid trilayer and fuel and air channels (see Fig. 2.3). Further simplifying hypotheses are: cell boundaries are adiabatic and radiative heat transfer between solid trilayer and metallic interconnects is assumed negligible. Although previous works (Braun, 2002; Burt et al., 2004) report that the radiative heat transfer mechanism could enhance the model accuracy. The heat conduction in the solid trilayer in the flow direction is considered, while in the previous model (Sorrentino et al., 2008) was neglected. Hence, the dominant energy balance effects described in the model are the convective heat transfer between solid trilayer and fuel and air streams, the heat conduction in the solid trilayer in flow direction and the energy transfer due to the reactants and products flows.

The steady-state energy balance for an open system reads as:

$$\frac{dE}{dt} = \dot{E}_{in} - \dot{E}_{out} + \dot{Q} - \dot{L} = 0 \tag{2.26}$$

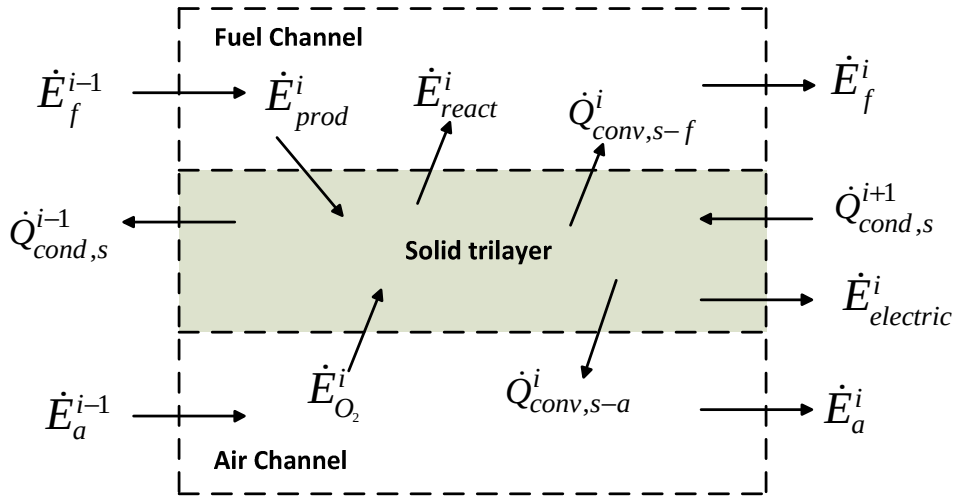

Fig. 2.3 – Energy balance at the *i*-th element for co-flow configuration.

Applying Eq. (2.26) to the three control volumes shown on Fig. 2.3, the following energy balances hold for solid trilayer, fuel channel and air channel, respectively:

$$\dot{E}_{react}^i - \dot{E}_{prod}^i + \dot{E}_{O_2}^i - \dot{Q}_{conve,s-a}^i + Q_{cond}^{i+1} - Q_{cond}^{i-1} - \dot{E}_{electric}^i = 0 \qquad \text{(solid)} \qquad (2.27)$$

$$\dot{E}_f^{i-1} - \dot{E}_f^i - \dot{E}_{react}^i + \dot{E}_{prod}^i + \dot{Q}_{conve,s-f}^i = 0 \qquad \text{(fuel)} \qquad (2.28)$$

$$\dot{E}_a^{i-1} - \dot{E}_a^i - \dot{E}_{O_2}^i + \dot{Q}_{conve,s-a}^i = 0 \qquad \text{(air)} \qquad (2.29)$$

The energy rates, associated with inlet and outlet flows and the electrooxidation, reforming and water-gas shift reactions, are calculated as follows:

$$\begin{aligned}\dot{E}_{react}^i = {} & h_{H_2}(T_f^i) \cdot \dot{r}_{ox}^i + \left[h_{CH_4}(T_f^i) + h_{H_2O}(T_f^i) \right] \cdot \dot{r}_{ch_4}^i + \\ & \left[h_{CO}(T_f^i) + h_{H_2O}(T_f^i) \right] \cdot \dot{r}_{shift}^i\end{aligned} \qquad (2.30)$$

$$\dot{E}^{i}_{prod} = h_{H_2O}(T^{i}_{s}) \cdot \dot{r}^{i}_{ox} + \left[3 \cdot h_{H_2}(T^{i}_{s}) + h_{CO}(T^{i}_{s})\right] \cdot \dot{r}^{i}_{ch_4} + \left[h_{H_2}(T^{i}_{s}) + h_{CO_2}(T^{i}_{s})\right] \cdot \dot{r}^{i}_{shift} \tag{2.31}$$

$$\dot{E}^{i}_{O_2} = \frac{\dot{r}^{i}_{ox}}{2} h_{H_2O}(T^{i}_{s}) \tag{2.32}$$

$$\dot{E}^{i}_{f} = \dot{n}^{i}_{H_2} \cdot h_{H_2}(T^{i}_{f}) + \dot{n}^{i}_{CH_4} \cdot h_{CH_4}(T^{i}_{f}) + \dot{n}^{i}_{H_2O} \cdot h_{H_2O}(T^{i}_{f}) + \dot{n}^{i}_{CO_2} \cdot h_{CO_2}(T^{i}_{f}) + \dot{n}^{i}_{CO} \cdot h_{CO}(T^{i}_{f}) \tag{2.33}$$

$$\dot{E}^{i-1}_{f} = \dot{n}^{i-1}_{H_2} \cdot h_{H_2}(T^{i-1}_{f}) + \dot{n}^{i-1}_{CH_4} \cdot h_{CH_4}(T^{i-1}_{f}) + \dot{n}^{i-1}_{H_2O} \cdot h_{H_2O}(T^{i-1}_{f}) + \dot{n}^{i-1}_{CO_2} \cdot h_{CO_2}(T^{i-1}_{f}) + \dot{n}^{i-1}_{CO} \cdot h_{CO}(T^{i-1}_{f}) \tag{2.34}$$

$$\dot{E}^{i}_{a} = \dot{n}^{i}_{O_2} \cdot h_{O_2}(T^{i}_{a}) + \dot{n}^{i}_{N_2} \cdot h_{N_2}(T^{i}_{a}) \tag{2.35}$$

$$\dot{E}^{i-1}_{a} = \dot{n}^{i-1}_{O_2} \cdot h_{O_2}(T^{i-1}_{a}) + \dot{n}^{i-1}_{N_2} \cdot h_{N_2}(T^{i-1}_{a}) \tag{2.36}$$

$$\dot{E}^{i}_{electric} = V_{SOFC} \cdot J^{i} \cdot A^{i} \tag{2.37}$$

Convective heat transfer between solid cell and fuel/air channel is computed as:

$$\dot{Q}^{i}_{conve,s-f} = \bar{h}_{f} \cdot A_{s} \cdot (T^{i}_{s} - T^{i}_{f}) \tag{2.38}$$

$$\dot{Q}^{i}_{conve,s-a} = \bar{h}_{a} \cdot A_{s} \cdot (T^{i}_{s} - T^{i}_{a}) \tag{2.39}$$

$$\bar{h}_{f} = \frac{N_u \cdot k_f}{D_h} \tag{2.40}$$

$$\bar{h}_a = \frac{N_u \cdot k_a}{D_h} \tag{2.41}$$

The hydraulic diameter (Iwata et al., 2000) and Nusselt number (Braun, 2002) are estimated as, respectively:

$$D_h = \frac{4A_{ch}}{2(l_{ch} + w_{ch})} \tag{2.42}$$

$$\begin{aligned} N_u &= 7.541(1 - 2.61 \cdot \beta + 4.97 \cdot \beta^2 - 5.119 \cdot \beta^3 + \\ &+ 2.702 \cdot \beta^4 + 0.548 \cdot \beta^5) \end{aligned} \tag{2.43}$$

where β is the ratio between channel height and channel width. Following (Braun, 2002), the thermal conductivity of the gas mixture, k_{gas}, is calculated as function of the thermal conductivity of fuel species:

$$k_f = \sum_{j=1}^{n} \frac{x_j k_j}{\sum_{m=1}^{n} k_m z_{jm}} \tag{2.44}$$

$$z_{jm} = \frac{\left[1 + (k_j / k_m)^{1/2} \cdot (M_m / M_j)^{1/4}\right]^2}{\left[8 \cdot (1 + M_j / M_m)\right]^{1/2}} \tag{2.45}$$

where k_j (k_m) and M_j (M_m) are the molar mass and thermal conductivity of the j-th (m-th) species, respectively.
Conductive heat in the solid trilayer in the flow direction is computed as:

$$\dot{Q}_{cond,s}^{i+1} = \frac{k_s}{\Delta x} A_{cross} (T_s^{i+1} - T_s^i) \tag{2.46}$$

$$\dot{Q}_{cond,s}^{i-1} = \frac{k_s}{\Delta x} A_{cross} (T_s^i - T_s^{i-1}) \tag{2.47}$$

Where $\dot{Q}_{cond,s}^{i+1}$ and $\dot{Q}_{cond,s}^{i-1}$ refers to the conductive heat exchanged between the *i+1*-th and the *i*-th computational element of the solid trilayer, and between *i*-th element and the *i-1*-th computational element of the solid trilayer.

A_{cross} represents the cross-sectional area and k_s is the solid trilayer conductivity. k_s is assumed to be constant with cell temperature variations and $k_s = 1.67 \ \frac{W}{mK}$.

2.1.4. Conservation equations in counter-flow configuration

Mass balance

The mass balance equations for the counter-flow configuration the mass balance changes as follows (see Eq. (2.23)):

$$cathode: \quad \begin{cases} \dot{n}_{N_2}^{i} = \dot{n}_{N_2}^{i-1} \\ \dot{n}_{O_2}^{i} = \dot{n}_{O_2}^{i-1} + 0.5 \cdot \dot{r}_{ox}^{i} \end{cases} \tag{2.48}$$

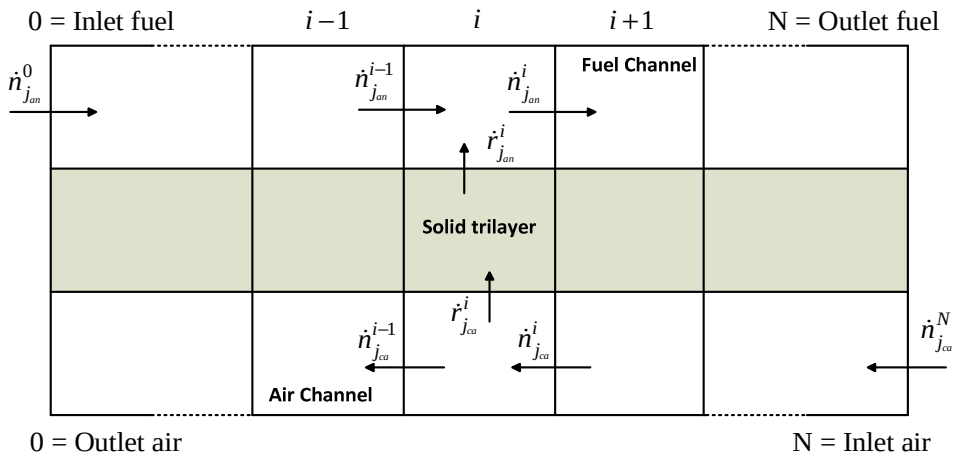

Fig. 2.4 - Discretized mass balance at the *i*-th element for counter-flow configuration.

Energy balance

With reference to the energy balance equations for the co-flow configurations (Eqq. (2.27)-(2.29)), according to the scheme of Fig. 2.5, the energy balance equations in case of counter-flow configurations change as follows:

$$\dot{E}^{i}_{react} - \dot{E}^{i}_{prod} + \dot{E}^{i}_{O_2} - \dot{Q}^{i}_{conve,s-a} + Q^{i+1}_{cond} - Q^{i-1}_{cond} - \dot{E}^{i}_{electric} = 0 \qquad \text{(solid)} \qquad (2.49)$$

$$\dot{E}^{i-1}_{f} - \dot{E}^{i}_{f} - \dot{E}^{i}_{react} + \dot{E}^{i}_{prod} + \dot{Q}^{i}_{conve,s-f} = 0 \qquad \text{(fuel)} \qquad (2.50)$$

$$\dot{E}^{i}_{a} - \dot{E}^{i-1}_{a} - \dot{E}^{i}_{O_2} + \dot{Q}^{i}_{conve,s-a} = 0 \qquad \text{(air)} \qquad (2.51)$$

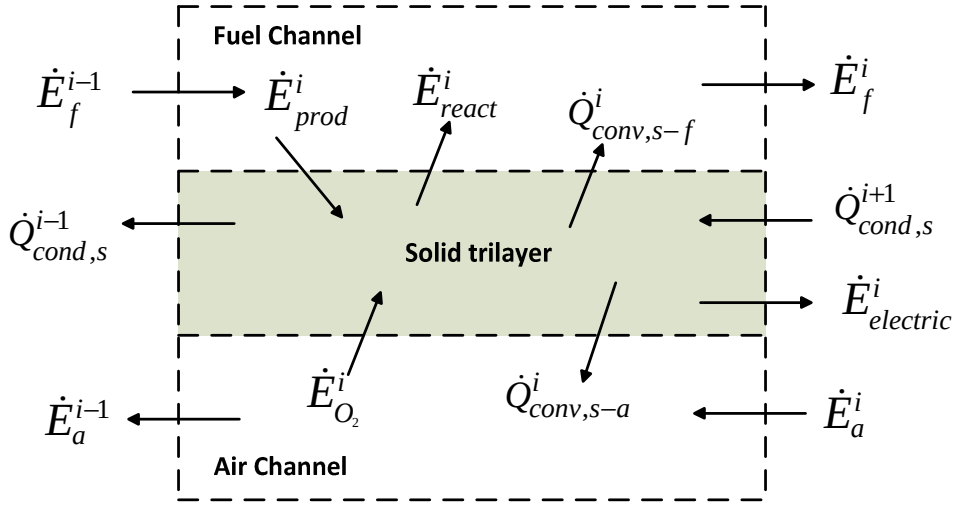

Fig. 2.5 - Energy balance at the *i*-th element for counter-flow configuration.

2.2 IEA model validation

The model developed was validated with the IEA Benchmark (Braun, 2002), considering both the co-flow and the counter flow configuration. The black-box electrochemical sub-model was adopted (Eqq. (2.12)-(2.15)) in the simulations. The model was tested in two operating conditions: 1) fueled with methane, 2) fueled with pure hydrogen (Tab. 2.1), with different number of nodes. The benchmark results are reported in Tab. 2.2 and in Tab. 2.3. The model outputs were included into IEA limits, thus resulting validated. In Fig. 2.6 the stack temperature was compared between co-flow and counter flow configuration, for the case 1. It is important noting that in counter flow-configuration the mean stack temperature is greater than in co-flow configuration (55 K), thus resulting in a greater stack voltage (0.697 V in counter-flow and 0.643 V in co-flow configuration). This effect is due the configuration of the gases flows, in the case of counter flow configuration, the maximum of stack temperature is near the air inlet section (see Fig. 2.6), thus also the current density is maximum in the same zone (Fig. 2.7). The effect of the maximum temperature near the inlet air section led to a faster reforming

reaction of the methane, as is it clear in Fig. 2.8.

Operating conditions case 1	
Fuel	Methane
Cell current density	0.3 [A/cm^2]
Gas inlet temperature	900 [°C]
Air inlet temperature	900 [°C]
Fuel Utilization	85%
Excess air	7
Pressure	1 [bar]
Operating conditions case 2	
Fuel	Hydrogen
Cell current density	0.3 [A/cm^2]
Gas inlet temperature	900 [°C]
Air inlet temperature	900 [°C]
Fuel Utilization	85%
Excess air	7
Pressure	1 [bar]

Tab. 2.1 – Operating conditions for IEA validation.

Parameters	Counter-flow configuration				Co-flow configuration			
	Benchmark (IEA data)	SOFC Model			Benchmark (IEA data)	SOFC Model		
Number of nodes		10	20	30		10	20	30
Voltage [V]	0.680 - 0.692	0.692	0.696	0.697	0.633 - 0.649	0.643	0.643	0.643
Current density [A/m^2]								
Max	5330 - 6554	5441	6351	6617	3040 - 3665	3502	3509	3519
Min	994 - 1332	1253	1193	1174	1748 - 2508	2489	2432	2409
Temperature [°C]								
Max	1062 - 1089	1087	1097	1107	1021 - 1034	1035	1035	1035
Min	906 - 915	911	905	904	847 - 862	861	855	852
Outlet gas temperature [°C]								
air	1018 - 1028	1034	1034	1034	1016 - 1026	1035	1035	1035
fuel	906 - 915	911	905	904	1021 - 1026	1035	1035	1035

Tab. 2.2 – One-dimensional model validation with IEA benchmark in counter and co-flow configurations (case 1).

Parameters	Counter-flow configuration				Co-flow configuration			
	Benchmark (IEA data)	SOFC Model			Benchmark (IEA data)	SOFC Model		
Number of nodes		10	20	30		10	20	30
Voltage [V]	0.709 - 0.730	0.714	0.716	0.717	0.702 - 0.722	0.703	0.706	0.707
Current density [A/m^2]								
Max	7107 - 8970	7151	8068	8496	3725 - 3957	3787	3733	3711
Min	1080 - 1235	1160	1122	1110	1020 - 1366	1168	1069	1036
Temperature [°C]								
Max	1062 - 1084	1100	1099	1099	1048 - 1098	1085	1084	1084
Min	904 - 913	909	904	903	909 - 930	922	911	908
Outlet gas temperature [°C]								
air	1064 - 1082	1099	1099	1099	1048 - 1067	1085	1084	1084
fuel	906 - 914	909	904	903	1048 - 1068	1085	1084	1084

Tab. 2.3 - One-dimensional model validation with IEA benchmark in counter and co-flow configurations (case 2).

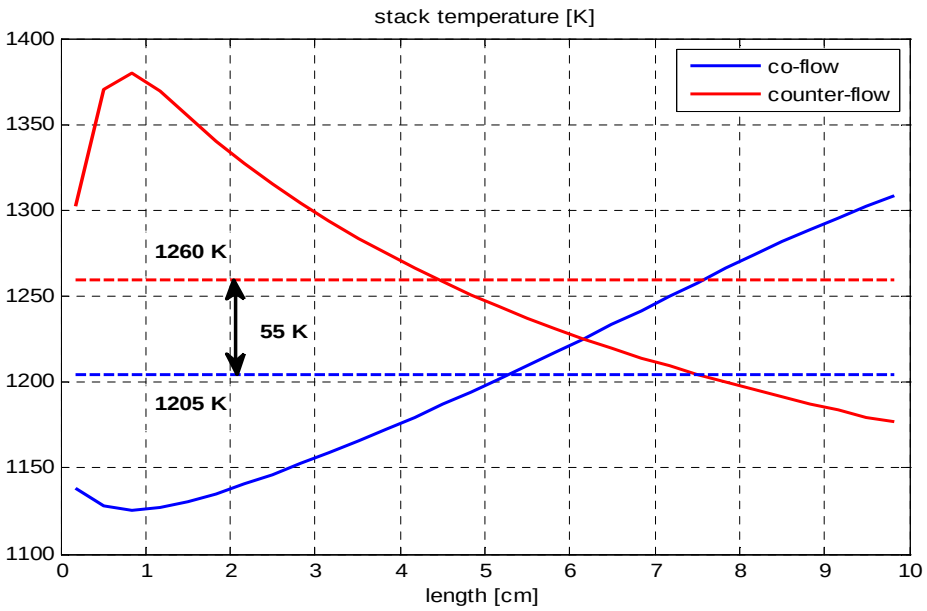

Fig. 2.6 – Comparison between stack temperature profiles in co-flow and counter flow configurations (case 1 of IEA validation)

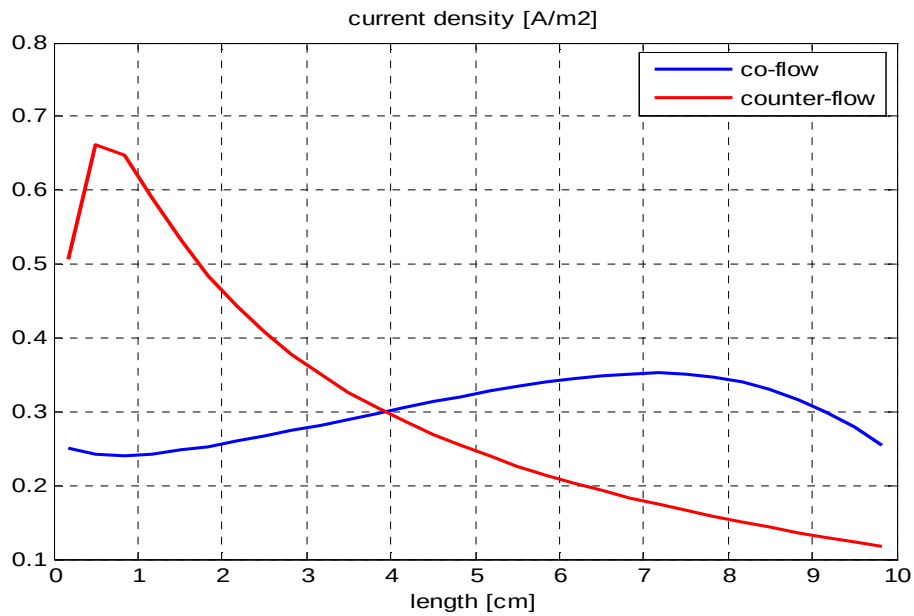

Fig. 2.7 - Comparison between current density profiles in co-flow and counter flow configurations (case 1 of IEA validation)

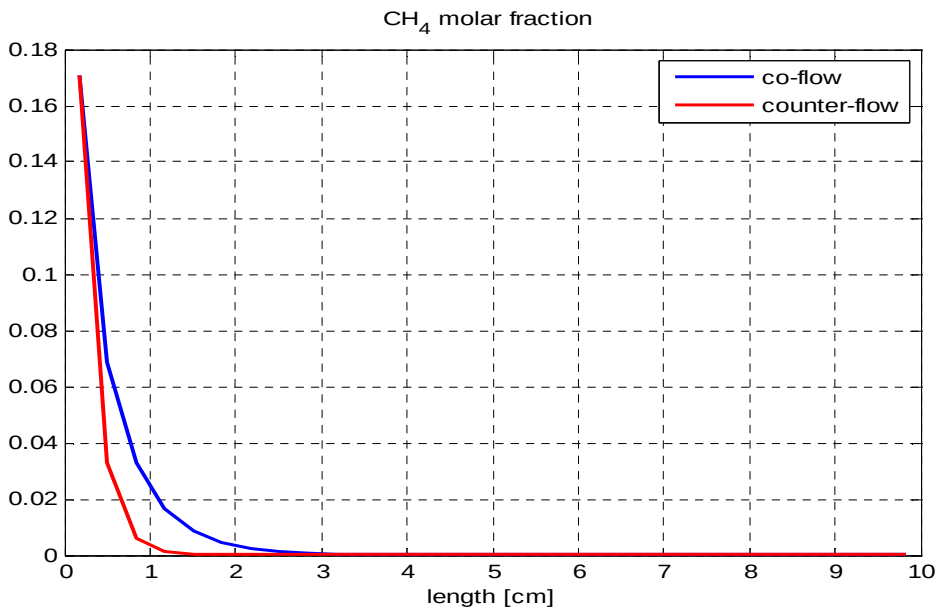

Fig. 2.8 - Comparison between CH_4 molar faction profiles in co-flow and counter flow configurations (case 1 of IEA validation)

2.3 Cross-validation

The 1-D model developed for planar counter-flow configuration and with heat conduction was compared with other similar models developed by other research centers (this comparison was performed in the frame work of the EU project GENIUS). Particularly the model was compared with the model developed by the University of Genoa (UNIGE) and by the VTT center in Finland. One model (UNIGE) is dynamic, whereas the other two are steady-state models. With this background, only the steady-state results were compared. The simulation experiments were defined so that would correspond to normal SOFC operating conditions (in a laboratory). The effects of three inputs were studied: average current density ($\bar{j}$) was set at 0.3 A/cm^2 and 0.35 A/cm^2; the fuel utilization rate (U_f) was set at 50% and 60%; the inlet gas temperature ($T_{an,in}$) was set at 700 °C and 750 °C. Six combinations of the parameters were examined, resulting in six simulation experiments (see Tab. 2.4). As the model

results were significantly dependent on some assumptions made about the cell solid phase, the simulations experiments were made in two different cases: i) the solid phase resembled a ceramic material and ii) the solid phase was closer to a metallic material.

Experiments number	Current density [A/cm^2]	Fuel Utilization [%]	Inlet Gas Temperature [°C]
1	0.3	50	700
2	0.35	50	700
3	0.3	60	700
4	0.3	50	750
5	0.35	60	700
6	0.35	60	750

Tab. 2.4 – Simulation experiments conditions

2.3.1. Results

In Fig. 2.9 and Fig. 2.10 are plotted the comparison between the three model of the average cell voltage and the cell maximum temperature in two different configurations. In the configuration number 1 the cell solid phase was considered to be composed in metallic material, while in the configuration number 2 it was supposed to be composed in ceramic material. The model results correspond to each other very well. The two static models of UNISA and VTT are close to identical, with only minor off-sets in the results. However, some results given by the dynamic model of UNIGE and those obtained with the two static models were notably different when the operating conditions were such that more severe gradients in temperature and current density arise. These differences are clearly evident in the current density and temperature profiles showed in Fig. 2.11 and Fig. 2.12.

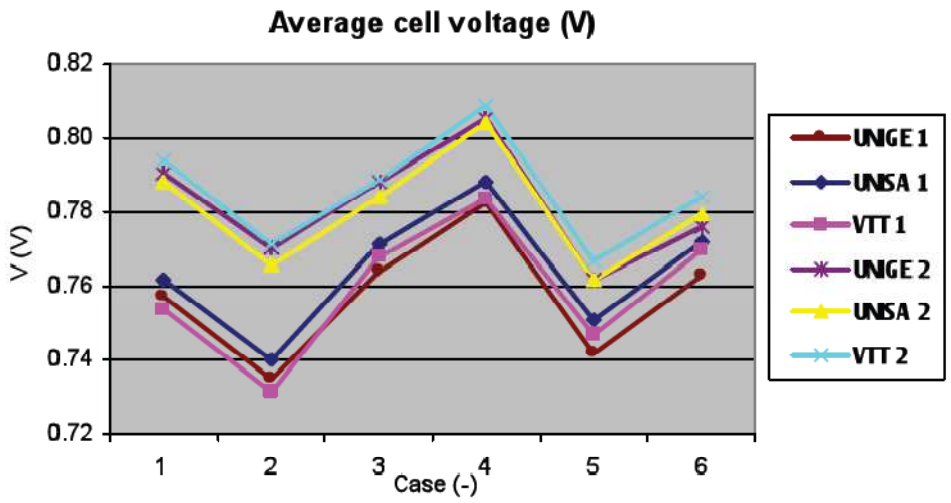

Fig. 2.9 – The average cell voltage estimated by the compared models. The x-axis refers to the simulation experiments of Tab. 2.4 and the model number given in the legend refers to either a metallic solid configuration (1) or a ceramic solid configuration (2).

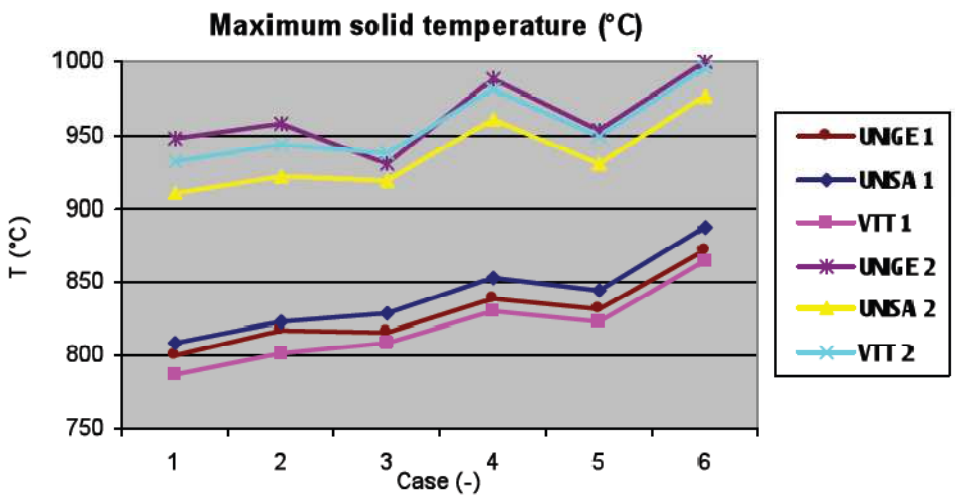

Fig. 2.10 - The maximum cell temperature estimated by the compared models. The x-axis refers to the simulation experiments of Tab. 2.4 and the model number given in the legend refers to either a metallic solid configuration (1) or a ceramic solid configuration (2).

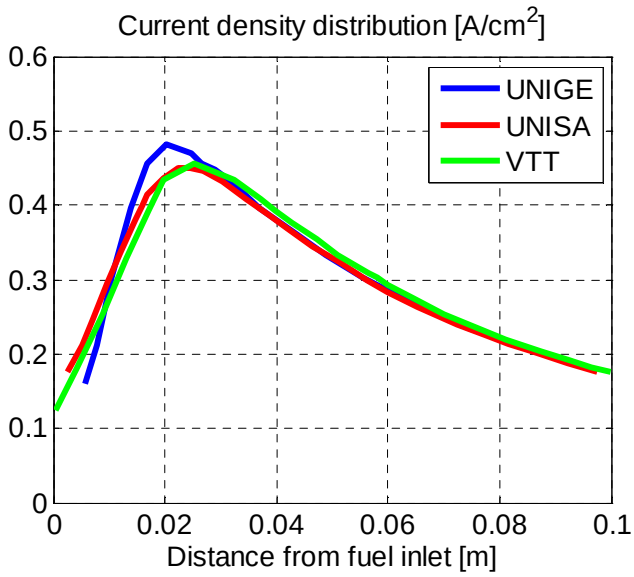

Fig. 2.11 – Example of current density profiles on the cell, estimated by the compared models, in conditions: current density 0.35 A/cm^2, fuel utilization 60%, inlet gas temperature 750 °C and ceramic solid phase.

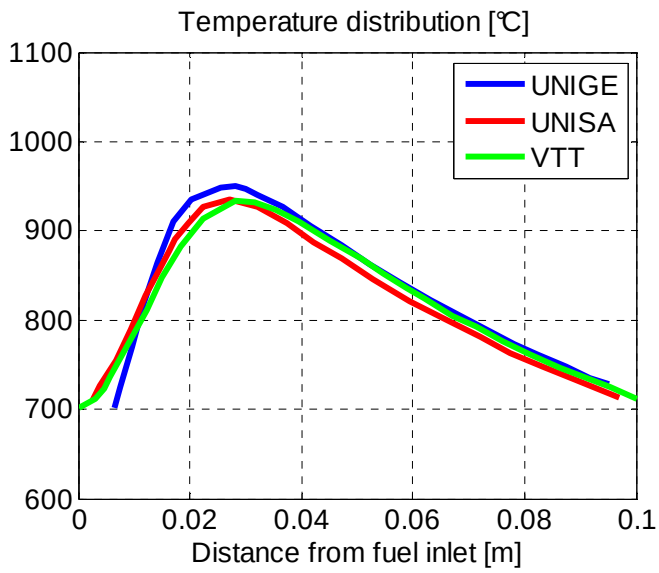

Fig. 2.12 - Example of cell temperature profiles on the cell, estimated by the compared models, in conditions: current density 0.35 A/cm^2, fuel utilization 60%, inlet gas temperature 750 °C and ceramic solid phase.

The assumptions made on the solid phase had a significant effect on the simulation results, especially on the cell temperature and, consequently, on the current density profiles. Fig. 2.13 shows an example of how the estimated cell current density profiles change (for every model) when the solid phase parameters were changed from metallic (top) to ceramic (bottom). The main difference was that metallic materials were significantly better thermal conductors than ceramic materials. The difference was also fortified by the porosity of the ceramics. As results of the improved heat transfer, the cell current density profiles were significantly smoother in the case when the solid was considered to be closer to a metal than a ceramic material.

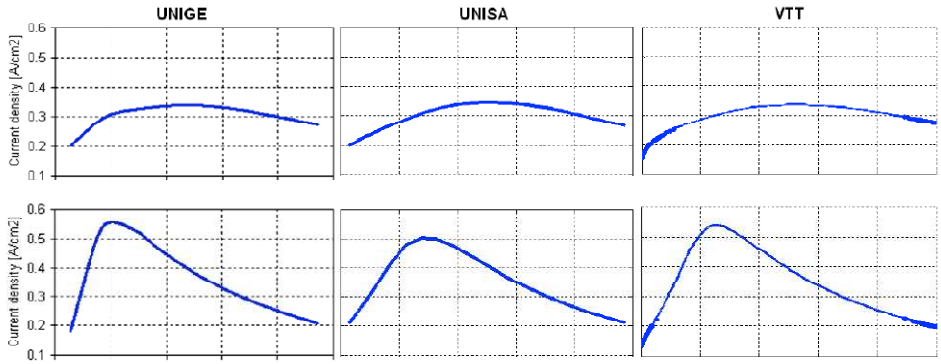

Fig. 2.13 - Example of current density profiles obtained from simulation experiments in solid phase configuration (top) and in ceramic configuration (bottom) in the operating conditions: current density 0.35 A/cm^2, fuel utilization 60%, inlet gas temperature 750 °C.

The cross-validation of three independently 1-D SOFC models carried out and the differences in the observed simulation results underlined the functioning of the 1-D model developed. The results justify using the 1-D model for developing model-based fault detection. Particularly in the next section is discussed the involving of the model into a model-based to identify the cell degradation.

2.4 Diagnostic application

The model was tested to verify the possibility to identify the Ohmic resistance of the electrochemical black-box sub-model (Marra et al., 2010).
The methodology was based on the inversion of a 1-D SOFC stack model by means of an optimization algorithm. Modeling features allowed simulating both co- and counter-flow planar SOFC with a good compromise between accuracy and computational burden, thus resulting particularly suitable for implementation in optimization algorithms. The target of this methodology was to identify the model parameters that were not directly measurable in the real SOFC system, e.g. electrolyte and electrode Ohmic resistance. The optimization inputs were the real-system measurable variables, such as stack voltage and current, inlet and outlet mass flows and temperatures. Once unmeasurable variables were identified, they had to be compared to corresponding reference values to generate suitable residuals, depending on which SOFC stack faulty conditions should be eventually detected and isolated and the stack degradation state should be estimated.

2.4.1. Degradation model: parameter identification

In the Ohmic resistance estimation, only the electrolyte resistivity was considered. This is dominant in an electrolyte-supported cell. In the degradation model a coefficient K was identified to estimate the increase in the electrolyte resistivity with respect to the normal value. The identification procedure is schematized in Fig. 2.14. In a real system, for on-field diagnosis, only measurable variables must be considered. Therefore V and T_C were selected for K identification.

$$\sigma_{el} = K \cdot \frac{3.34 \cdot 10^4}{T_s^i} \exp\left(\frac{-10300}{T_s^i} \right) \tag{2.52}$$

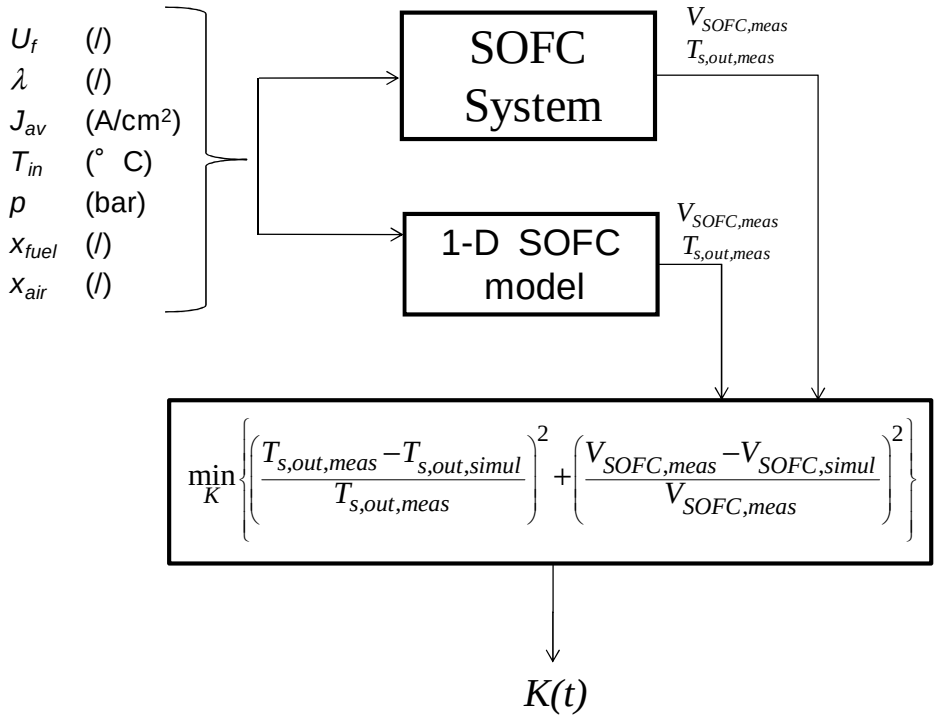

Fig. 2.14 – Degradation parameter identification scheme

2.4.2. Model setup

1-D model was setup to simulate the real system in faulty conditions. Two different scenarios were considered:

i. a distributed increase of the electrolyte resistivity has been set to 20%;
ii. a local increase of the electrolyte resistivity has been set to 20%.

The operating conditions and the geometric data are reported in Tab. 2.5.

Cell data	
Geometric data	
Active Area	100 [cm^2]
Anode thickness	50 [μm]
Cathode thickness	50 [μm]
Electrolyte thickness	500 [μm]
Operating conditions	
Cell voltage	0,6434 [V]
Cell current	30 [A]
Gas inlet temperature	900 [°C]
Fuel Utilization	85%
Excess air	7
Pressure	1 [bar]

Tab. 2.5 – 1-D model setup for degradation parameter identification. IEA Benchmark (Braun, 2002)

2.4.3. Results

In case a distributed increase in cell resistivity occurs, the inverse model yields a value of *K* equal to 1.2001. The comparison of resistivity distribution in normal and faulty operation is shown in Fig. 2.15. This is the first important result as it demonstrates how cell resistivity estimation in planar SOFC can be suitably identified via 1-D modeling, using measurable variables as input. Moreover, Fig. 2.16 shows that cell temperature difference between normal and faulty conditions is maximum at the cell outlet. Such an observation confirms the suitability of the outlet temperature to monitor Ohmic-related distributed faults in solid oxide fuel cells. If the cell temperature is controlled by a closed loop system the

outlet temperature difference (see Fig. 2.16) would be defeated. But there would be an increase in the excess air at cathode inlet, which is an input of the inverse model (see Fig. 2.14), therefore the curve of resistivity would be similar to that identified in faulty conditions without a temperature controller (red line in Fig. 2.15), highlighting the difference from normal conditions and therefore the presence of a fault.

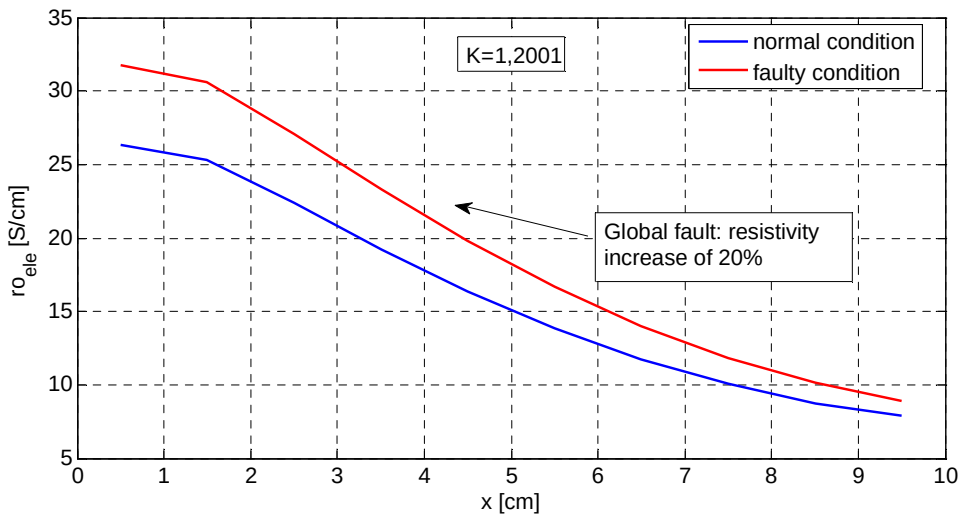

Fig. 2.15 - Cell resistivity spatial distribution in normal and faulty conditions for a global increase of electrolyte resistivity.

When a local increase in cell resistivity is considered, the diagnosis procedure yields a value of K=1,0176, which is a medium value as the fault should be distributed on the entire cell length (green line in Fig. 2.17). It is important noting that in both faulty conditions considered, which are substantially different, the diagnostic procedure can identify a value of electrolyte resistivity, specifically the value of K, which is indicative of the deterioration of the cell. The K values for the two cases analyzed above are different (Tab. 2.6), but in both cases it is possible to discriminate the curves of electrolyte resistivity in faulty and normal conditions, thus allowing reliable detection of a fault in the cell.

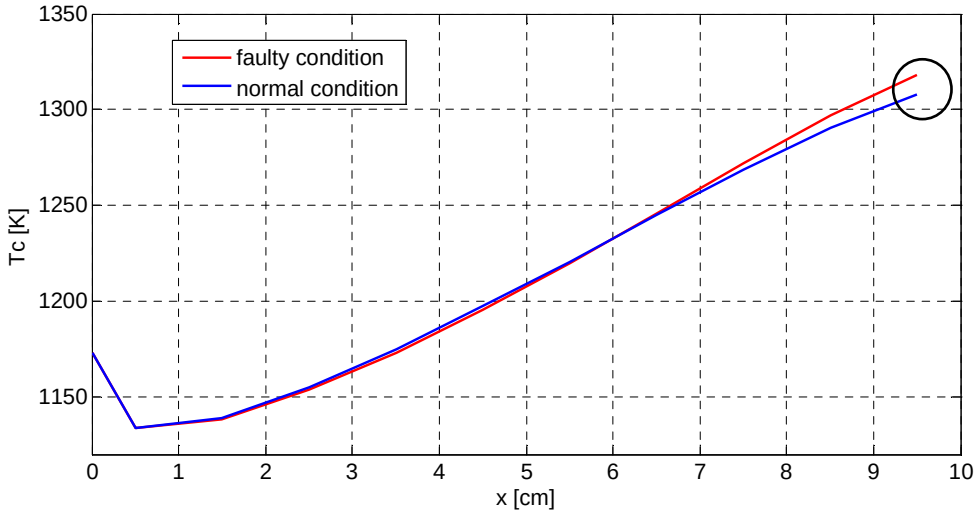

Fig. 2.16 - Cell temperature spatial distribution in normal and faulty conditions

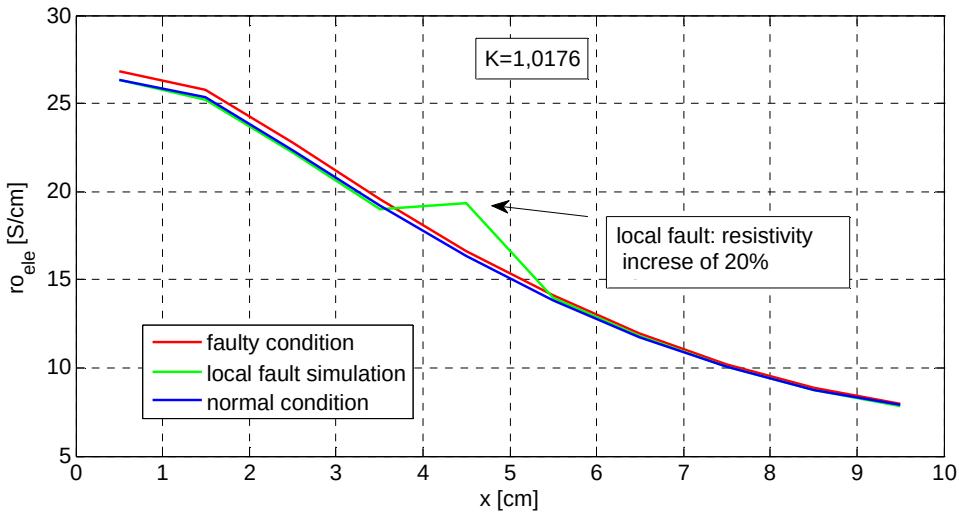

Fig. 2.17 - Cell resistivity spatial distribution in normal and faulty conditions for a local increase of electrolyte resistivity

Global increase of 20% of electrolyte resistivity	Local increase of 20% of electrolyte resistivity
K=1.2001	*K*=1.0176

Tab. 2.6 - Values of *K* for a global and local increase of 20% of electrolyte resistivity

CHAPTER 3 Grey-box SOFC Stack modeling

The aim of the grey-box modeling is to develop model-based tools aiming at optimal design, management, control and diagnosis of SOFC units destined to a wide application area (Sorrentino et al., 2009 (a)). The grey-box method is based on a priori knowledge concerning the process and on the mathematical relations which describe the behavior of the system. This means that the starting point is a specific model structure based on physical relations. The construction procedure of a grey-box model based on mathematical relations can be divided into different sub-procedures: basic modeling, experiment on the system, calibration and validation (Sohlberg et al., 2003). The flexibility of a grey-box model allows to extract rules that describe the behaviour of a device.
In order to develop SOFC stack models aimed at the implementation into control-oriented system models the lumped approach was considered the most appropriate between all the possible grey-box ones. In the lumped models spatial variations are not taken into account (i.e. 0-D models) and they are based on simplified assumptions and practical information. In such a system, the single elements, for instance, compressors, heat exchangers, fuel reformer, partial oxidizers, and contaminant removal apparatus are simulated through independent box models (Bove et al., (2006)). Furthermore, they allow being easily calibrated and modified for similar systems with different technology (e.g. different materials). This latter aspect is fundamental in the frame of the EU project GENIUS, whose main purpose is to develop “Generic diagnostic instruments for SOFC systems”. The “generic” term refers to the flexibility of diagnosis tools to be adapted to different SOFC systems.

3.1 Lumped model

The lumped model proposed was based on simplifying assumptions

whose validity was supported by previous studies. Starting from the modeling approach proposed Sorrentino et al., (2008, 2009(a), 2009(b)) a dynamic lumped model to simulate thermal response of TOPSOE SOFC stack, particularly the air temperature at cathode outlet, was developed.
The model was obtained considering the following simplifying assumptions: i) negligible pressure drop across the cell (Burt et al., 2004); ii) the variation of gases' sensible heat is neglected; iii) the dynamics of both electrochemistry and mass transfer is much faster than thermal dynamics (Achenbach, 1995); iv) since in planar co-flow SOFC fuel, air and solid temperatures do not differ significantly (Iwata et al., 2000), the temperature of the solid trilayer is assumed as representative of the entire control volume; v) $T_{ca,out}$ is assumed as the state variable; vi) the outlet fuel composition species are considered in chemical equilibrium and the methane is supposed to be totally reformated into the stack.
The SOFC thermal dynamics was modeled applying, according to the hypotheses, the energy conservation principle to the lumped stack control volume (see Fig. 3.1). This allow describing the dynamic behavior of the SOFC stack as a first order system:

$$K_{stack}\frac{dT_{ca,out}}{dt} = \dot{E}_{s,in} - \dot{E}_{s,out} + \dot{Q} - V_{stack}\cdot I_{stack} \tag{3.1}$$

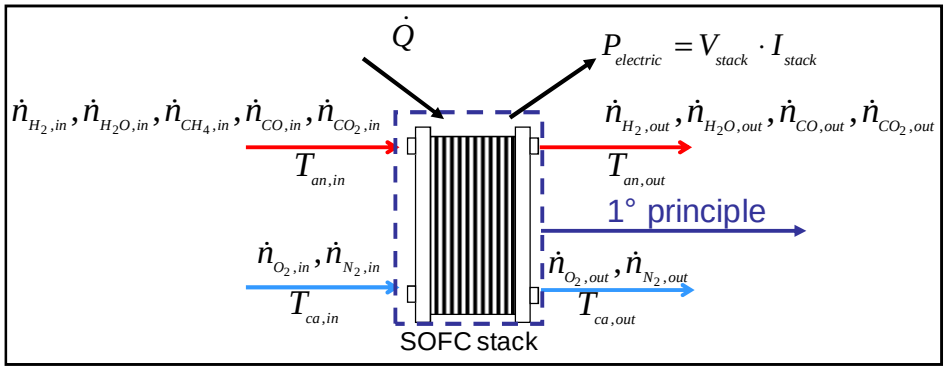

Fig. 3.1 – Lumped model control volume: 1° principle scheme.

Where K_{stack} (J/K) is the lumped SOFC stack heat capacity; $\dot{E}_{s,in}$ and $\dot{E}_{s,out}$ are the gases flows energy at the inlet and outlet of the stack respectively, calculated as follows (Sorrentino, 2006):

$$\begin{aligned}\dot{E}_{s,in} &= \dot{n}_{an,in} \cdot \Big[x_{H_2,in} \cdot h_{H_2}(T_{an,in}) + x_{H_2O,in} \cdot h_{H_2O}(T_{an,in}) + \\ &+ x_{CH_4,in} \cdot h_{CH_4}(T_{an,in}) + x_{CO,in} \cdot h_{CO}(T_{an,in}) + x_{CO_2,in} \cdot h_{CO_2}(T_{an,in}) \Big] \\ &+ \dot{n}_{ca,in} \cdot \Big[x_{O_2,in} \cdot h_{O_2}(T_{ca,in}) + x_{N_2,in} \cdot h_{N_2}(T_{ca,in}) \Big]\end{aligned} \tag{3.2}$$

$$\begin{aligned}\dot{E}_{s,in} &= \dot{n}_{an,out} \cdot \Big[x_{H_2,out} \cdot h_{H_2}(T_{an,out}) + x_{H_2O,out} \cdot h_{H_2O}(T_{an,out}) \\ &+ x_{CH_4,out} \cdot h_{CH_4}(T_{an,out}) + x_{CO,out} \cdot h_{CO}(T_{an,out}) + x_{CO_2,out} \cdot h_{CO_2}(T_{an,out}) \Big] \\ &+ \dot{n}_{ca,out} \cdot \Big[x_{O_2,out} \cdot h_{O_2}(T_{ca,out}) + x_{N_2,out} \cdot h_{N_2}(T_{ca,out}) \Big]\end{aligned} \tag{3.3}$$

$\dot{Q}$ represents the heat losses of the stack; $V_{stack} \cdot I_{stack}$ is the electric power generated by the stack. In Eq. (3.1) the accumulation term on the left side $K_{stack} \dfrac{dT_{ca,out}}{dt}$ only accounts for the heat stored by the solid part, as a consequence of hypothesis ii). Owing to the lumped nature of Eq. (3.1) and the simplifying modeling assumptions, it is required to identify the model parameter K_{stack}, which was assumed to be equal to the heat capacity of the solid parts) (i.e. cell trilayer and interconnect) (Braun, 2002.

The mole flow rates $\dot{n}_i$ and the gas concentrations $\dot{x}_i$ at stack outlet are calculated solving the system equations (3.4). Where $\dot{r}^i_{ref}$, $\dot{r}^i_{shift}$ and $\dot{r}^i_{ox}$ are the reaction rates (mol/s) of the methane reforming Eq.(1.3), water-gas shift Eq. (1.4) and electro-oxidation Eq. (1.5) reactions respectively. The concentrations at the anode outlet are considered to be in chemical equilibrium. The K_{shift} is the equilibrium constant of the water gas shift reaction Eq. (1.4) and according to the Eq. (2.16) is calculated as a function of the stack temperature at the outlet section, which is considered to be equal to the gas temperature at anode outlet.

$$\begin{cases} \dot{n}_{H_2,out} = \dot{n}_{H_2,in} + 3 \cdot \dot{r}_{ref} + \dot{r}_{shift} - \dot{r}_{ox} \\ \dot{n}_{CO,out} = \dot{n}_{CO,in} + \dot{r}_{ref} - \dot{r}_{shift} \\ \dot{n}_{CO_2,out} = \dot{n}_{CO_2,in} + \dot{r}_{shift} \\ \dot{m}_{H_2,out} + \dot{m}_{H_2O,out} + \dot{m}_{CH_4,out} + \dot{m}_{CO,out} + \dot{m}_{O_2,out} = \dot{m}_{H_2,in} + \\ \qquad + \dot{m}_{H_2O,in} + \dot{m}_{CH_4,in} + \dot{m}_{CO,in} + \dot{m}_{O_2,in} \\ K_{shift} = \dfrac{x_{H_2,out} \cdot x_{CO_2,out}}{x_{CO,out} \cdot x_{H_2O,out}} = \dfrac{\dot{n}_{H_2,out} \cdot \dot{n}_{CO_2,out}}{\dot{n}_{CO,out} \cdot \dot{n}_{H_2O,out}} \end{cases} \tag{3.4}$$

The main purpose of the models developed in this thesis is for of diagnostic, monitoring and control applications. In the lumped model developed the aim was to estimate the air temperature at cathode outlet. In the lumped model of Eq. (3.1) some variable were measured and other estimated by means of sub-models.

The lumped model parameters were identified and validated on the stack produced by TOPSOE, whose data were provided in the frame of the GENIUS project. The data sets used to identify the parameters and to validate the model were the data set 1 and the data set 2, which correspond to the TOPSOE 2nd and 3rd test rounds data respectively, available in the GENIUS project (see Tab. 3.1).

The selection of measured and computed variables was performed evaluating the balance between costs of measurement instrumentation and opportunities to substitute them with virtual sensors with appropriate features (i.e. accuracy, computational burden).

In the system under consideration with reference to Eq. (3.1) the measured variables were: the stack current, the gas temperature at the stack inlet, the gases composition at the stack inlet and the stack voltage, all the other variables were simulated.

Company	Data set Thesis	Data set GENIUS project
TOPSOE	data set 1	2nd test round
TOPSOE	data set 2	3rd test round

Tab. 3.1 – Experimental data sets provided by TOPSOE

3.1.1. Stack heat flows sub-models

In order to estimate the heat flows in the stack a black-box model based on a multiple linear regression was developed. In order to define the structure of the black-box model the control volume of the stack was divided into two control volumes (see Fig. 3.2). The heat flows model is expressed as follows:

$$\dot{Q} = K_1 \cdot (T_{ext} - T_{ca,in}) + K_2 \cdot (T_{ext} - T_{ca,out}) \tag{3.5}$$

Where T_{ext} is the external temperature and $T_{ca,in}$ and $T_{ca,out}$ represent the air temperature at the inlet and outlet of the SOFC stack. According to the hypothesis iv) SOFC fuel, air and solid temperatures do not differ significantly, thus $T_{ca,in}$ and $T_{ca,out}$ represent the temperature of the inlet and outlet sections of the stack. The model of Eq. (3.5) is the sum of two contributions to heat flows. The first term of the right hand side represent the heat flux between the stack inlet section and the external environment ($\dot{Q}_1$) and the second term represent the heat flux between the stack outlet section and the external environment ($\dot{Q}_2$) (see Fig. 3.2). The global heat flux between the stack and the external ambient is the weighted sum of these two terms and the weights are expressed by the coefficients K_1 and K_2. These coefficients are function of the SOFC stack operating conditions. The function dependencies with respect to stack operating conditions are expressed by two multiple linear regressions, described in the next section.

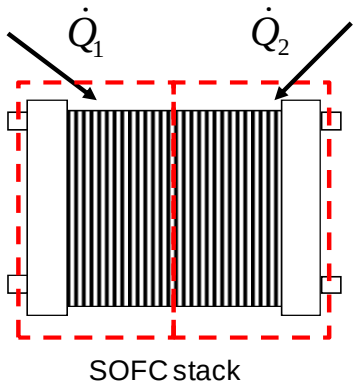

Fig. 3.2 – Stack heat flows model scheme

The model (3.5) can be considered as the full convective heat flux between the stack and the external environment and the "*driving force*" can be expressed by an equivalent temperatures difference:

$$\dot{Q} = (K_1 + K_2) \cdot (T_{ext} - T_{stack,eq}) \tag{3.6}$$

Where $T_{satck,eq}$ is an equivalent lumped temperature of the stack. From Eq. (3.6) $T_{stack,eq}$ is calculated as follows:

$$T_{stack,eq} = T_{ext} + \frac{\dot{Q}}{(K_1 + K_2)} \tag{3.7}$$

$T_{stack,eq}$ is function of the operating conditions, and it is the temperature weighted between the inlet and outlet stack sections temperatures.

Parameters identifications

The K_1 and K_2 parameters were estimated for each operating condition by minimizing an error quantity derived after the comparison between the heat flows $\dot{Q}$ estimated on the real system (left hand side term of Eq. (3.5)) and the two heat flows expressed by the right hand side term of Eq. (3.5). In order to estimate the heat flows $\dot{Q}$, 20 steady-state points were selected from a data set 1 provided by TOPSOE. According to the hypothesis (iii) the dynamics of both electrochemistry and mass transfer were considered much faster than thermal dynamics, thus to choose the steady-state points the stack temperature was considered (see Fig. 3.3). In these points the heat losses $\dot{Q}$ were calculated from stack energy balance (i.e. Eq. (3.1)) after imposing steady-state conditions (Eq. (3.8)):

$$\begin{cases} K_{stack} \dfrac{dT_{ca,out}}{dt} = \dot{E}_{s,in} - \dot{E}_{s,out} + \dot{Q} - V_{stack} \cdot I_{stack} \\ K_{stack} \dfrac{dT_{ca,out}}{dt} = 0 \end{cases} \tag{3.8}$$

Thus the heat losses $\dot{Q}$ in steady-state conditions is calculated as follows:

$$\dot{Q} = \dot{E}_{s,in} - \dot{E}_{s,out} - V_{stack} \cdot I_{stack} \tag{3.9}$$

The selection of the steady-state points was limited to a little range of stack temperature variation, as it is shown in Fig. 3.3. The warm-up and shut-down phases were not included for two reasons: in these phases there were not steady-state points and the model was calibrated to run in a limited range of stack temperature near 750 °C.
Once the heat losses were estimated for the 20 steady-state points, the coefficients K_1 and K_2 were identify by minimizing the difference between the left hand side and the right hand side of Eq. (3.5). The coefficients K_1 and K_2 identified for the 20 steady-points selected are reported in Tab. 3.2.

K_1 [W/K]	K_2 [W/K]
1,9819	0,7083
0,9252	1,0671
0,2302	1,5966
0,0568	1,7139
0,9097	1,0917
0,1672	1,4483
0,7007	1,3104
0,681	1,8011
0,5007	1,5566
0,4008	1,4986
0,5433	1,6593
1,2286	0,8656
0,8282	1,1788
0,7902	1,2286
1,1738	0,9159
0,9188	1,0842
0,7632	1,2596
0,7418	1,3174
0,0335	2,1258
-0,0923	2,3541

Tab. 3.2 – Heat flows model parameters identified.

In order to simulate the stack heat flows in all possible stack operations continuously, the coefficients K_1 and K_2 were correlated to the different operating conditions by means of two multiple linear regressions. After an analysis of the possible functional dependences, the coefficients were expressed as function of stack current density (j_{stack}), stack voltage (V_{stack}), fuel utilization (FU), and air utilization (AU):

$$\begin{cases} K_1 = f(j_{stack}, V_{stack}, FU, AU) \\ K_2 = f(j_{stack}, V_{stack}, FU, AU) \end{cases} \tag{3.10}$$

After a trial and error analysis of the possible combination of these variable the optimal multiple linear regressions were:

$$\begin{cases} K_1 = C_1 \cdot j_{stack} + C_2 \cdot V_{stack} + C_3 \cdot V_{stack} \cdot j_{stack} + C_4 \cdot FU + C_5 \cdot AU \\ K_2 = C_6 \cdot j_{stack} + C_7 \cdot V_{stack} + C_8 \cdot V_{stack} \cdot j_{stack} + C_9 \cdot FU + C_{10} \cdot AU \end{cases} \tag{3.11}$$

The coefficients identified by minimizing Eq. (3.5) represent the reference values to identify the 10 coefficient of the regressions expressed in Eq. (3.11). For the parameters identification 12 of K_1 and K_2 values were selected randomly from the 20 available in Tab. 3.2. The models of the Eq. (3.11) were validated on the other 8 steady-state points selected.
The comparison between the coefficients K_1 and K_2 estimated by minimizing the energy balance of Eq. (3.5) and estimated by the multiple linear regressions of Eq. (3.11) are represented in Fig. 3.4 and Fig. 3.5 for the coefficient K_1 and in Fig. 3.6 and Fig. 3.7 for the coefficient K_2. The optimal results confirmed the good selection of the variables to correlate the dependency of the coefficients K_1 and K_2 from the different stack operating conditions.

The heat flows $\dot{Q}$ estimated by the Eq. (3.9) for the 20 steady-state points selected from the stack data set 1 provided by TOPSOE were compared with those estimated by the model (3.5), where K_1 and K_2 were calculated by the multiple linear regressions (3.11). Fig. 3.8 and Fig. 3.9 show the good results obtained (R^2=0.9918). It is important noting that the results represent only the model performance in steady-state conditions. In order to evaluate the dynamic performance of the heat flows model, the model

was tested for the entire transient and in order to take into account the dynamic effect also the thermal storage term $K_{stack}\frac{dT_{ca,out}}{dt}$ of the Eq. (3.1) was considered. The heat capacity of the stack K_{stack} was estimated through the system geometrical and material information provided by the manufacturer of the stack (TOPSOE) and by other partners of the GENIUS project. The value obtained is $K_{stack} \simeq 1200\ \frac{J}{K}$ was used in the Eq. (3.1). The estimated value of the stack heat capacity K_{stack} was further confirmed by minimizing the error between the experimental and simulated data.

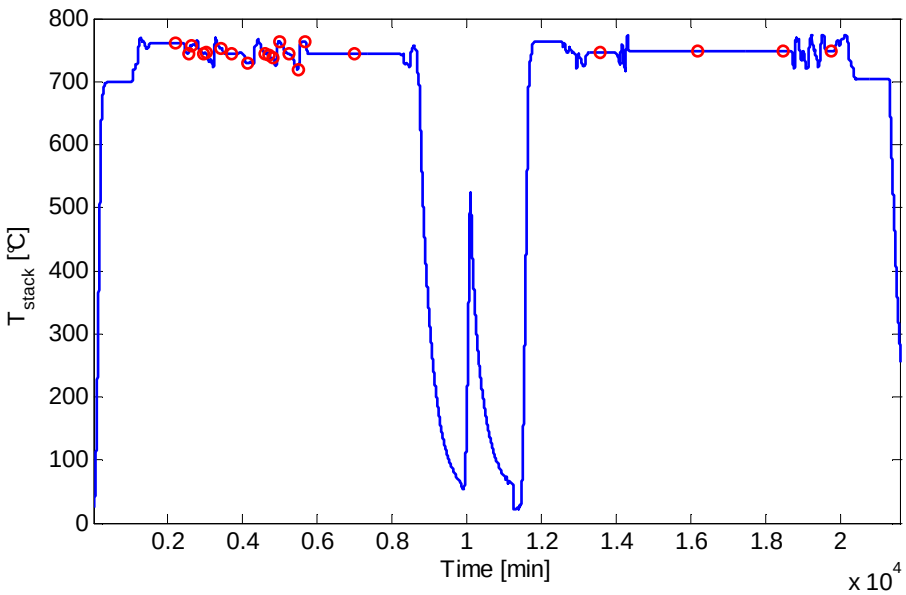

Fig. 3.3 – Steady-state points selection in the data set 1 of TOPSOE stack

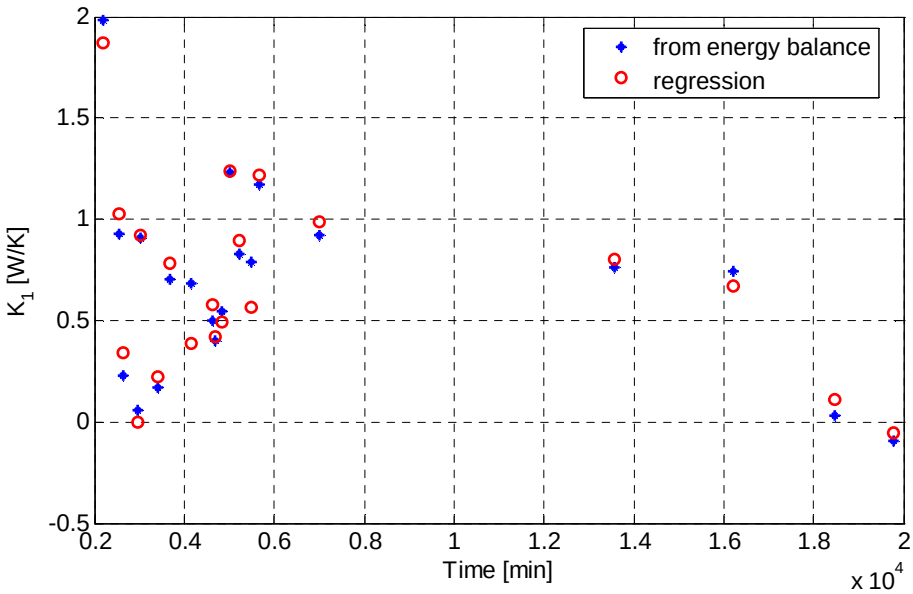

Fig. 3.4 – Comparison of heat losses model coefficient K_1 vs Time calculated by regression and by energy balance.

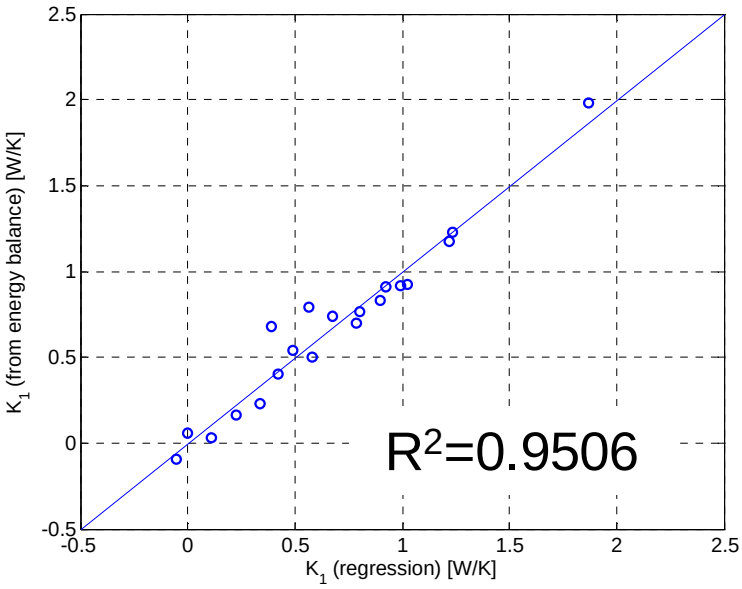

Fig. 3.5 - Comparison of heat losses model coefficient K_1 calculated by regression and by energy balance.

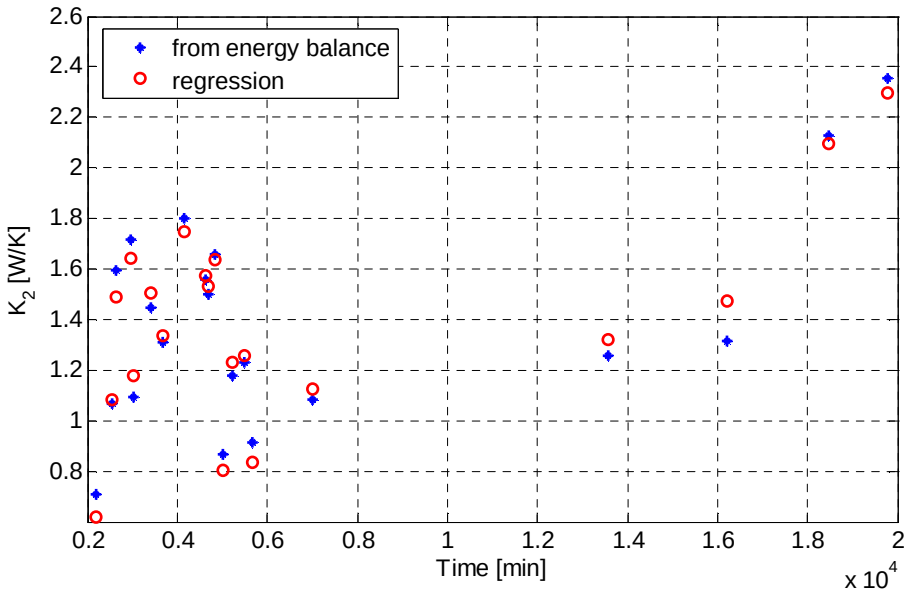

Fig. 3.6 - Comparison of heat losses model coefficient K_2 vs Time calculated by regression and by energy balance.

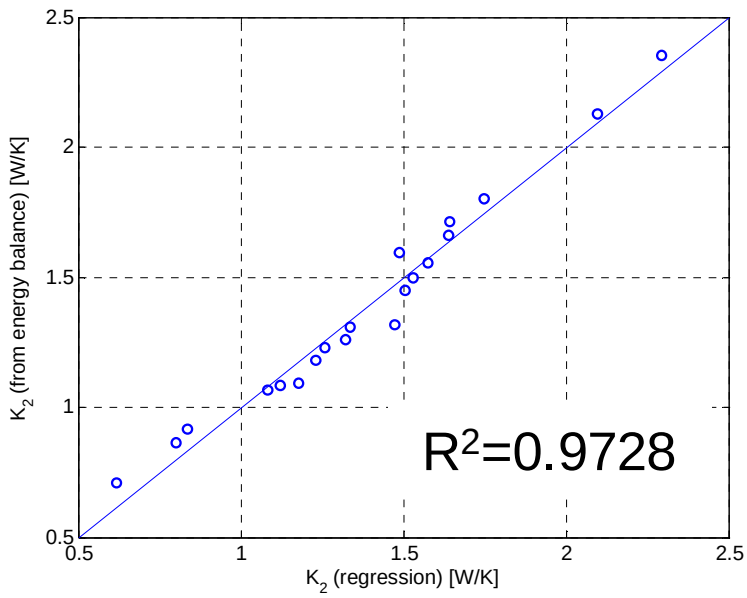

Fig. 3.7 - Comparison of heat losses model coefficient K_1 calculated by regression and by energy balance.

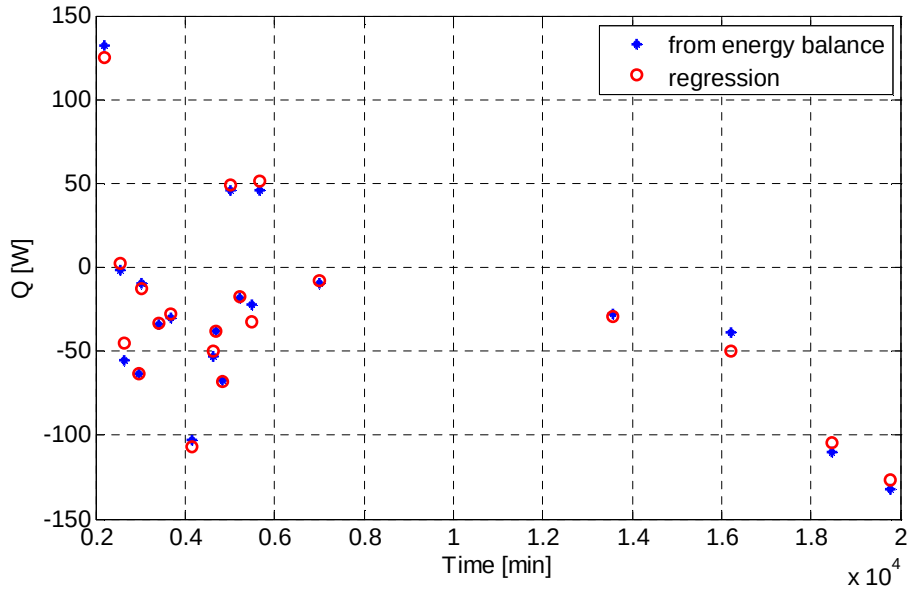

Fig. 3.8 - Comparison of heat losses model *Q* vs Time calculated by regression and by energy balance.

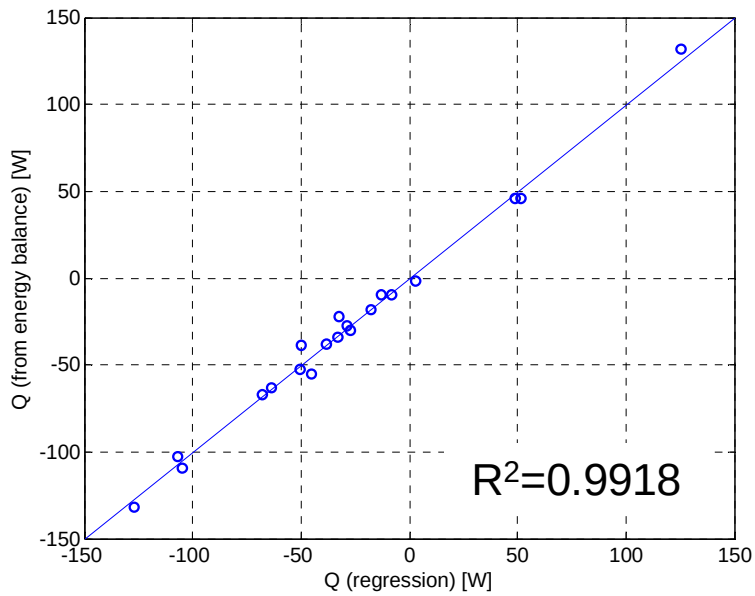

Fig. 3.9 - Comparison of heat losses model *Q* calculated by regression and by energy balance.

Heat flows sub-model results

In order to test the dynamic capability of the heat flows sub-model of Eq. (3.5), it was tested on two transients: the data set 1and the data set 2 of TOPSOE stack. In the results the left and the right side terms of the Eq. (3.1) i.e.: $\dot{Q} - K_{stack}\frac{dT_{ca,out}}{dt}$ with the term $\dot{E}_{s,out} - \dot{E}_{s,in} + V_{stack} \cdot I_{stack}$ were compared. This grouping did not change the results, because it was completely arbitrary, but allowed to put in a single group the stationary heat flows and the thermal dynamics terms. In the other term the energy flows to/from the stack were grouped together. It is important noting that in the results obtained the air temperature at cathode outlet was not simulated, but measured on the real system. This enabled to evaluate the results obtained with the heat exchange model, without the influence of the error due to temperature simulation itself. In this way there was no error superposition, allowing an evaluation of the only heat flows model only (Eq. (3.5)), and not of the entire lumped model (Eq. (3.1)).

Fig. 3.10 shows the results obtained with the heat exchange sub-model with the data set 1. The dynamic results were excellent, as shown in the different time windows of Fig. 3.11, Fig. 3.12 and Fig. 3.13. The peaks in transient phases are well simulated as the different dynamics ramps. In Fig. 3.13 it is possible noting how the model was able to simulate even small oscillation. The model was tested with the same type of comparison also for the data set 2. In Fig. 3.14 the results obtained are shown, there is an offset between the two terms represented. This was due to a different *ASR* estimated on the stack of the data set 2 than that estimated on the stack of the data set 1. This difference, even in the same operating conditions, was probably due to different materials used.

The model of heat exchange developed, being a gray-black box, showed a low attitude during extrapolation, especially in case of different materials used in the stack. In order to reduce this offset a term proportional to the difference between the *ASR* estimated in the stack of the data set 2 and that estimated in the stack of the data set 1 was introduced in the heat exchange model of Eq. (3.5). In Eq. (3.12) is reported the model of Eq. (3.5) with the term proportional to *ASR*.

$$\dot{Q} = K_1 \cdot (T_{ext} - T_{ca,in}) + K_2 \cdot (T_{ext} - T_{ca,out}) + K_3 \cdot ASR \qquad (3.12)$$

In this way the model turned out to be independent of the value of *ASR*

and acquired greater generalizability. The confirmation of the above analysis is confirmed by Fig. 3.15, where the results of the heat flows sub-model are shown. The offsets are no longer present and the error is decreased considerably.

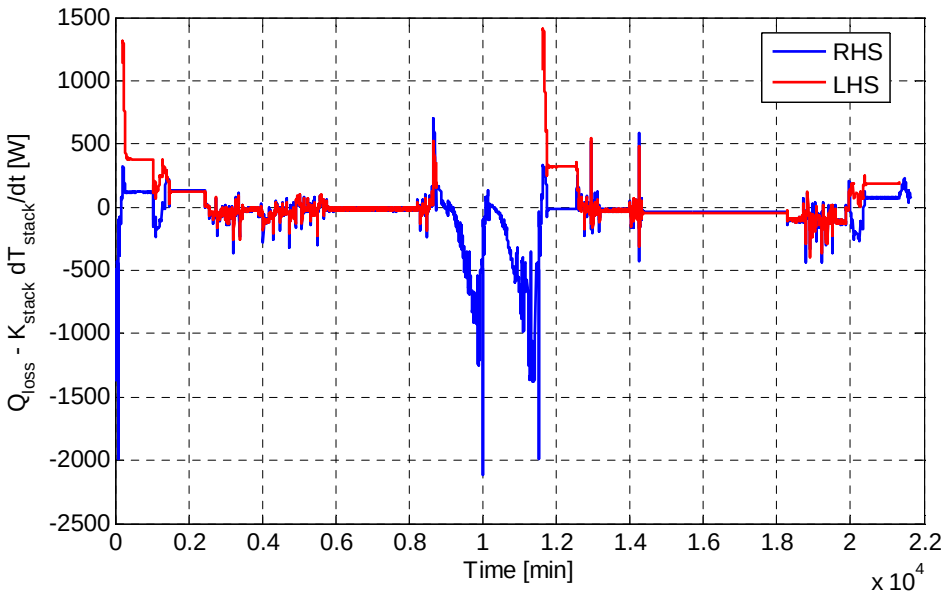

Fig. 3.10 - Comparison of heat losses model *Q* vs Time in dynamic conditions calculated by regression and by energy balance on the data set 1 of TOPSOE stack.

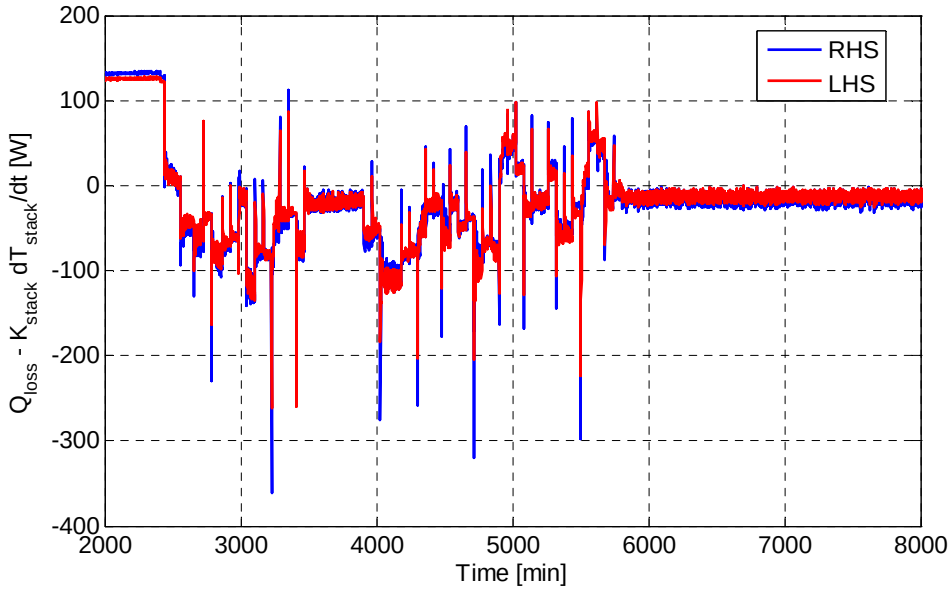

Fig. 3.11 - Comparison of heat losses model *Q* vs Time in dynamic conditions calculated by regression and by energy balance on the data set 1 of TOPSOE stack – time window [2000-8000] min.

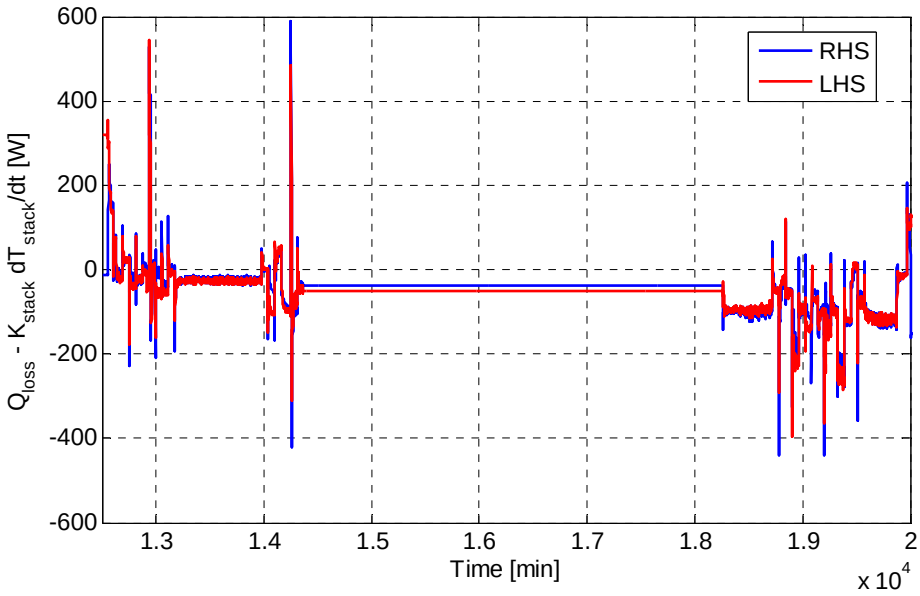

Fig. 3.12 - Comparison of heat losses model *Q* vs Time in dynamic conditions calculated by regression and by energy balance on the 2nd test round of TOPSOE stack – time window [12500-20000] min.

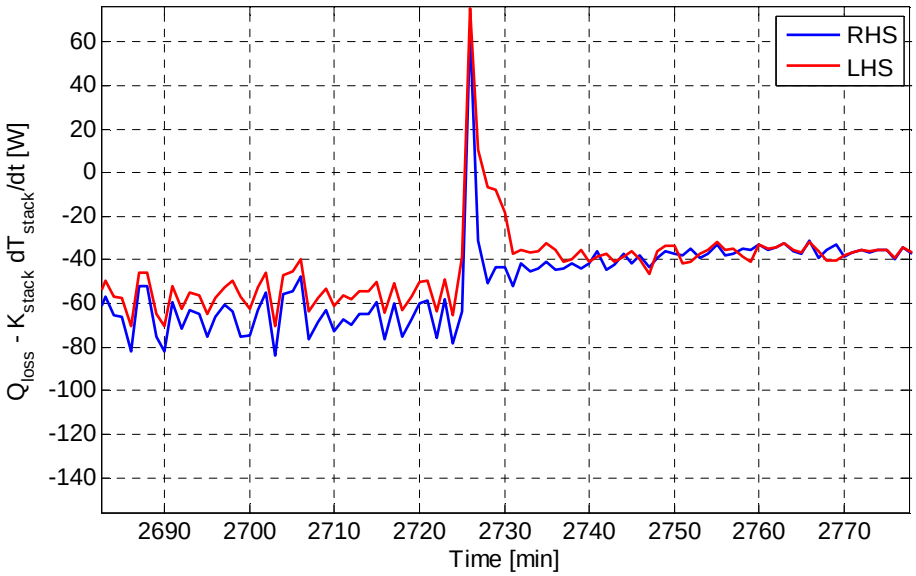

Fig. 3.13 - Comparison of heat losses model *Q* vs Time in dynamic conditions calculated by regression and by energy balance on the data set 1 of TOPSOE stack – time window [2685-2775] min.

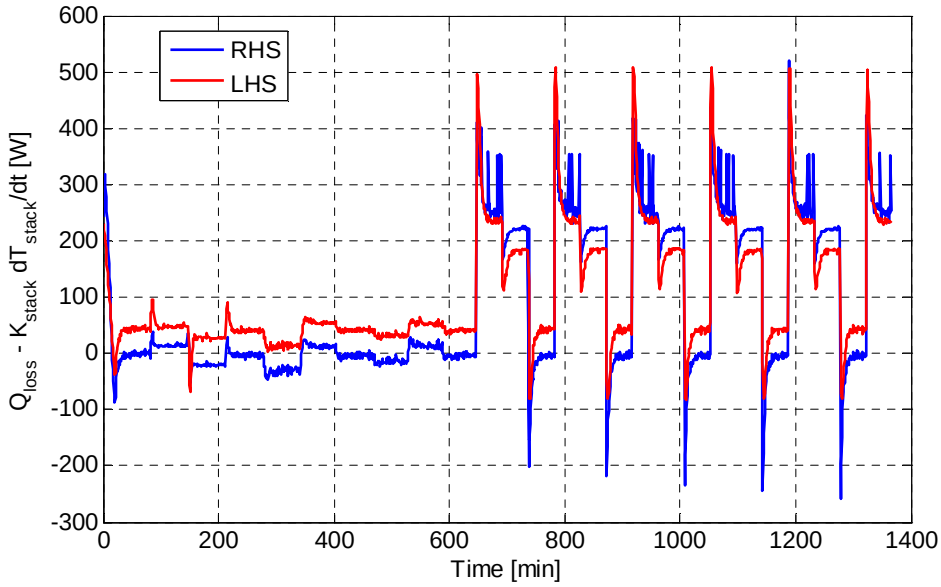

Fig. 3.14 - Comparison of heat losses model *Q* vs Time in dynamic conditions calculated by regression and by energy balance on the data set 2 of TOPSOE stack, before introduction of coefficient proportional to *ASR*.

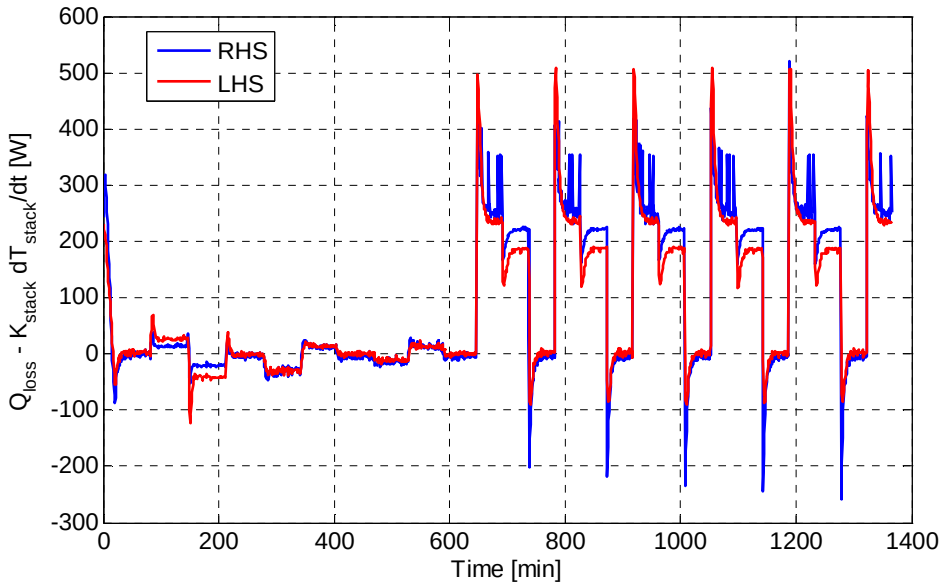

Fig. 3.15 - Comparison of heat losses model *Q* vs Time in dynamic conditions calculated by regression and by energy balance on the data set 2 of TOPSOE stack, after introduction of coefficient proportional to *ASR*.

3.2 Lumped model results

Once the heat flows model parameters were identified, the grey-box model was tested on two different transients: the data set 1 and the data set 2 of TOPSOE stack. In Fig. 3.16, is shown the simulation of air temperature at cathode outlet of the data set 1. As described before, it is worth to note that the warm up and shut down transient were not simulated. Fig. 3.17, Fig. 3.18, Fig. 3.19 show the results of the model in different time windows of the data set 1.

The results obtained show a great ability of the model to simulate both stationary values and transients. The excellent results in transient phases confirm the good estimation of the stack heat capacity K_{stack}. In the model development and then in the results obtained, a particular sensitivity of the model results with respect to the precision of the sub-model of heat exchange was noted. This led to a sub-model with sufficiently high accuracy. In Fig. 3.18 and Fig. 3.19 model results shown errors in the stationary phases. This error, which is less than 3%, is certainly to be attributed to the approximation of the heat exchange sub-model.

The results obtained with the model in the simulation of the air temperature at cathode outlet with the data set 1 are shown in Fig. 3.20. This transient tested the extrapolation ability of model. The results obtained are very good, both for stationary values and for transient maneuvers. The introduction into the heat exchange model of the term proportional to *ASR*, as before discussed, allowed to make the model more generalizable and thus good results also in extrapolation phase were obtained. The relative error for the transient considered is not more than 5%, as it is shown in the graph of Fig. 3.20.

The main feature of the lumped model is the fast and reliable procedure developed for the heat flows model and for the stack thermal dynamics. Moreover it can be easily applied to other stack with different geometries and materials.

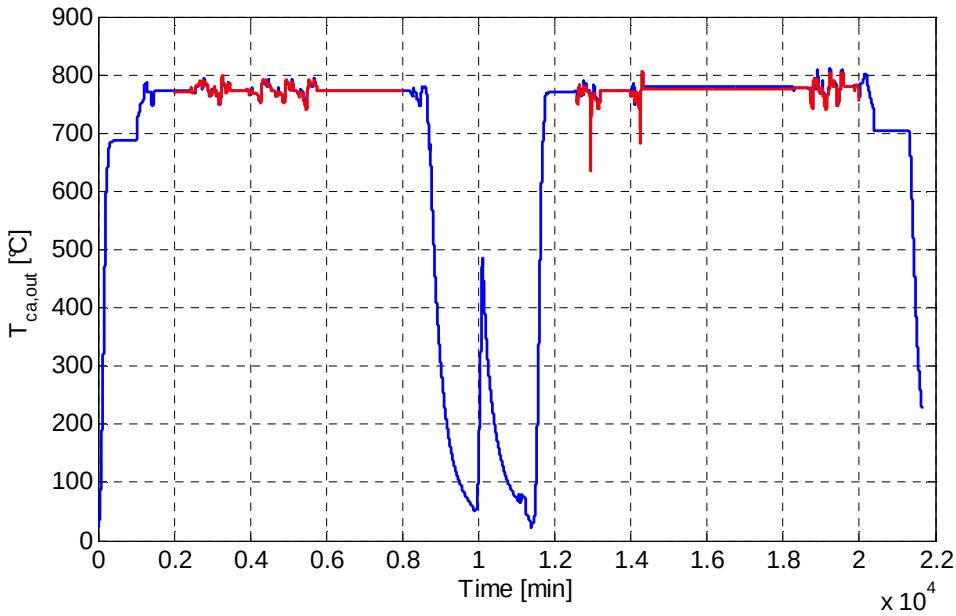

Fig. 3.16 – Comparison between measured and simulated air temperature at cathode outlet in the data set 1 of TOPSOE stack.

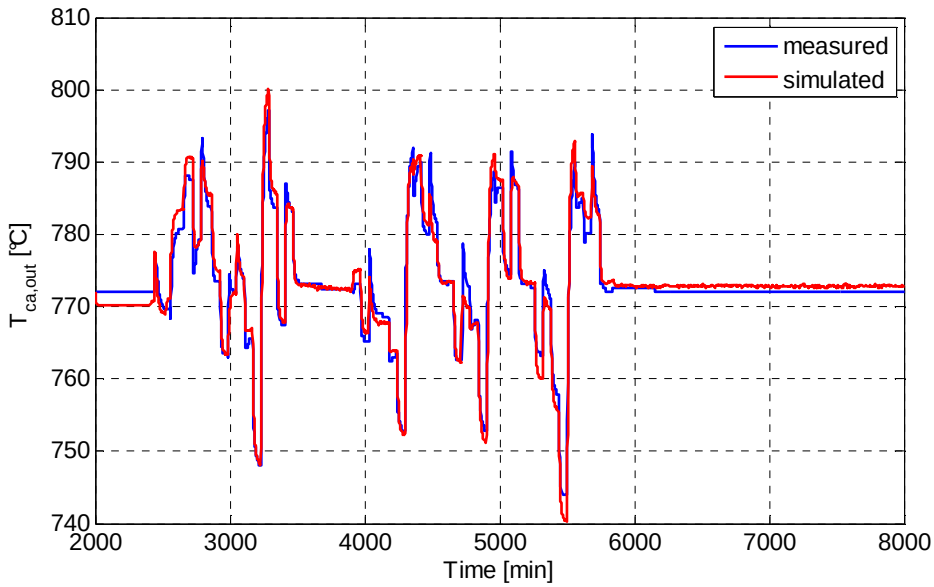

Fig. 3.17 - Comparison between measured and simulated air temperature at cathode outlet in the data set 1 of TOPSOE stack, time window [2000-8000] min.

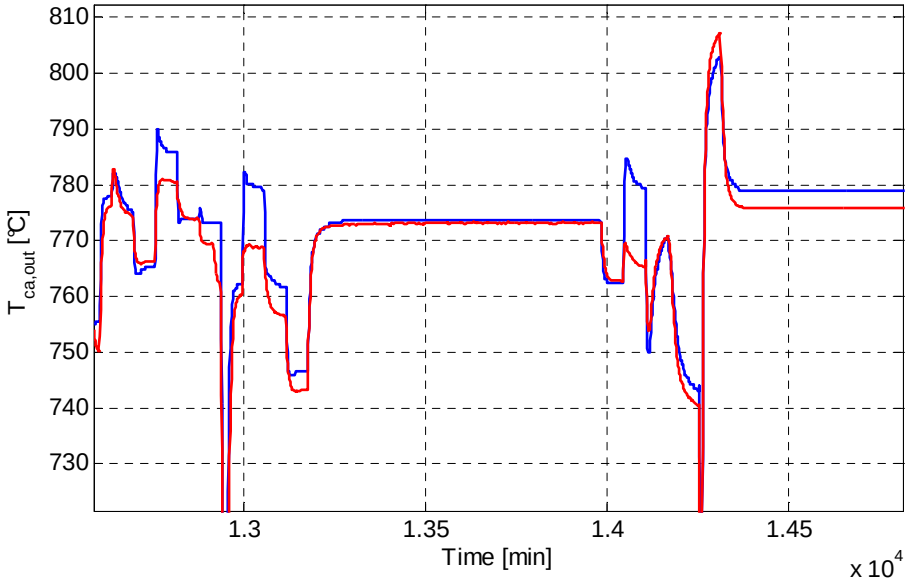

Fig. 3.18 - Comparison measured and simulated air temperature at cathode outlet between in the data set 1 of TOPSOE stack, time window [12250-14750] min.

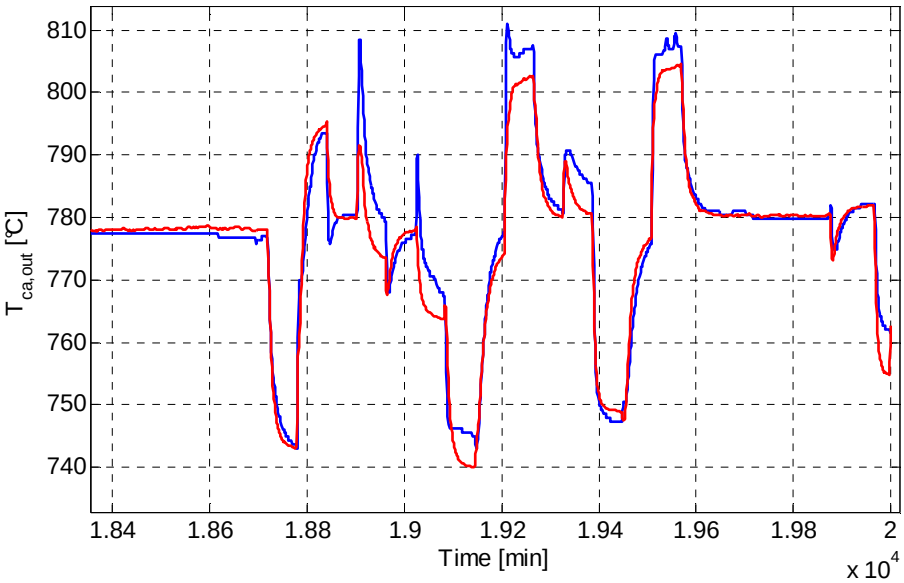

Fig. 3.19 - Comparison measured and simulated air temperature at cathode outlet between in the data set 1 of TOPSOE stack, time window [18300-20100] min.

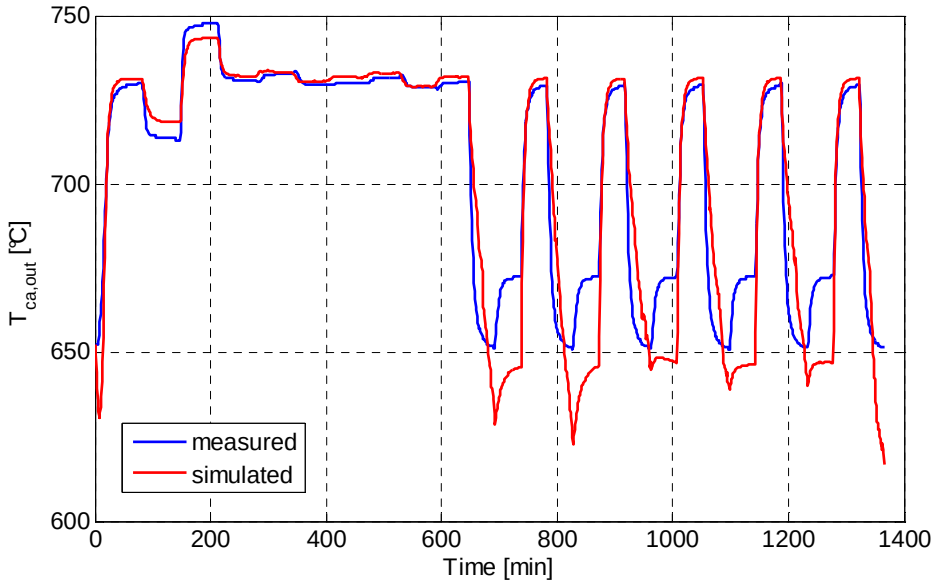

Fig. 3.20 - Comparison between measured and simulated air temperature at cathode outlet in the data set 2 of TOPSOE stack.

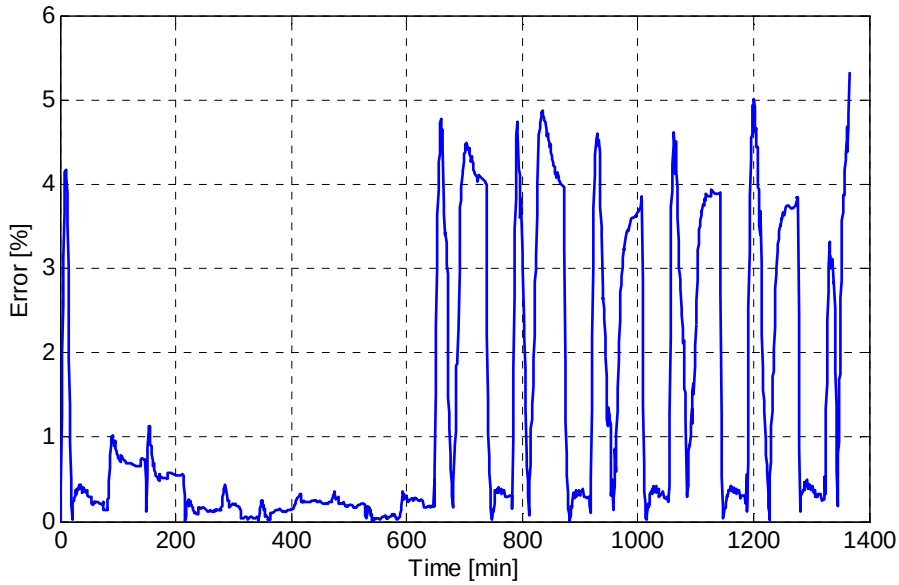

Fig. 3.21 – Relative error between measured and simulated air temperature at cathode outlet in the data set 2 of TOPSOE stack.

CHAPTER 4 Black-box SOFC Stack modeling

This chapter focuses on the experimental identification and validation of different neural network estimators of SOFC output voltage aimed at enhancing on-field diagnosis and control of SOFC-based. The models are based both on steady-state Neural Network (NN) and on dynamic Recurrent Neural Network (RNN). A NN was developed to simulate HEXIS SOFC stack voltage and two RNNs were developed to simulate TOPSOE and VTT (HTC) SOFC stack voltage.

4.1 Neural networks

An Artificial Neural Network (ANN or NN) is a non-linear black-box model able to perform a mapping between the input vector u and the output vector $\hat{y}$. The input data (i.e. the independent variables) are propagated from the input layer to the output one, through the hidden layers, to generate the corresponding output signal (i.e. the dependent variables). Each layer is composed of several elementary processing units (neurons) that work in parallel and are connected each other to create a flow of information from the input layer to the output one. These elements can be considered as single output black-box computing units with multiple inputs, where the output is obtained by processing the weighted sum of the inputs with a transfer function named activation function, which is usually a non-linear monotonic function. A detailed description of the Neural Network approach and a comprehensive analysis can be found in a previous work (Arsie et al., 2001) and in the specific literature (Patterson, 1995; Haykin, 1999; Hecht-Nielsen, 1987).
From the analogy with human brain behavior, Neural Networks are able to reproduce a process from training examples (neurocomputing approach), rather than from a coded algorithm, by simulating the process on the basis of a mathematical model (programmed computing approach) (Arsie et al., 2001). Neural Networks are able to deal with highly

uncertain input or noisy data and the experimental data required to achieve reliable models are reduced as compared with other black-box modeling approaches (Patterson, 1995).

4.1.1. Recurrent Neural Network

Recurrent Neural Networks (RNNs) are derived from static Neural Networks by considering feedback connections among the neurons. Depending upon the feedback typology, which can either involve all the neurons or only those located in the output and input layers, RNNs are classified into global, local or external recurrent neural networks (Haykin, 1999) Thus, a dynamic effect is introduced into the computational system by a local memory process. Moreover, by retaining the non-linear mapping features of the static networks, the RNN are suitable for black-box nonlinear dynamic modeling (Arsie et al., 2006). Fig. 4.1shows a scheme of the proposed RNN model structure, assuming the vector of input variables u with lag space i and one output variable $\hat{y}$ (Arsie et al., 2010 (b)). For the current applications a nonlinear dynamic output error model (NOE) based on an external RNN was selected.

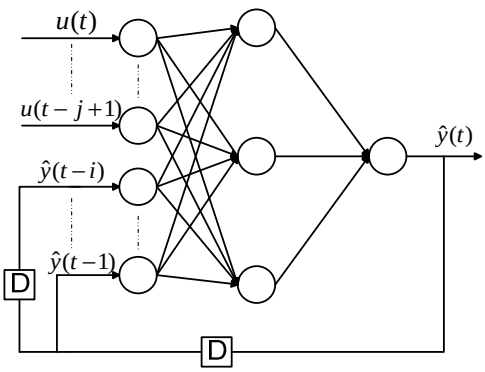

Fig. 4.1 – NOE Recurrent Neural Network scheme.

4.1.2. Neural Networks Learning approach

The parameters identification of any Neural Network (also Recurrent Neural Network) is performed through a learning process during which a

set of training examples (experimental data) is presented to the network to settle the levels of the connections between the nodes. The most common approach is the error backpropagation algorithm due to its easy-to-handle implementation. At each iteration the error between the experimental data and the corresponding estimated value is propagated backward from the output to the input layer through the hidden layers. The learning process is stopped when the following cost function, *Mean Squared Error* (*MSE*), reaches its minimum:

$$MSE(\theta) = \frac{1}{2N} \sum_{i=1}^{N} \left(\hat{y}_i(\theta) - y_i \right)^2 \tag{4.1}$$

Eq. (4.1) refers to steady-state NN, formally for Recurrent Neural Networks the cost function to calculate the *MSE* is the following:

$$E(\theta) = \frac{1}{2N} \sum_{t=1}^{N} \left(\hat{y}(t \mid \theta) - y(t) \right)^2 \tag{4.2}$$

N is the size of the training pattern gathered from available experiments. The above functions (Eqq. (4.1), (4.2)) can be carried out in either a batch or a pattern- by-pattern way. The former is usually preferred at the initial development stage, whereas the latter may be adopted online to enable network weights adaptation in response to the exogenous variations of the controlled/simulated system. The backpropagation method is a first-order technique and its use for complex networks might cause long training and in some cases a loss of effectiveness of the procedure. Therefore, in the current work both for the steady-state NN and the two RNNs developed a second-order method based on the Levenberg-Marquardt optimization algorithm is adopted (Patterson 1995; Haykin 1999; Hecht-Nielsen R. 1987; Nørgaard et al. 2000; Ripley 2000). Moreover,to limit the occurrence of overfitting for the RNN, a regularization term (Nørgaard et al., 2000) was added to Eq. (4.2), yielding the following new cost function:

$$E^*(\theta) = \frac{1}{2N} \sum_{t=1}^{N} \left(\hat{y}(t \mid \theta) - y(t) \right)^2 + \frac{1}{2N} \cdot \theta^T \cdot \alpha \cdot \theta \tag{4.3}$$

where α is the weight decay (Nørgaard et al., 2000).

The training process aims at determining NN and RNN models with a satisfactory compromise between precision (i.e. small error on the training-set) and generalization (i.e. small error on the test-set). High generalization can be guaranteed only if the training data-set is sufficiently rich, so as to cover most of the system operating domain.
As far as network structure and learning approach are concerned, the precision and generalization goals are often in conflict. The loss of generalization due to parameters redundancy in model structure is addressed in the literature as overfitting (Nelles, 2000). This latter may occur in case of a too large number of weights, which in principle improves NN (or RNN) precision but may cause generalization to decrease. A similar effect can occur if network training is stopped after too many epochs. Although this can be beneficial to precision, it may negatively impact generalization capabilities and is known as overtraining.
Based on the above considerations and to ensure a proper design of the NN and RNNs developed in this thesis, the following steps were accomplished:

i) generate a training data set extensive enough to guarantee acceptable generalization of the knowledge retained in the training examples,
ii) select the proper stopping criterion to prevent overtraining, and
iii) define the network structure with the minimum number of weights.

As for the impact of point i) on the current application, the influence of the main input variables (i.e. load and SOFC degradation over time) was satisfactorily taken into account when selecting the most appropriate training set and network inputs. Point ii) was addressed by using the early stopping criterion (Nørgaard et al., 2000). This technique consists of interrupting the training process, once the *MSE* computed on a data set different from the training one stops decreasing. Therefore, when the early stopping is used, network training and test require at least three data sets (Haykin 1999): training-set, early stopping test-set and generalization test-set. According to the early stopping method, after each iteration of the training algorithm, the error of generalization is evaluated. This error is constructed in a similar manner to the error energy (Eq. (4.1)), but calculated at the desired response of a new set of data. What is expected is

generally a situation like the one in Fig. 4.2: the training error, which is the value of the cost function *MSE* (Eq. (4.1)) applied to the training set, is monotonically decreasing as the number of iterations increases, because it uses a minimization algorithm of the type described before. The generalization error reduces only at the beginning of the process. After n^* iterations it reaches a minimum and begins to increase afterword. This is determined by the ability of the network to capture the essential features of the system at the beginning of the process, then it adapts to background noise. This phenomenon is the above mentioned overtraining not be confused with the previously described overfitting. From Eq. (4.1) the cost function *MSE* is computed over the vector length *N* and the weights are adjusted at each iteration of the optimization process (i.e. training epoch). At each epoch the NN (and RNN) evaluates the complete set of inputs belonging to the training pattern. This training procedure is known as batch learning or epochwise training to distinguish from the on-line training approache. The batch learning is well suited for off-line applications as presented in this thesis. On the other hand, in case of on-line training, the network parameters are updated while the network processes the input data, thus being suitable for adaptive applications of NN (and RNN) (Haykin, 1999; Nørgaard et al., 2000).

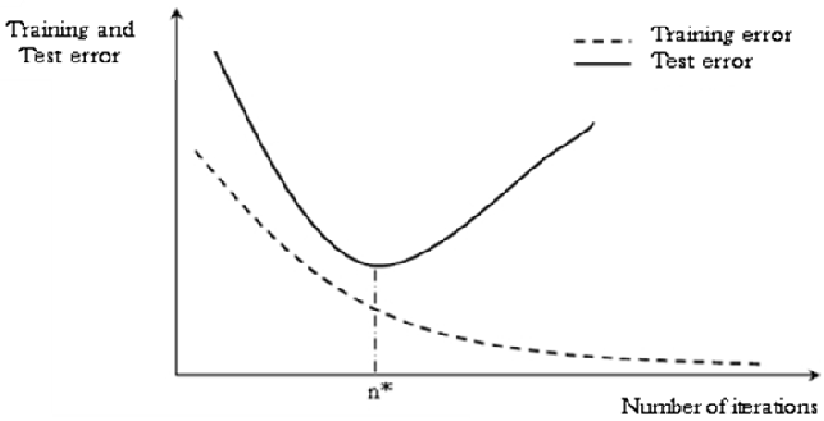

Fig. 4.2 – Comparison between training and test error vs number of training iteration (adapted from Patterson, 1995).

4.1.3. Optimal network dimension

Once the basic input variables have been determined, the network

structure can be selected by choosing the optimal number of hidden layers and neurons. Regarding the number of hidden layer has been demonstrated through the "universal approximation theorem" (theorem of existence of neural networks applied by Kolmogorov Cybenco, 1988 and Hornik, 1989) that all continuous functions can be approximated by a desired accuracy level by using a network with one hidden layer of neurons. Once the number of hidden layer is fixed to one, the number of hidden neurons must be defined. The level of accuracy achievable by the NN (or RNN) can be improved by increasing the number of hidden nodes. An increase of the number of parameters occurs with the risk of overparametrization and a loss of model generalization. In the current study, the trade-off between network accuracy and dimension has been accomplished performing a trial and error analysis on a set of possible structures.

4.2 Steady-state Neural Network model of HEXIS SOFC stack

The SOFC stack modeled in this work is a 5-cells test rig produced by HEXIS. In Tab. 4.1 the main specifications are reported (Mai et. al, 2011). The modeled stack operates at 850-900°C and consists of 100 cm^2 cells containing disk-shaped electrolyte supported cells (ESC) and metallic interconnects (MICs), see Fig. 4.3; these components are of planar design, with a round hole in the centre. Natural gas from the grid is converted by a catalytic partial oxidation (CPO) and supplied to the cells via the centre, while preheated air flows from the outside through four opposite radial channels onto the metallic interconnect. Both cathodic and anodic gas have parallel radial flows moving towards the stack periphery, thus the stack may be classified as a radial-planar co-flow. A post combustion takes place in the surrounding area of the stack (Mai et al., 2011).

Fuel cell	
Output	about 95 W
Type	Solid oxide feul cell (SOFC)
Fuel	Natural gas
Fuel processing	Catalytic partial oxidation (CPO)
Configuration	Radial co-flow

Tab. 4.1 - Main specifications of the 5-cells test rig.

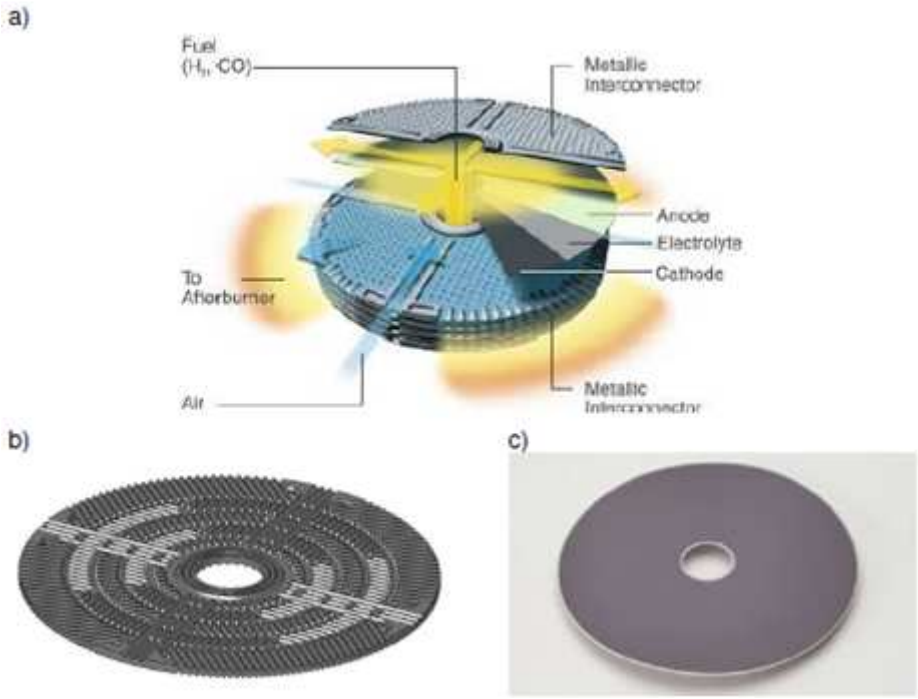

Fig. 4.3 - a) stack sketch; b) metallic interconnect (MIC); c) electrolyte supported cell (ESC) (Mai et al., 2011).

4.2.1. Neural Network input selection

For the definition of the input variables of a black-box model, the knowledge of the main phenomena occurring into the system being modeled is required; from a methodological point of view the authors have exploited the experience gained in other researches devoted to the

black-box modeling of energy systems (Arsie et al., 2006). In the model developed, the stack voltage was the output and it was mapped with respect to the input variables of the model. Before describing the physical relationship among stack voltage and operating, control and state variables, It is worth noting that an accurate selection of these variables was performed to avoid data redundancy, which in turn may determine an increase of model's parameters leading to a loss of generality of the model (Arsie et al., 2006). At the same time the inputs were selected to provide all the information necessary for the simulation of the output. For an effective selection of the input variables, the main electrochemical processes, described in the CHAPTER 2, were analyzed through the study of the voltage models.

The electrochemical models highlight the functional dependence of the stack voltage to some physical quantities. In a fuel cell these variables change along the flows directions and their spatial distributions are governed by energy, mass and momentum balances occurring inside the cell. With reference to the steady-state 1-D model developed, the SOFC stack voltage was expressed as a function of the following variables:

$$V_s = f(j_{stack}, T_{air,ca,in}, T_{fuel,an,in}, T_{s,in}, x_{H_2,an,in}, x_{CO_2,an,in}, x_{CO,an,in}, x_{CH_4,an,in}, x_{H_2O,an,in}, x_{O_2,ca,in}, \dot{m}_{fuel,an,in}, \dot{m}_{air,ca,in}) \quad (4.4)$$

The input species at the anode inlet were supposed to be in chemical equilibrium and their concentrations ($x_{i,an,in}$) were supposed to be related to the temperature ($T_{fuel,an,in}$) of the gas blend coming from the CPO pre-reformer and entering the anode. According to this hypothesis Eq. (4.4) can be simplified as follows:

$$V_s = f(j_{stack}, T_{air,ca,in}, T_{fuel,an,in}, T_{s,in}, \dot{m}_{fuel,an,in}, \dot{m}_{air,ca,in}) \quad (4.5)$$

According to the hypothesis assumed for the model proposed in literature (Sorrentino et al., 2008), for a co-flow configuration the temperature of the stack was supposed to be equal to that of the anode and cathode gas streams. Thus only the fuel inlet temperature was considered and the stack voltage was expressed as follows:

$$V_s = f(j_{stack}, T_{air,ca,in}, \dot{m}_{fuel,an,in}, \dot{m}_{air,ca,in}) \tag{4.6}$$

The stack was fed by methane, which was reformed through a CPO. The fuel mass flow considered as input to the model was the methane mass flow at the CPO inlet.
The choice of the methane flow rate at CPO inlet and not directly to the anode was linked to the difficulty to measure, the methane flow rate directly at the anode inlet. The methane (and hydrogen) flow rates at the anode inlet are linked to the CPO conversion efficiency. The two main factors that affect CH_4 to H_2 conversion of the CPO efficiency are the catalyst bed temperature and the ratio of the reactants (CH_4 and O_2) (Recupero et al., 1998 and Zhu et al., 2001). At proper CPO operating temperature, the amount of hydrogen created depends on the supply rate of CH_4 and the CPO air to fuel ratio, i.e., the oxygen to carbon ratio. The oxygen to carbon ratio also influences the amount of heat produced in the CPO, which then affects the CPO catalyst bed temperature and the temperature of the gas blend coming from the pre-reformer and entering the anode ($T_{fuel,an,in}$). In the present work the conversion efficiency of the CPO and thus the methane and hydrogen flow rates at anode inlet were assumed to be function of the methane flow rate at CPO inlet and of the gas blend temperature of CPO outlet.

$$\dot{m}_{fuel,an,in} = f_2(\dot{m}_{CH_4,CPO,in}, T_{fuel,an,in}) \tag{4.7}$$

According to the hypothesis assumed the stack voltage can be expressed:

$$V_s = f(j_{stack}, T_{air,ca,in}, \dot{m}_{CH_4,CPO,in}, \dot{m}_{air,ca,in}) \tag{4.8}$$

As already introduced, the SOFC stacks are characterized by complex degradation phenomena during their life causing a reduction of the stack voltage. The stack degradation is usually divided into two main classes: the steady state degradation due to the aging of stack components, which can not be avoided. The degradation can be accelerated or caused by transient operating conditions, e.g. redox- and thermo-cycling or BoP failures (Larrain et al. 2006). Degradation processes are still not completely understood and thus cannot be explicitly modelled with a black-box mapping model, unless large dedicated experiments are

available, but model generality may not be guaranteed. In order to account for the degradation the time was considered as a further input of the model. Finally the stack voltage was expressed as a function of anode inlet temperature, stack average current density, CPO inlet fuel methane mass flow, air mass flow at cathode inlet and time:

$$V_s = f(j_{stack}, T_{air,ca,in}, \dot{m}_{CH_4,CPO,in}, \dot{m}_{air,ca,in}, t) \tag{4.9}$$

The degradation causes an increase in cell polarization losses, whose effect is the rotation of the current-voltage (IV) curves in time, as shown in Fig. 4.4. The effect of natural degradation (aging) is present both in the IV curves and in long-term sets. Therefore, the time is considered as an index of the degradation. A sketch of the input-output structure of the model is shown in Fig. 4.5, where the links among input, intermediate and output computing elements (i.e. neurons) are reported.

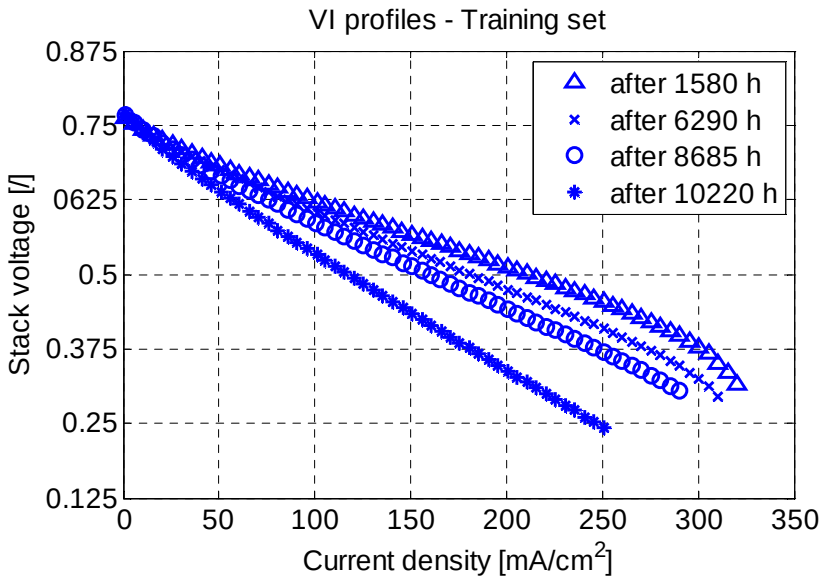

Fig. 4.4 - Stack Voltage vs Current Density at different operating hours (Training_set, VI profiles).

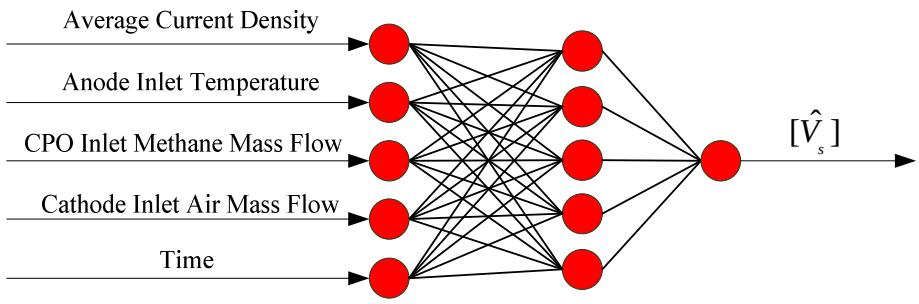

Fig. 4.5 - Sketch of the input-output model; the structure of the neural networks is described into section 2.

4.2.2. Steady-state Neural Network

A multi-layer-perceptron-feed-forward (MLPFF, Patterson, 1995) neural networks was adopted to develop an accurate model for predicting HEXIS SOFC stack voltage, as shown on Fig. 4.5. MLPFF parameters identification was performed through a second-order method based on the Levenberg-Marquardt to minimize Eq. (4.1) (Patterson 1995; Haykin 1999; Hecht-Nielsen R. 1987; Nørgaard et al. 2000; Ripley 2000). According to the early stopping criteria (described in the paragraph 4.1.2), tree data sets were selected: training-set (set A), early stopping test-set (set B) and generalization test-set (set C). Fig. 4.6 shows the evolution in time of the NN MSE on both set A and set B, highlighting how the learning process for the NN SOFC model here developed was as long as 53 epochs. Such an interruption occurred because the estimation error on set B (i.e. early stopping data set) stopped decreasing, as shown on Fig. 4.6, thus clearly indicating that the overtraining problem would have occurred if further training epochs had been performed. According to the "universal approximation theorem" the number of hidden layer was fixed. In order to prevent the NN training from the above-discussed overfitting issue, in the current work the optimal trade-off between network accuracy and dimension was accomplished through a parametric analysis by varying the number of hidden neurons from 3 to 10. This study was performed after the selection of the training set, whose details are given in the following section, leading to the definition of a neural network with 5 neurons in the hidden layer. According to the NN structure shown in Fig.

4.5 the neural network has 5 inputs, 5 hidden neurons ad 1 output; therefore the parameters of the model are 36, of which 30 weights, connecting the neurons and 6 biases, 1 per each neuron in the hidden layer and 1 on the output neuron.
In the following section the strategy adopted to ensure proper selection of training and test sets is presented and discussed in detail.

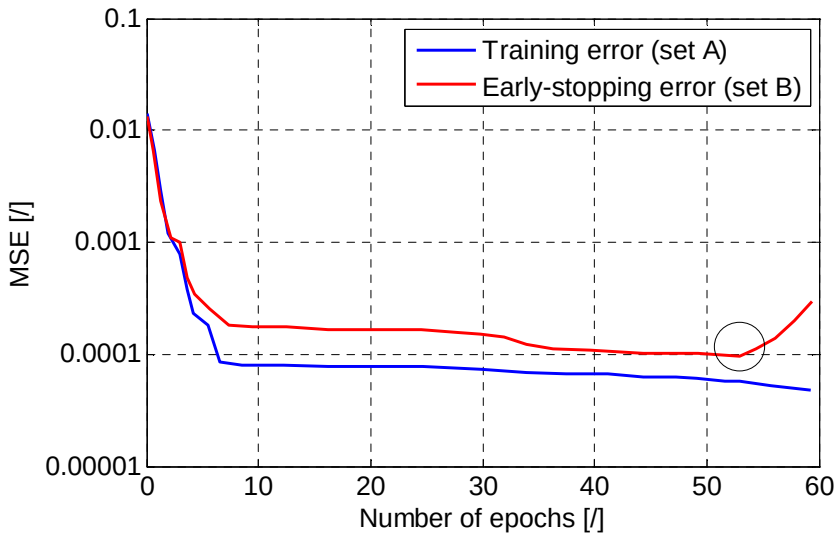

Fig. 4.6 - NN MSE of training-set and early stopping test-set vs number of epochs.

4.2.3. Training and Test data sets definition

As anticipated above and according to the system identification theory (Ljung, 1999), two sets of data should be used for the NN training and for the generalization test, respectively. To guarantee the highest generalization the two sets should be independent and their selection must be performed carefully. Same principle applies to the early stopping data set, which may be a sub-set of either the training or the test sets. Owing to the low extrapolation capabilities of the NN, it is essential that the training set spans the domain of each input variable to its largest extent. It is worth recalling that the input variables were selected following the guidelines drawn in the paragraph 4.2.1 and, according to that analysis,

the methane flow rate, the air flow rate, the temperature of the reformate fuel, the current density and the time were chosen as input variables for the neural network model. After the input variables selection, the training set must be generated in such a way to reflect the data independence principle just drafted; it has to guarantee the highest generalization with the minimum amount of training data, to avoid accuracy losses due to, e.g., the occurrence of overfitting. The selection of the training set is therefore critical and a trade-off between high number of measures and high information content of the database has to be solved. Advanced methodologies, such as experimental design (Pianese and Rizzo, 1996; Esposito et al., 2012), can support the design of experimental campaigns. Nevertheless, the generation of new data entails an analysis of costs and time needed to build the new data set, on the other hand the system might not be on operation and available data must be used. When databases are already populated, several methodologies ranging from easy-to implement random-based selection up to complex ones, such as active selection of informative data (Arsie et al., 2001) or more general data mining techniques (Gargano and Raggad, 1999; Lee and Siau, 2001), might be implemented.

SOFC stacks, which accounted for the system degradation over time. For this reason the data selected for the development of the model (i.e. training data) contained data measured continuously over a time period of few thousand hours. The Training_set (see Tab. 4.2) was recorded at Hexis premises and contains the measurements acquired over a long time interval (see Fig. 4.7). Such a data set consists of two data groups: in the first set (see red circles in Fig. 4.7) all the operating conditions are constant, whereas in the second one several voltage-current (VI) curves (blue stars) are available at different time intervals; for these latter data groups the stack control variables vary according to the different values imposed to stack current, spanning the current range from zero to its maximum value. The availability of long term and VI data makes the training data very appealing since the experimental data holds simultaneously the knowledge about the degradation process (long term data) and the behaviour of the stack at different current levels (VI curves), respectively. As a matter of fact, the availability of VI profiles recorded at different times also contributes to providing further knowledge content on degradation effect, as shown in Fig. 4.4, where the slope variation in the VI relationship due to increasing degradation clearly emerges. Thanks to

the non-linear capabilities of the neural network, the combined influence of degradation and input variables change can be simulated with high accuracy through the same model. Thus the effect degradation on SOFC stack performance can be accounted also outside the nominal operating region, making the model well suited to simulate the stack under faulty conditions, i.e. operations that are not expected during normal operations. Such capabilities are the key features of model-based monitoring and diagnosis algorithms and represent the first step towards the implementation of prognostics algorithm for stack lifetime forecast.

To improve the generalization of the neural network, data measured on two different stacks belonging to the same family (i.e. same material and geometry, Technology 1 in Tab. 4.2) were considered for the network parameters identification. The training set was constructed by joining the VI curves and long term data of the two stacks belonging to Technology 1. Care was given to cover the entire domain of the stack operating points, this was achieved by comparing the domains of the model inputs of the training set with those of the other data set (test sets). When building the training set, a balance between VI curves and long term test was pursued by selecting all the VI curves and varying afterward the number of long term data to be included. Indeed it is mandatory to avoid that long series of data at constant operation polarize the behaviour of the model; moreover, the knowledge to be transferred to the network has to be balanced among the main processes considered for the training. The optimum ratio between VI and long term points was defined through a trial and error process, evaluating the generalization errors on different test sets. The choice of long term data was done randomly by selecting single points from the entire data set. It is worth noting here that this procedure is valid for static neural network, whereas for dynamic neural network the time sequence has to be considered to simulate the dynamics of the system to be modelled (Nørgaard et al., 2000; Arsie et al., 2006). Once the training data set was created, the sub-set for the early stopping was built by picking-up randomly the 12% of the data.

After the training, the generalization capability of the neural network was tested on four additional data-sets, whose data were not used during the training. These data were recorded at Hexis on two different stacks, one with the same technology considered for the training (i.e. Technology 1 in Tab. 4.2) and another one with a different technology (i.e. different material and geometry, Technology 2 in Tab. 4.2). Therefore, the

generalization capabilities of the model were properly checked by testing the ability of the neural network to reproduce the VI curves and the voltage output of the long term sets. Overall, the network was tested on the 4 test sets shown on Tab. 4.2, consisting of 2 VI curves and 2 long term sets.

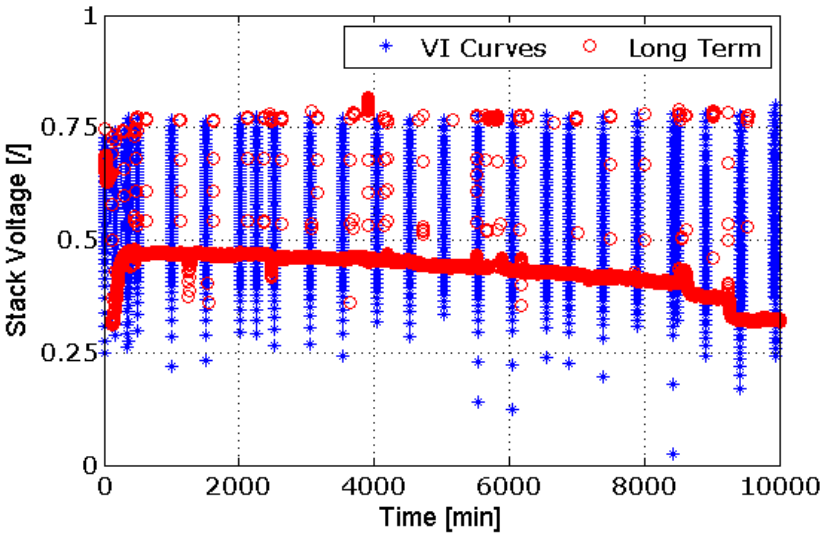

Fig. 4.7 - VI curves and long term Voltage data (Training_set).

	VI data	Long Term data	Technology
Training set	YES	YES	1
Test_set_1	YES		1
Test_set_2	YES		2
Test_set_3		YES	1
Test_set_4		YES	1

Tab. 4.2 - Features of the experimental data-sets used for neural network training and validation.

4.2.4. Results

The neural network voltage simulator showed excellent accuracy for different VI profiles, as it is shown in the comparison between simulated and experimental (i.e. measured) data of Fig. 4.8 and Fig. 4.9, where the generalization capabilities of the trained network were verified on Test_set_1 (see Tab. 4.2). The data set considered in Fig. 4.8 and Fig. 4.9 belongs to an SOFC stack of the same technology (i.e. Technology 1) as the one used for the training. In Fig. 4.9 and Fig. 4.10, it is possible to note how the neural network, thanks to the inclusion of time among the input variables, well simulates the change in VI profile slopes, due to the "natural" degradation of the stack. Such a relevant feature of the developed neural network should be also attributed to the correct choice of the training set, which allowed a good coverage of the domain of model inputs, and the correct balance between the VI curves and long term data shares in the training set.

The following validation task consisted of further comparative analyses, conducted on VI curves measured for a stack of a different technology from that used for training (i.e. Test_set_2 in Tab. 4.2). Even in this case the network showed excellent results, as it can be seen in Fig. 4.11 and Fig. 4.12. This result actually indicates a good network ability when extrapolating with respect to the training domain.

Also the accuracy attained by the neural network on long-term data was relevant, as shown in Fig. 4.13 and Fig. 4.14, which illustrate the comparison of experimental and simulated data on Test_set_3 and Test_set_4 (see Tab. 4.2), respectively. The network was able to simulate the entire trajectory of performance degradation, which as usual for fuel cells is expressed in terms of gradual reduction of stack voltage in time, while keeping the load constant. In Fig. 4.13, it is worth noting that the network, at the end of the experimental trajectory, was only capable of simulating an average voltage reduction trend; such a behavior can be explained considering that the developed network is intrinsically a static nonlinear model, thus not being able to precisely reproduce some dynamic manoeuvres. Nevertheless, the inclusion of time among the input variables still ensures obtaining good prediction of expected stack degradation in the next operating hours.

The results shown and discussed above are certainly a fair trade-off between the two different types of data, VI profiles and long term data

trajectories. It is important remarking here that the network could be trained with a more pronounced tendency towards one or the other type of data, depending on what is the targeted predictive information that has to be guaranteed in SOFC monitoring.

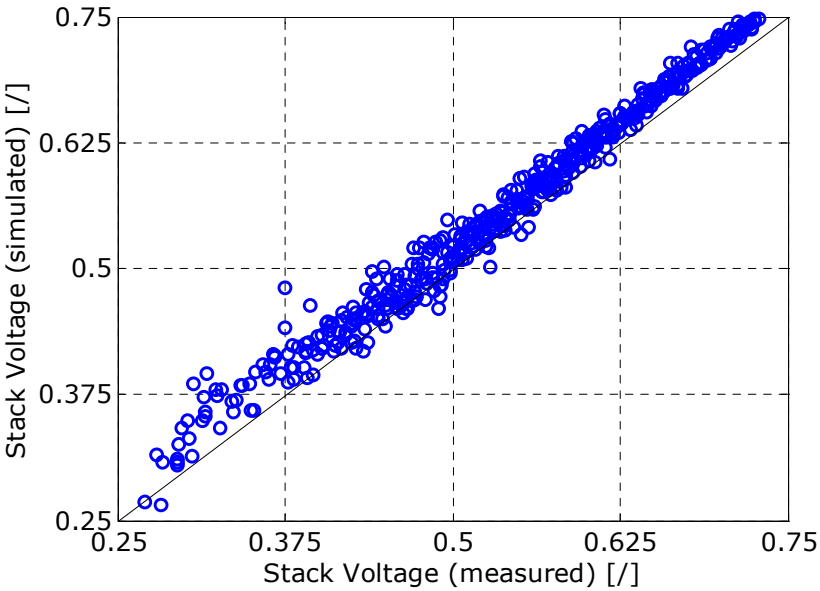

Fig. 4.8 - Comparison between measured and simulated stack voltage on Test_set_1 (VI curves).

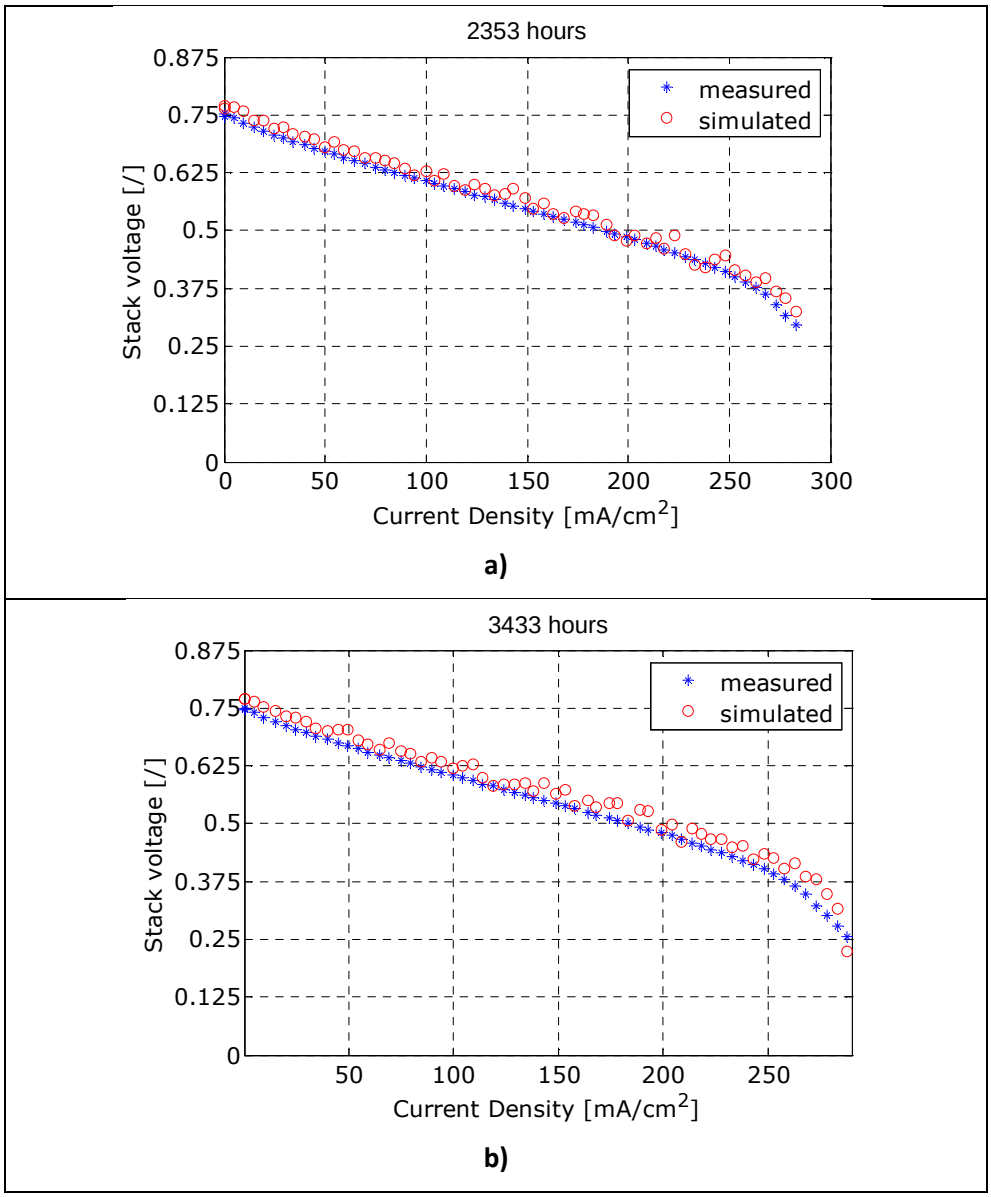

Fig. 4.9 - a) Comparison between measured and simulated stack voltage for Test_set_1 (VI curves) at 2353 hours; b) Comparison between measured and simulated stack voltage for Test_set_1 (VI curves) at 3433 hours.

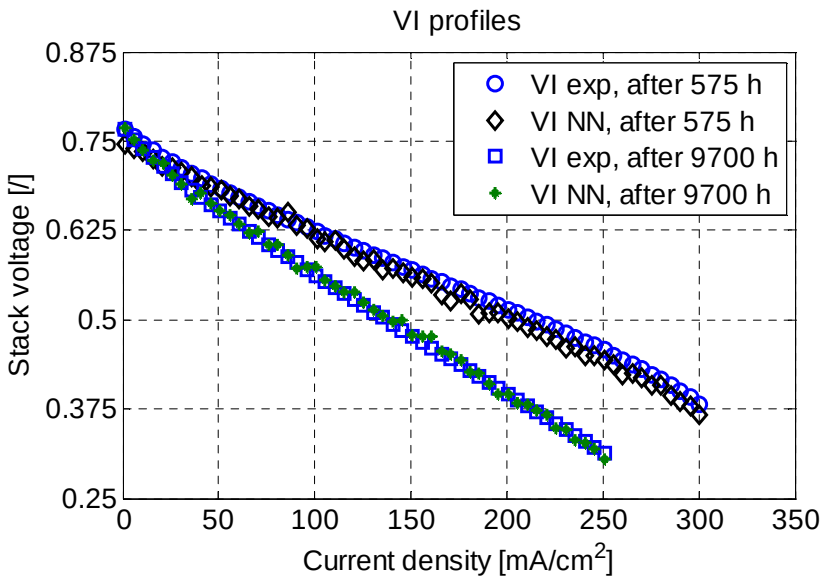

Fig. 4.10 - Comparison between measured and simulated VI profiles for the Training_set.

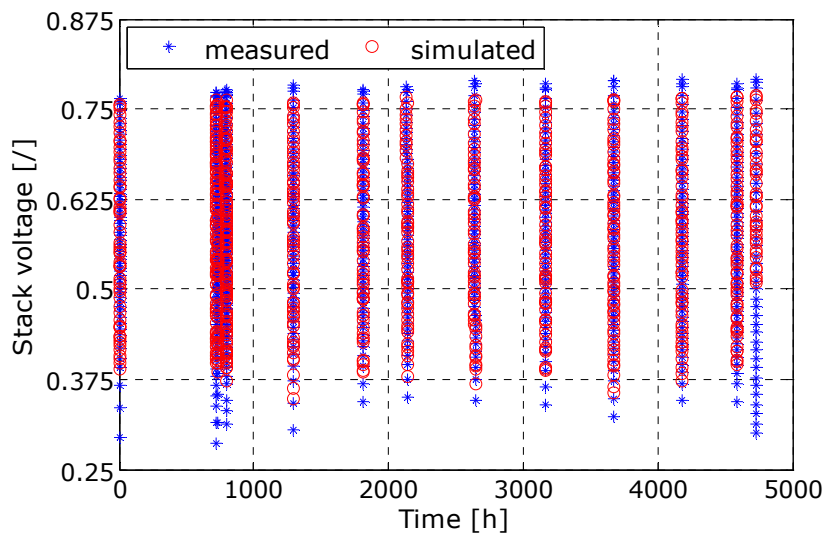

Fig. 4.11 - Comparison between measured and simulated stack voltage for Test_set_2 (VI curves).

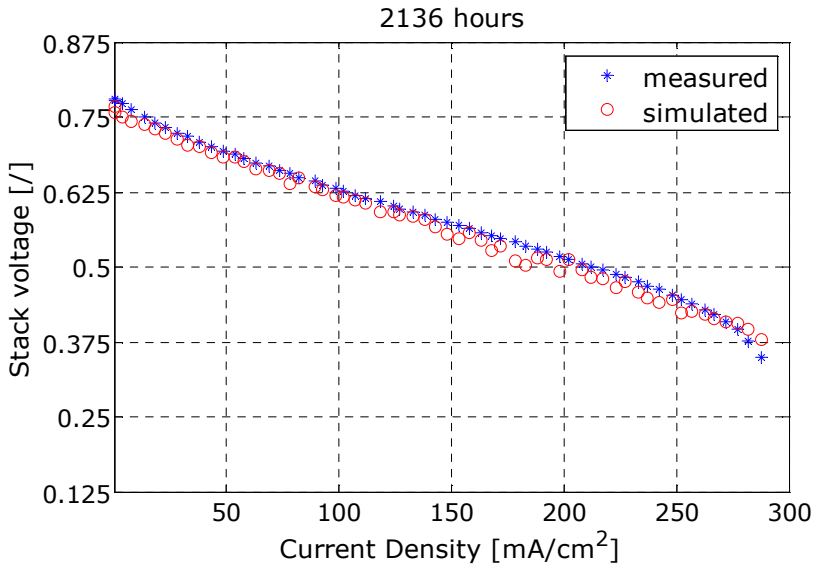

Fig. 4.12 - Comparison between measured and simulated stack voltage for Test_set_2 (VI curves) at 2136 hours.

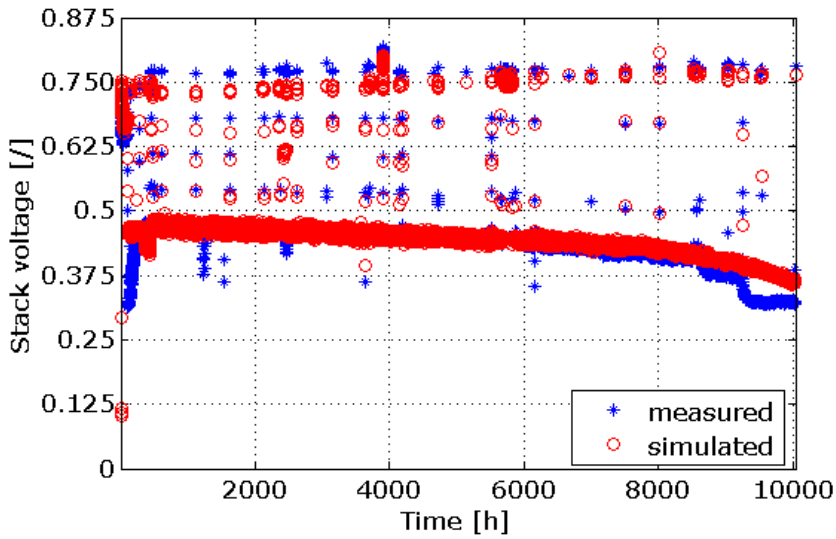

Fig. 4.13 - Comparison between measured and simulated stack voltage for Test_set_3 (long term).

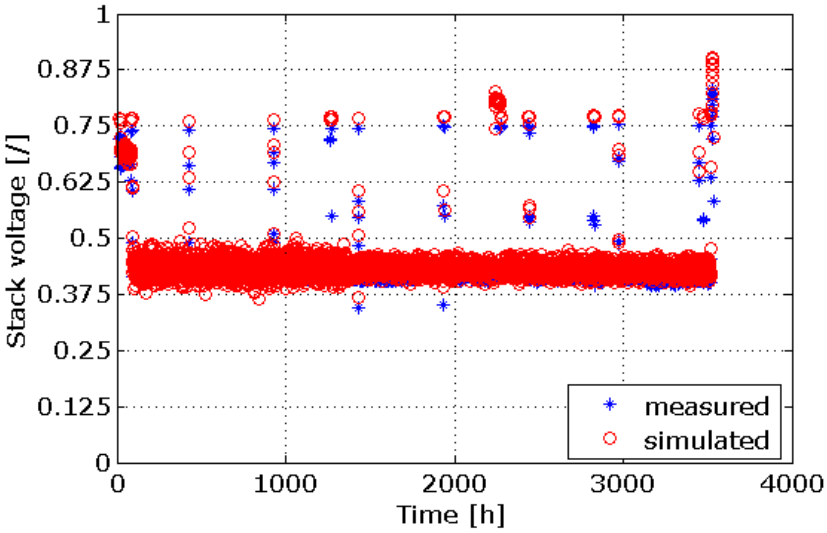

Fig. 4.14 - Comparison between measured and simulated stack voltage for Test_set_4 (long term).

4.3 Recurrent Neural Networks models of TOPSOE and VTT (HTC) SOFC stacks

In the present paragraph two black box models based on Recurrent Neural Network are presented: a RNN to simulate TOPSOE stack voltage and a RNN to simulate VTT (HTC) stack voltage. The data were provided by TOPSOE and VTT (HTC) in the frame of the EU project GENIUS. Recurrent Neural Networks were derived from static Neural Networks by considering feedback connections among the neurons, and nonlinear dynamic output error models (NOE), as discussed in the paragraph 4.1.1. This choice was motivated by the need of i) modeling the non linearity of stack voltage, ii) enhancing dynamic features to improve model accuracy during transient operation and iii) reducing the experimental burden requested for model identification (Nørgaard et al., 2000; Arsie et al., 2006). This latter feature is particularly important in case of on-board model update, which may be accomplished along a suitable single transient. The algorithms used to train and validate the Recurrent Neural Network models described in the next sections were based on the work performed by the University of Salerno over the last decade towards the development of both static and dynamic neural networks for the simulation of complex energy systems. For a more detailed description of the background on RNN the reader is addressed to the bibliography at the end of this document (Arsie et al., 2006, 2007, 2009, 2010) and to the references therein.

4.3.1. Topsoe Stack RNN

TOPSOE stack had a planar co-flow configuration and it was fueled with methane and hydrogen. The stack was tested for 21440 minutes (see Fig. 4.15). According to the 1-D model decrypted in Chapter 2, 8 input were selected to the RNN: current density; stack temperature, air cathode inlet temperature, air inlet flow rate, methane inlet flow rate, hydrogen inlet flow rate, nitrogen flow rate and water inlet flow rate. In Fig. 4.17 the transients relative to the 8 inputs selected are shown. It is important noting that in real system the stack temperature should be difficult to be measured. The anode inlet temperature should represent an alternative to

the stack temperature as input to the RNN, due to its major simplicity to be measured in the real system. Unfortunately, the experimental data provided had an error in the anode inlet temperature. Thus the stack temperature was selected instead of anode inlet temperature.

For the RNN structure the number of hidden layer was fixed to one. In order to prevent the RNN training from the above-discussed overfitting issue, in the current work the optimal trade-off between network accuracy and dimension was accomplished through a parametric analysis by varying the number of hidden neurons from 5 to 12. The input lag spaces dimensions were selected considering the different characteristic dynamic time of the different inputs of the RNN. The principle was based on the concept that a slower dynamic correspond to a greater lag space and vice-versa. In the TOPSOE stack RNN for the temperatures the lag spaces were set to 3 (slow dynamic); on the other hand for current density, voltage and flows, the lag spaces were set to 2 (fast dynamic). According to the RNN structure shown in Fig. 4.18 the internal structure is composed by 20 neurons of the input layer, 8 neurons in the hidden layer, and 1 neuron in the output layer. There are 177 parameters in the neural network (168 weights and 9 biases).

The TOPSOE data (the data set 1 with reference to Tab. 3.1) used to identify the RNN model were splitted into two data set, as showed in Fig. 4.16. The training set was selected in such a way to grant an acceptable coverage of the voltage-current domain and of main dynamic operations. This was fundamental to avoid extrapolation of the RNN The training set size represents the 64% of the entire data set and the test set the remaining 36%.

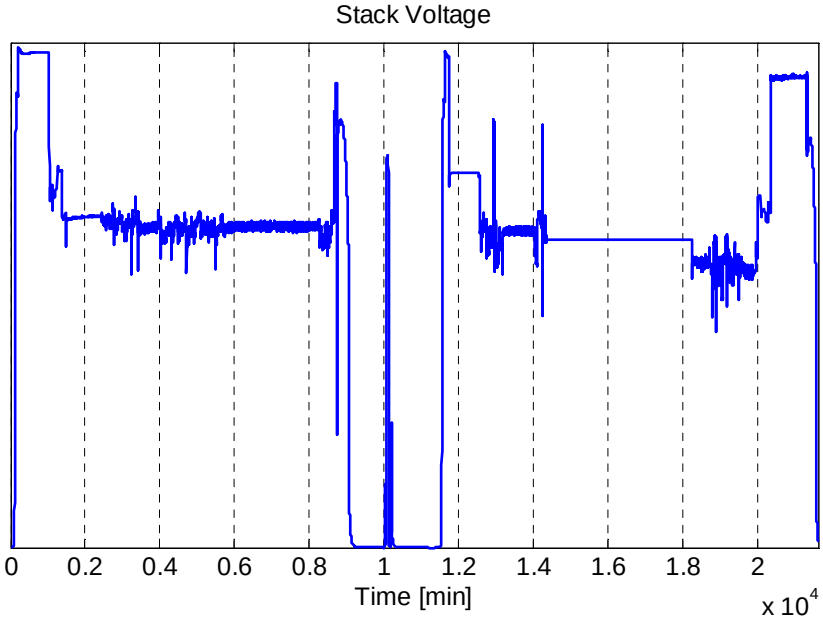

Fig. 4.15 - Topsoe stack voltage (experimental output).

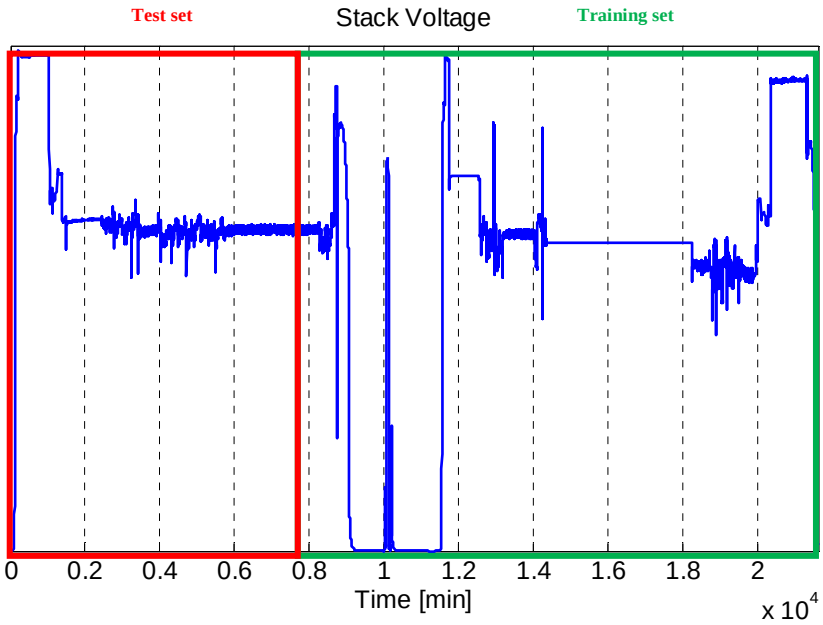

Fig. 4.16 - Topsoe stack voltage splitting into training and test set.

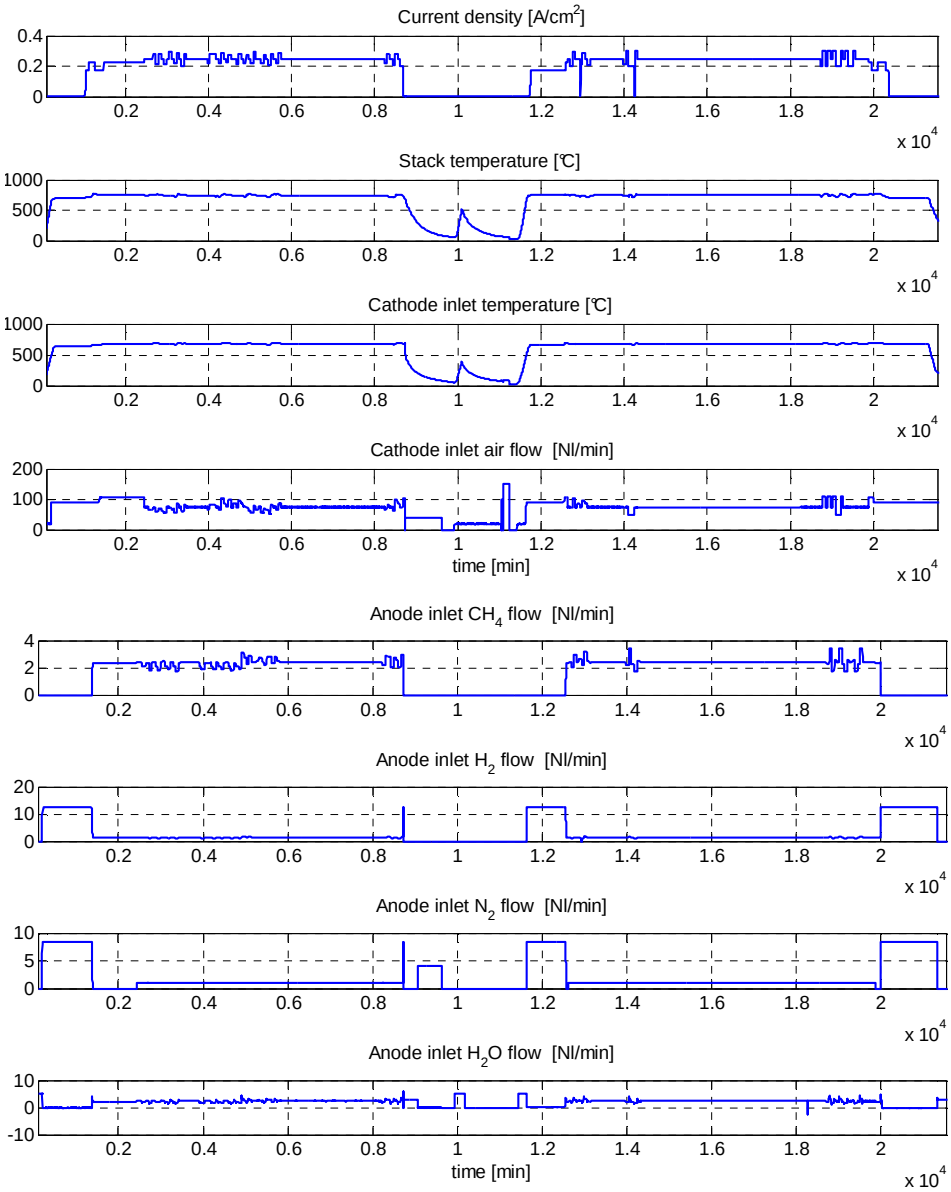

Fig. 4.17 - Topsoe RNN inputs.

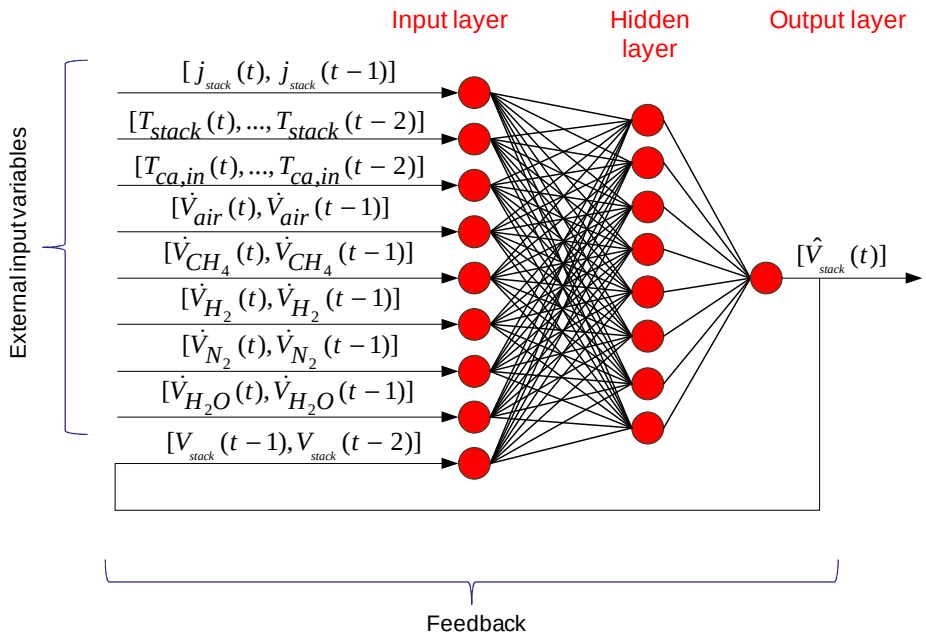

Fig. 4.18 - Schematic of Topsoe RNN architecture.

4.3.2. VTT (HTc) Stack RNN

The data used to identify the RNN model were acquired by VTT on a stack provided by HTc. The data set used to identify and validate the model corresponds to the 2nd test round provided by VTT (HTc) in the framework of GENIUS project. The stack presented a counter-flow planar configuration and it was fueled with methane and hydrogen. According to the 1-D model described and the RNN developed for TOPSOE stack before, 8 input were selected to the RNN: current density; fuel anode inlet temperature, air cathode inlet temperature, air inlet flow rate, methane inlet flow rate, hydrogen inlet flow rate, nitrogen flow rate and water inlet flow rate (see Fig. 4.22). It is important noting that the anode inlet temperature was selected instead of stack temperature.

The VTT (HTc) RNN architecture was the same as the one adopted on TOPSOE stack, the only difference is the anode inlet temperature instead of stack temperature, as shown in Fig. 4.19

The VTT (HTc) experimental transient (25000 minutes), shown in Fig. 4.20, was divided into 2 groups: one for the training set and one for the test set (see Fig. 4.21). The training set size represents the 60% of the entire data set and the test set the remaining 40%. The training set has been chosen in order to cover as much as possible the voltage-current domain and the main dynamic operations.

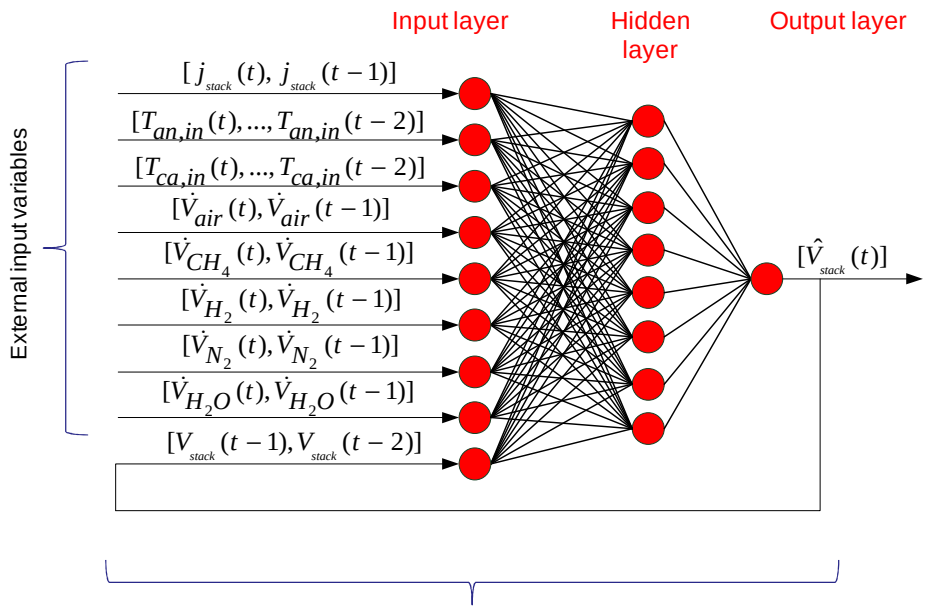

Fig. 4.19 - Schematic of VTT (HTc) RNN architecture.

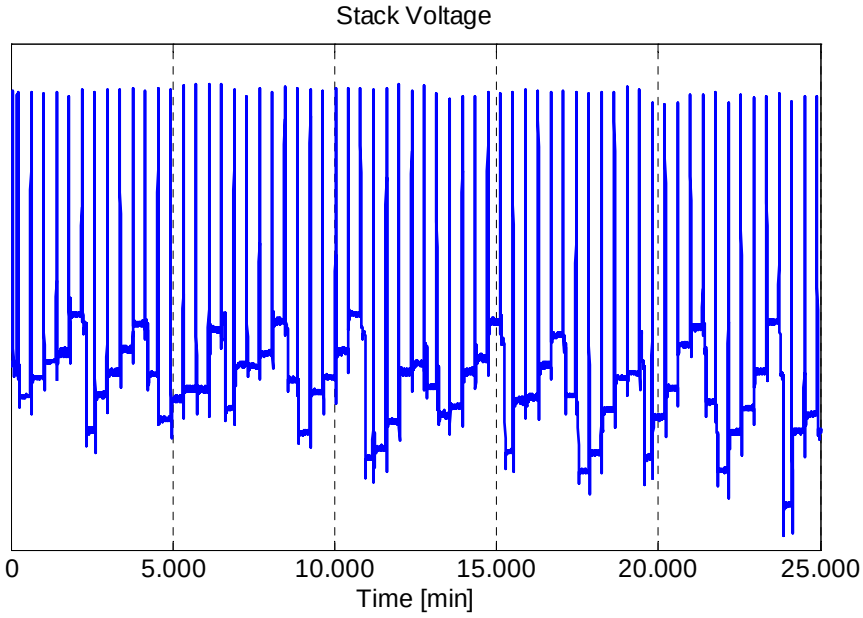

Fig. 4.20 - VTT (HTc) stack voltage (experimental output).

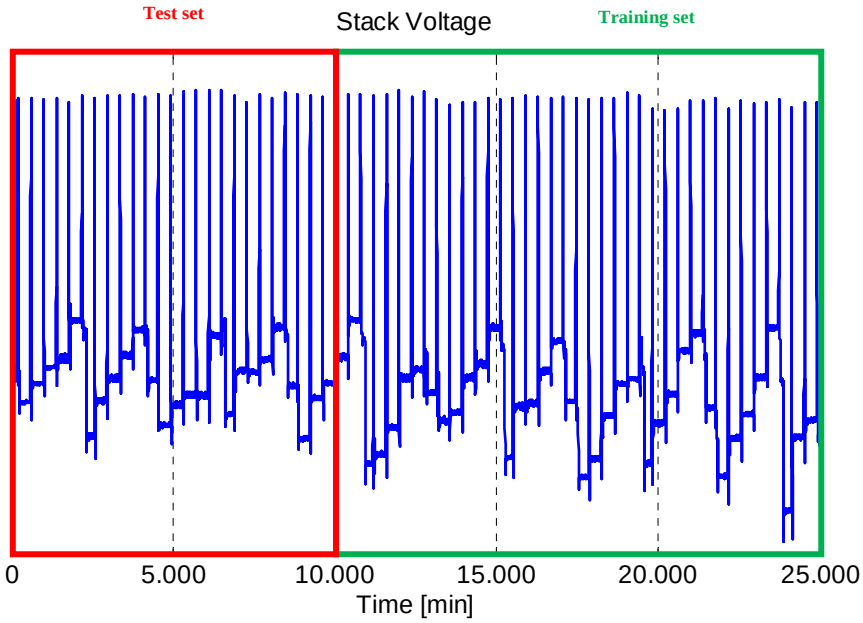

Fig. 4.21 – VTT (HTc) stack voltage splitting into training and test set.

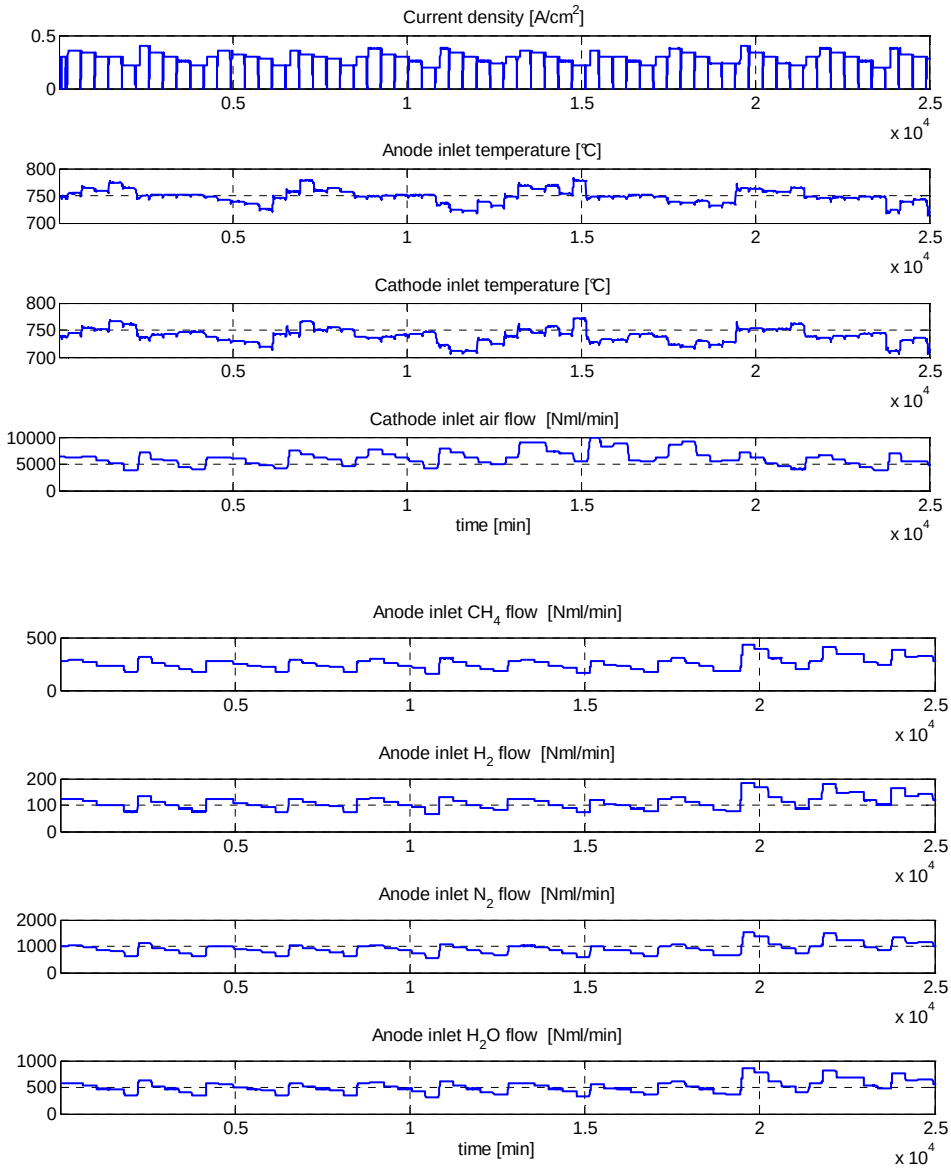

Fig. 4.22 - VTT (HTc) RNN inputs.

4.3.3. Results

The results for the training (time window 7800-24000 min) of the TOPSOE RNN are plotted in Fig. 4.23 and compared with experimental data. The test set, plotted in Fig. 4.24, indicates the good RNN accuracy in simulating SOFC transients, thus confirming RNN reliability for the TOPSOE stack experimented during the data set 1 (the 2nd test round in GENIUS project). The RNN showed optimal capability to simulate stack voltage during the transients (see Fig. 4.25). This confirms the correct choice of the training set inside the data set 1 (the 2nd test round in GENIUS project).

The results of the training set (time window 10000-25000 min) of VTT (HTc) RNN are plotted in Fig. 4.26 and compared with experimental data. The results of the test set (belonging to the 2nd test round in GENIUS project), plotted in Fig. 4.27, are very satisfactory. Some minor offsets occur in the test set, but their impact is always bounded within a safe range of +/- 2%.

Fig. 4.28 shows the comparison between TOPSOE and VTT (HTc) load domain, which highlights the larger domain covered by the latter set of experimental data set. Due to the intrinsic features of neural network models, whose extrapolation capability are limited and dependent by the training set selection, the VTT (HTc) RNN was expected to have higher generalization capabilities, thus ensuring higher performance during real-time monitoring. It is worth to note that for the development of dynamic neural network the training set has to be designed in such a way to cover all the possible maneuvers and operating conditions in a transient only. The training set design represent a critical phase in the RNN development.

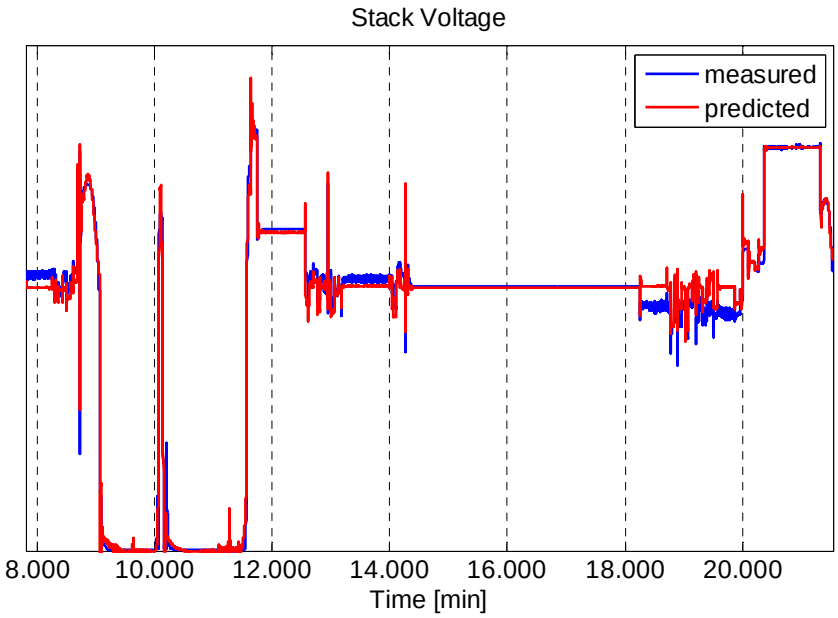

Fig. 4.23 - Comparison between measured and simulated TOPSOE stack voltage (training set).

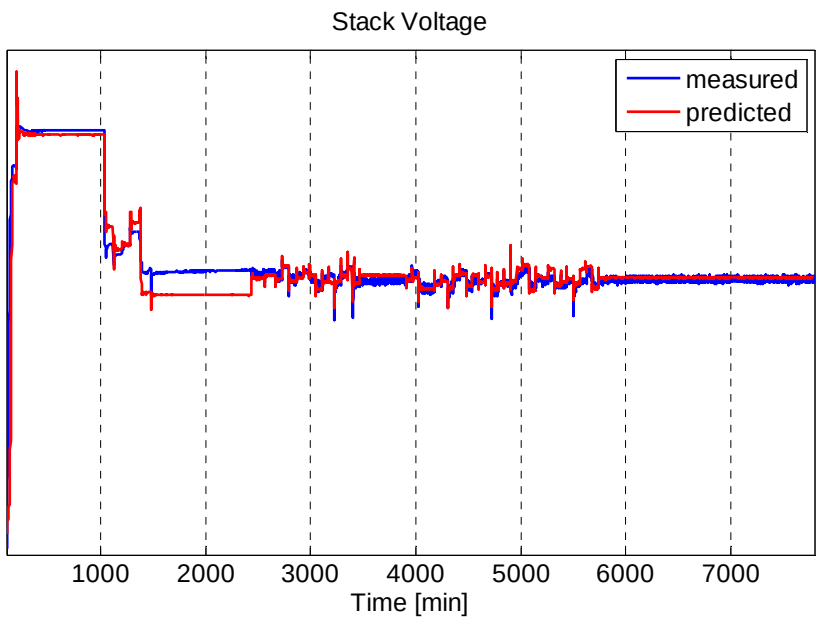

Fig. 4.24 - Comparison between measured and simulated TOPSOE stack voltage (test set).

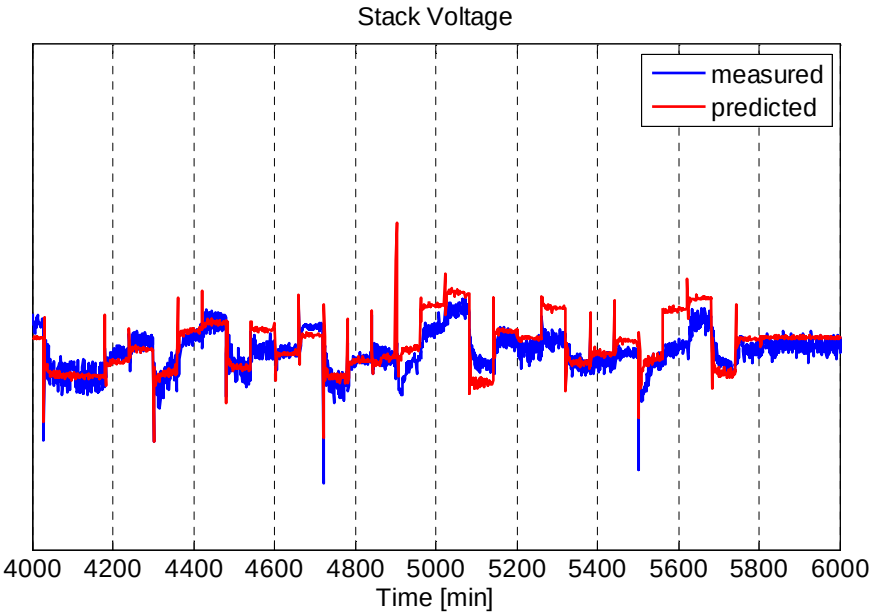

Fig. 4.25 - Comparison between measured and simulated TOPSOE stack voltage (test set), time window [4000-6000] min.

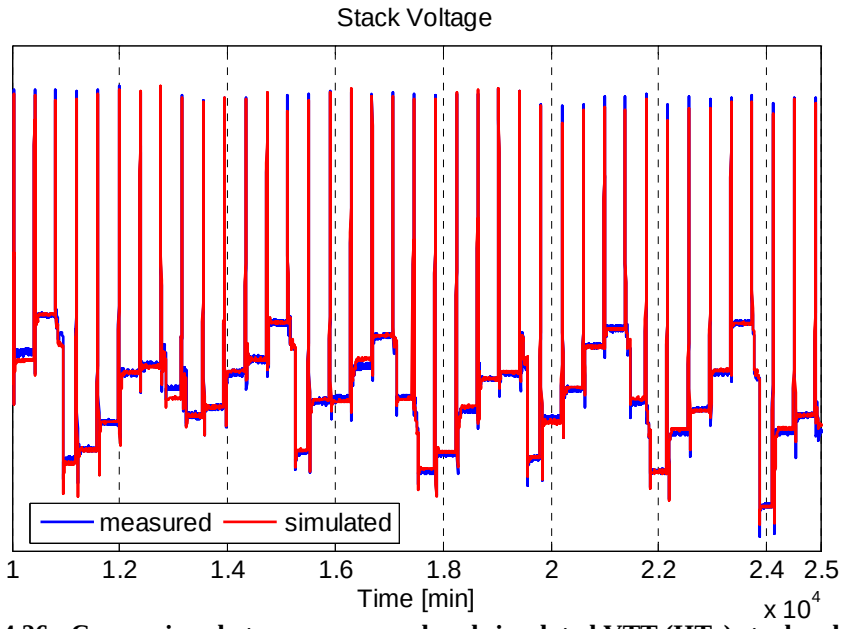

Fig. 4.26 - Comparison between measured and simulated VTT (HTc) stack voltage (training set).

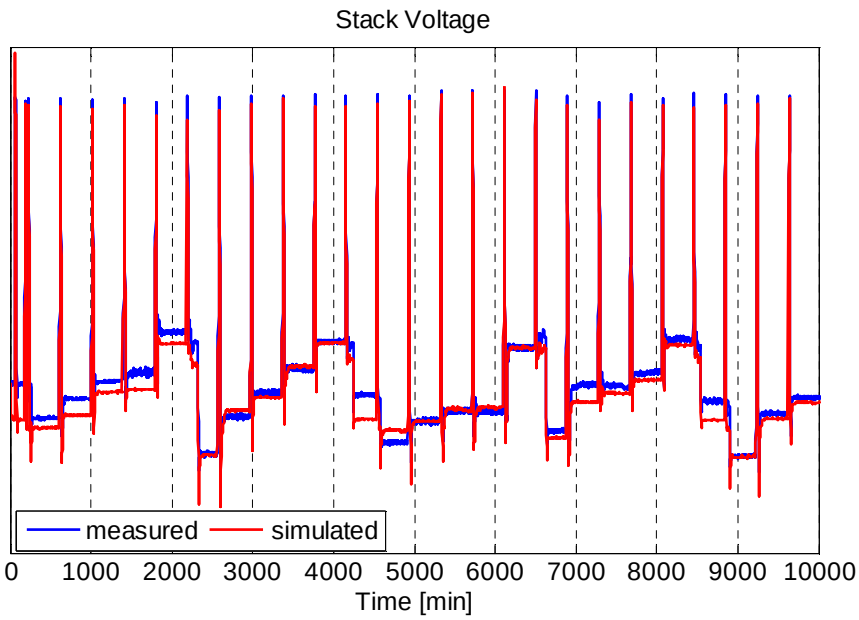

Fig. 4.27 - Comparison between measured and simulated VTT (HTc) stack voltage (test set).

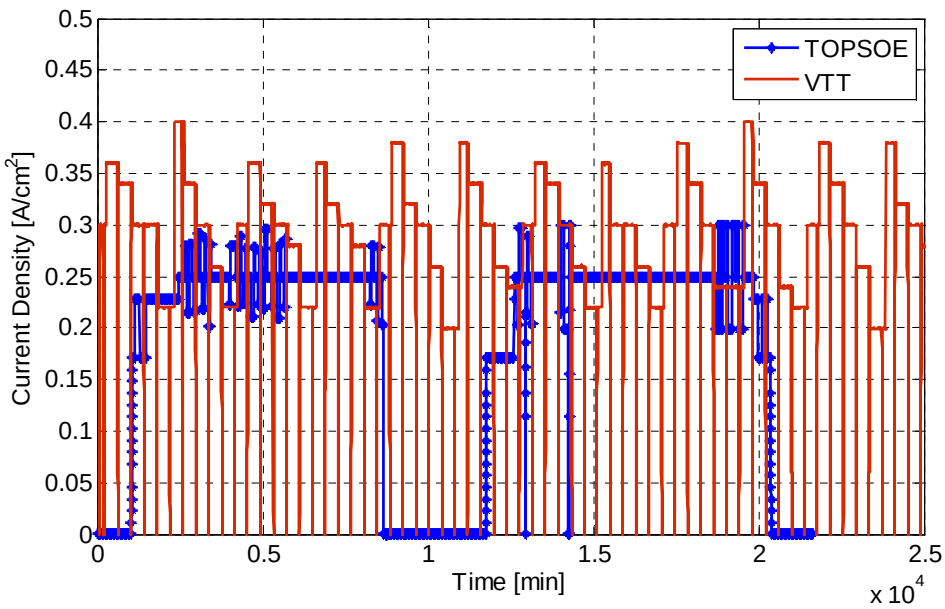

Fig. 4.28 - Comparison between TOPSOE and VTT (HTc) load time history investigated in the 2nd test round

CHAPTER 5 Conclusions

In the present work different SOFC stack models have been presented. The results shown were obtained in the general framework of the GENIUS project (GEneric diagNosis Instrument for SOFC systems), funded by the European Union (grant agreement n° 245128). The objective of the project is to develop "generic" diagnostic tools and methodologies for SOFC systems. The "generic" term refers to the flexibility of diagnosis tools to be adapted to different SOFC systems.

In order to achieve the target of the project and to develop stack models suitable for monitoring, control and diagnosis applications for SOFC systems, different modeling approaches have been proposed. Particular attention was given to their implementability into computational tools for on-board use. In this thesis one-dimensional (1-D), grey-box and black-box stack models, both stationary and dynamic were developed. The models were validated with experimental data provided by European partners in the frame of the GENIUS project.

A 1-D stationary model of a planar SOFC in co-flow and counter-flow configurations was presented. The model was developed starting from a 1-D model proposed by the University of Salerno for co-flow configuration (Sorrentino, 2006). The model was cross-validated with similar models developed by the University of Genoa and by the institute VTT. The cross-validation results underlined the suitability of the 1-D model developed. A possible application of the 1-D model for the estimation of stack degradation was presented. The results confirmed the possibility to implement such a model for fault detection.

A lumped gray-box model for the simulation of TOPSOE stack thermal dynamics was developed for the SOFC stack of TOPSOE, whose experimental data were made available in the frame of the GENIUS project. Particular attention was given to the problem of heat flows between stack and surrounding and a dedicated model was proposed. The black-box approach followed for the implementation of the heat flows and its reliability and accuracy was shown to be satisfactory for the purpose of its applications. The procedure adopted turned out to be fast and applicable to other SOFC stacks with different geometries and materials. The good results obtained and the limited calculation time

make this model suitable for implementation in diagnostic tools. Another field of application is that of virtual sensors for stack temperature control.
Black-box models for SOFC stack were also developed. In particular, a stationary Neural Network for the simulation of the HEXIS stack voltage was developed. The analyzed system was a 5-cells stack operated up to 10 thousand hours at constant load. The training set was chosen appropriately, to balance the information derived from the VI curves and from the long term data acquisition. Indeed, the first sets (i.e. VI profiles) bring the knowledge on SOFC stack performance, while the second ones (i.e. long term data) provide information on the degradation affecting the electrochemical processes occurring into the stack. The neural network exhibited very good prediction accuracy, even for systems with different technology from the one used for training the model. Beyond showing excellent prediction capabilities, the NN ensured high accuracy in well reproducing evolution of degradation in SOFC stacks, especially thanks to the inclusion of time among model inputs. Moreover, a Recurrent Neural Network for dynamic simulation of TOPSOE stack voltage and a similar one for a short stack built by HTc and tested by VTT were developed. The stacks analyzed were: a planar co-flow SOFC stack (TOPSOE) and a planar counter-flow SOFC stack (VTT-HTc). The two RNNs had the same structures with 177 parameters identified. The training sets were selected to cover all the possible operating conditions and all the possible dynamic maneuvers.
All models developed in this thesis show high accuracy and computation times that allow them to be implemented into diagnostic and control tool both for off-line (1-D model and grey-box) and for on-line (NN and RNNs) applications. It is important noting that the models were developed with reference to stacks produced by different companies. This allowed the evaluation of different SOFC technologies, thus obtaining useful information in the models development. The information underlined the critical aspects of these systems with regard to the measurements and control of some system variables, giving indications for the stack models development.
The proposed modeling approaches are good candidates to address emerging needs in fuel cell development and on-field deployment, such as the opportunity of developing versatile model-based tools capable to be generic enough for real-time control and diagnosis of different fuel cell systems typologies, technologies and power scales.

CHAPTER 6 APPENDIX

Fault diagnosis

The final aim of a fault diagnosis activity is to reach the required criteria for a commercial application, which, besides high lifetime and performance, include high reliability and safety and suitable costs as well.
The desire to guarantee system availability and reliability is the reason why Fault Diagnosis methodologies are applied to several different fields, ranging from passenger cars and trucks to aircrafts, trains and even to stationary systems, such as power and chemical plants (Isermann, 2004; Rizzoni et al. 2008).
To guarantee the safe operation of fuel cell systems and to support the successful deployment of SOFC, it is necessary to make systematic use of specific computational tools for developing suitable control and diagnostic strategies.
With particular regard to diagnostics, designers and users always pay interest in preventing the occurrence of failures of any mechanism, machine or energy conversion system. To this end, several approaches can be taken, the most obvious of which is to stop the system whenever an abnormal functioning is observed, i.e., a fault is determined as a difference in the performance of the system from its expected behavior. The ability to detect the occurrence of any fault, and identify its cause, is a critical task.
Fault diagnosis methods aim to satisfy the following requirements: a) monitoring incipient faulty conditions to avoid abrupt failure, as well as severe damages; b) diagnosing faults in the actuators, process components or sensors; c) detecting faults in closed loops and supervising processes in transient states. The fault diagnosis process involves three activities: i) fault detection to indicate the presence of faults and the time of detection; ii) fault isolation to determine the location of the faults after their detection; iii) fault identification to determine the size of the faults and their time-variant behavior. The present work mainly focuses on steps i)

and ii).

The fault detection process is composed of two main phases: residual generation and residual analysis (see Fig. 6.1). The residual provided by the first process consists of the difference between the known (measured or nominal) and the "faulty" value of the same variable. The purpose of the second phase, residual analysis, is to evaluate the residual and draw conclusions regarding the presence of a fault. This is done by comparing the residual with a threshold value. If the residual exceeds the threshold, an analytical symptom is generated and a fault is detected; otherwise, the system is working properly, and no symptoms are obtained (Arsie et al, 2010 (a)).

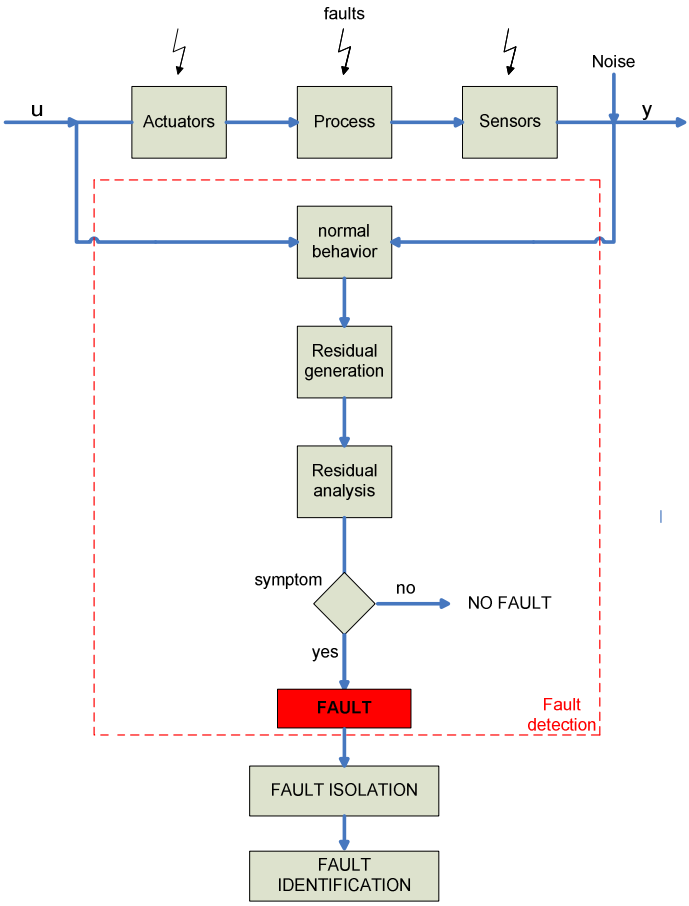

Fig. 6.1 – Fault Diagnosis scheme.

The most common residual generation methods are divided into three categories: signal-based, analytical model-based, knowledge based.
Signal based techniques rely on comparative assessment of the status of a system under testing with other known occurrences and consider a directly measurable variable. By assuming special mathematical models for the measured signal, suitable features are calculated such as amplitudes, phases, spectrum frequencies and correlation functions for a certain frequency band width of the signal.
Model-based techniques more commonly involve the description of a system through mathematical models of the physical laws governing its behavior (Isermann, 2004; Isermann, 2006; Rizzoni et al. 2008, Witczak, 2003). The model-based fault diagnosis is based on comparing on-line the real behavior of the system with the results obtained by a mathematical model. The most common model-based methods are parameter estimation, state observers and parity equations (Isermann, 2006).
In the case of modeling uncertainty, or the presence of vague or incomplete knowledge about the system, an alternative is required, which is not based upon the existence of an exact mathematical model of the system. In this framework, Fault Diagnosis can be considered within a knowledge-based approach, in order to combine heuristic knowledge with any model knowledge which may be available (Rizzoni et al., 2008; Isermann, 2006).
The final result of the detection process is therefore a set of analytical symptoms, or fault signatures, which are contained in a matrix, i.e. the fault signature matrix (FSM), with the symptoms in the columns and the faults in the rows. Fault isolation and identification procedures consider as inputs all the available symptoms. To perform these tasks, if no information is available on the fault-symptom causalities, experimentally trained classification methods can be applied (classification methods). If the fault symptom causalities can be expressed in the form of if-then rules, reasoning or inference methods are applicable (Arsie et al., 2010 (a)).

6.1 Fault Tree Analysis

The Fault Tree Analysis (FTA) is a deductive methodology aimed at determining logical occurrence of undesired events, which could result in either system or component faults. The process starts from the fault to be analyzed (i.e., top event) and, through a top/down approach, all the possible combinations of causes (i.e., events) are considered. The links between different events are expressed by Boolean relations. The analysis proceeds until no developable events (i.e., basic events) are individuated, to which are associated specific symptoms. The logical relationships between the events are graphically represented by a tree, which has at the top the fault to analyze and at the bottom the symptoms. Tab. 6.1 shows the terminology adopted in the fault tree development.

Fig. 6.2 shows a fault tree example, in which the fault (top event) can be caused either by event 1 or event 2. The event 1 is caused by the contemporary occurrence of the basic events 1 and 2 (i.e. symptoms). On the other hand, the event 2 is correlated to just one symptom (i.e. basic event 3).

In the development of a diagnostic tool the fault tree analysis is particularly important to understand both causes and symptoms of specific faults, through a physical knowledge of the system/component. Once the symptoms are identified, and in case these are associated to either measured or estimated system variables, it is possible to define a set of parameters to be monitored in the FDI process.

The complexity of an SOFC system suggests to analyze the faults at the component level. The following sub-sections reports the faults that are most likely to occur. In this work the faults at both BoP (i.e. air blower, air pre-heater, pre-reformer, post-burner, pipe between air compressor and air pre-heater) and stack levels are taken into account (Arsie et al., 2010 (a)).

	basic event / symptom	A basic initiating fault requiring no further development or the corresponding symptom
	conditioning event	Specific conditions or restrictions that apply to any logic gate
	undeveloped event	An event which is no further developed either because it is of insufficient consequence or because information is unavailable
	top/intermediate event	A fault event that occurs because of one or more antecedent causes acting through logic gates
	transfer	Indicates that the tree is developed at the occurrence in other pages. it is used to avoid extensive duplication in a fault tree
	and	Output fault occurs if all of the input faults occur
	or	Output fault occurs if at least one of the input faults occurs

Tab. 6.1 - Fault Tree symbols and related descriptions.

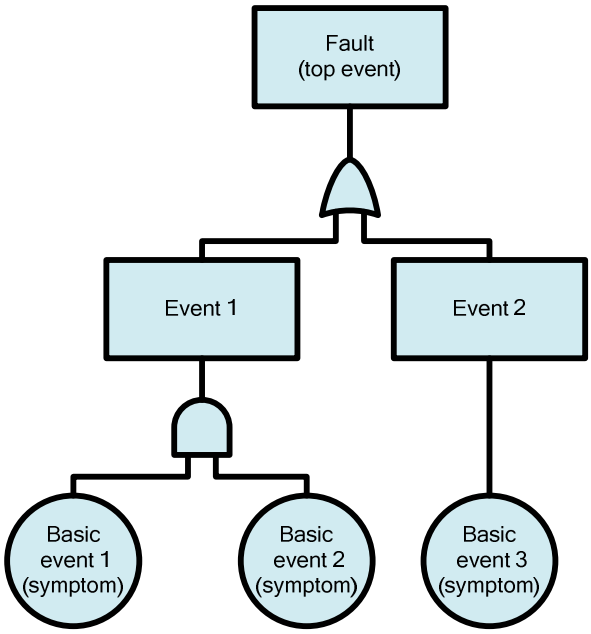

Fig. 6.2 - Fault Tree example developed through a top-down approach (refer to Tab. 6.1 for the list of symbols).

6.2 Fault Detection and Isolation process

The Fault Detection and Isolation process (FDI) is illustrated in Fig. 6.4. According to this scheme after the identification of the system faults, a fault tree analysis for each system component is developed. In the FTA of a component is taken into account also the interactions of other components, which are directly linked to it. From this analysis a set of system variables is identified. The definition of the final set of variables to be monitored requires a trade-off between the robustness of the method guaranteed by the physical analysis of components (FTA) and their interactions at system level, and the costs evaluation for on-field application of the SOFC system. Once the final set of system variables is defined, it is possible to generate the *fault signature matrix* (FSM) (Isermann, 2006). This matrix has on the rows the system faults f_i and on

the columns (or vice versa) the symptoms s_i associated to the defined set of variables. According to the FTA at component level and the knowledge of components interactions at system level, in the FSM at each fault is associated a vector of symptoms, which is 1 if the symptom is associated to that fault and 0 otherwise. Every symptoms vector must be different from each other, thus it is possible to isolate univocally a fault. The FSM is the final result of the FDI process, which allows the fault isolation at system level. In the on-line diagnosis the presence of symptoms indicates the occurrence of a fault in the system (*fault detection*). A possible candidate method for SOFC system application could be a parity equation approach. According to this approach the defined set of system variables is observed in the real system and compared with their equivalent ones of a system model, which simulates the system in nominal (non faulty) condition. The difference of signals between the system and the model are expressed by residuals r_i (Rizzoni et al., 2008; Isermann, 2006; Witczak, 2003). If a residual exceeds its relative threshold a symptom is generated (s_i=1 if r_i > threshold, s_i=0 otherwise). During on-line SOFC operation if a symptom is different from 0 a fault is detected. To isolate it, the vector of the symptoms associated to the set of variables is compared with all vectors in the FSM, thus it is possible isolate the fault in the system.

	Symptom s_1	**Symptom s_2**	**Symptom s_3**	**Symptom s_4**
Fault f_1	0	1	1	0
Fault f_2	0	1	1	0
Fault f_3	1	0	1	1

Fig. 6.3 – Fault Signature Matrix.

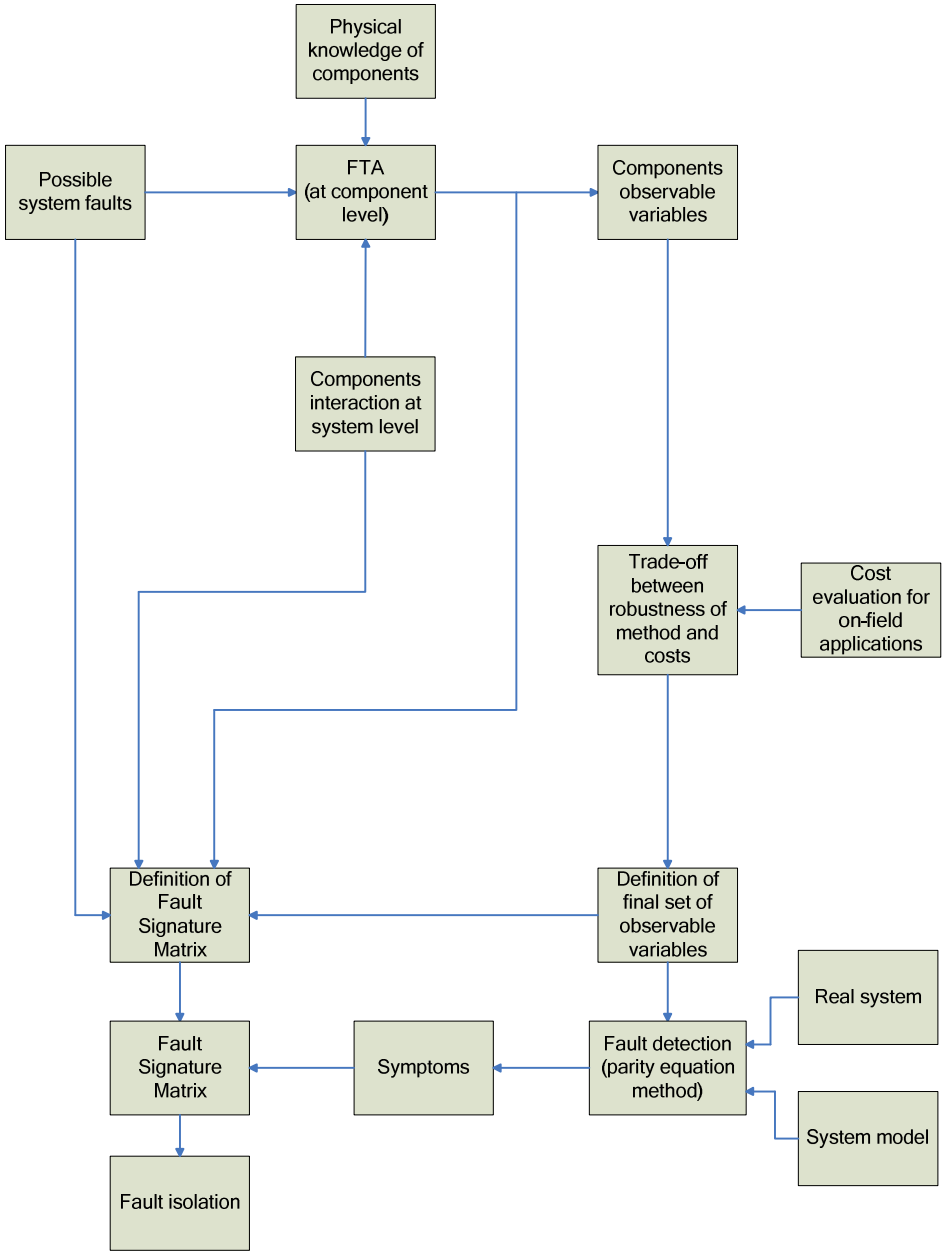

Fig. 6.4 – Fault Detection and Isolation process scheme.

References

Achenbach E., (1995), *Response of a solid oxide fuel cell to load change*, Journal of Power Sources, Vol. 57 (1995), pp. 105-109.

Achenbach E., and Riensche E., (1994), *Methane/steam reforming kinetics for solid oxide fuel cells*, Journal of Power Sources, Vol. 52 (1994), pp. 283-288.

Aguiar P., Adjiman C.S., Brandon N.P., (2004), *Anode-supported intermediate temperature direct internal reforming solid oxide fuel cell. I: model-based steady-state performance*, Journal of Power Sources, Vol. 138 (2004), pp. 120-136.

Arriagada J., Olausson P., Selimovic A., (2002), *Artificial neural network simulator for SOFC performance prediction*, Journal of Power Sources Vol. 112 (2002), pp. 54-60.

Arsie I., Di Filippi A., Marra D., Pianese C., Sorrentino M., 2010 (a), *Fault Tree Analysis Aimed to Design and Implement On-Field Fault Detection and Isolation Schemes for SOFC Systems*, ASME 8th International Conference on Fuel Cell Science, Engineering and Technology, Vol. 1 (2010), pp. 389-399.

Arsie I., Marotta F., Pianese C., Rizzo G. (2001), *Information Based Selection of Neural Network Training Data for S.I. Engine Mapping*,

SAE Transactions, Journal of Engines, Vol. 110 (2001), pp. 549-560.

Arsie I., Marra D., Pianese C., Sorrentino M., 2010 (b), *Real-Time Estimation of Engine NO_x Emissions via Recurrent Neural Networks*, the 6th IFAC Symposium Advances in Automotive Control, 12/07-14/07 2010, Monaco, Germania.

Arsie I., Pianese C., Sorrentino M. (2006), *A procedure to enhance identification of recurrent neural networks for simulating air–fuel ratio dynamics in SI engines*, Engineering Applications of Artificial Intelligence, Vol. 19 (2006), pp. 65–77.

Bhattacharyya D, Rengaswamy R., (2009), *A review of solid oxide fuel cell SOFC) dynamic models*, Industrial & Engineering Chemistry Research, Vol. 48 (2009); pp. 6068-6086.

Bogicevic A., Wolverton C., Crosbie G.M., Stechel E.B., (2001), *Defect ordering in aliovalently doped cubic zirconia from first principles*, Physical Review B, Vol. 64 (2001), 014106.

Bove R., Lunghi P., Sammes M.N., (2005), *SOFC mathematic model for systems simulations. Part one: from a micro-detailed to macro-black-box model*, International Journal of Hydrogen Energy, Vol. 30 (2005), pp. 181-187.

Bove R, Ubertini S., (2006), *Modeling solid oxide fuel cell operation: approaches, techniques and results*, Journal of Power Sources,

Vol.159 (2006), pp. 543-559.

Bove R, Ubertini S., (2008), *Modeling solid oxide fuel cells: methods, procedures and techniques*, Fuel Cells and Hydrogen Energy, Springer, 2008.

Braun R. (2002), *Optimal Design and Operation of Solid Oxide Fuel Cell Systems for Small-Scale Stationary Applications*, Ph.D. Thesis, University of Wisconsin, Madison, USA.

Burt A. C., Celik, I. B., Gemmenb, R. S., Smirnov A. V., (2004), *A numerical study of cell-to-cell variations in a SOFC stack*, Journal of Power Sources, Vol.126 (2004), pp. 76–87.

Campanari S., (2001), *Thermodynamic model and parametric analysis of a tubular SOFC module*, Journal of Power Sources, Vol. 92 (2001), pp. 26-34.

Chakraborty U. K. (2009), *Static and dynamic modeling of solid oxide fuel cell using genetic programming*, Energy, Vol. 34 (2009), pp. 740-751.

Cheddie D.F., Munroe N.D.H., (2007), *A dynamic 1D model of a solid oxide fuel cell for real time simulation*, Journal of Power Sources, Vol. 171 (2007), pp. 634-643.

Chick L. A., Williford R. E., Stevenson J. W., (2003), *Spreadsheet Model of SOFC Electrochemical Performance*, SECA Modeling &

Simulation Training Session August 2003 (web-page: www.netl.doe.gov/ publications/ proceedings/ 03/ seca - model/ seca-model03.html).

Chick L. A., Williford R. E., Stevenson J. W., Windisch Jr C. F., Simner S. P., (2002), *Experimentally Calibrated, Spreadsheet Based SOFC Unit Cell Performance Model*, Proceedings of Fuel Cell Seminar, PNNL-SA-37014, 19-21 November, 2002, Palm Springs, CA, USA.

Christiansen N., Hansen J.B., Kristensen S., Holm-Larsen H., Linderoth S., Hendriksen P.V., Larsen P.H., Mogensen, M., (2005), *Status and Recent Status and Recent Progress in SOFC Development at Topsoe Fuel Cell /Ris National Laboratory*, Proceedings of Fuel Cell Seminar, November, 2005, Palm Springs, CA, USA.

Costamagna P., Magistri L., Massardo A.F., (2001), *Design and part-load performance of a hybrid system based on a solid oxide fuel cell reactor and a micro gas turbine*, Journal of Power Sources, Vo. 96 (2001), pp. 352-368.

Costamagna P., Selimovic A., Del Borghi M., Agnew G., (2004) *Electrochemical model of the integrated planar solid oxide fuel cell (IP-SOFC),* Chemical Engineering Journal, Vol. 102 (2004), pp. 61-69.

Entchev E, Yang L. (2007), *Application of adaptive neuro-fuzzy inference system techniques and artificial neural networks to predict solid oxide*

fuel cell performance in residential microgeneration installation, Journal of Power Sources, Vol. 170 (2007), pp. 122-129.

Esposito A., Moçotéguy P., Postiglione F., Guida M., Pianese C., Pohjoranta A., Wang K., Hissel D., Péra M.-C., Pofahl S., (2012), *Experimental Test Plan and Data Analysis Based on the Design of Experiment Methodology*, Proceedings of the ASME 2012 6th International Conference on Energy Sustainability & 10th Fuel Cell Science, Engineering and Technology Conference, July 23-26, 2012, San Diego, CA, USA.

Ferrari M.L., Traverso A., Massardo A.F., (2004), *Transient analysis of solid oxide fuel cell hybrids: Part B e Anode recirculation model*, ASME Conference Proceedings, 2004, pp. 399-407.

Fuel Cell Handbook, 6th ed., (2002), U.S. Department of Energy/National Energy Technology Laboratory Strategic Center for Natural Gas, Morgantown, WV/Pittsburgh, PA/Tulsa, OK, 2002, November.

Gargano M. L., G. Raggad B. G. (1999), *Data mining - a powerful information creating tool*, OCLC Systems & Services, Vol. 15 (1999), pp. 81-90.

Goldberg D.E. (1989), *Genetic algorithms in search, optimization and machine learning*, Addison-Wesley Educational Publishers Inc, 1989.

Gubner A, Froning D, Haart BD, Stolten D., (2003), *Complete modeling*

of kW-range SOFC stacks, Proceedings - Electrochemical Society, ISSN Pennington, NJ, ETATS-UNIS.

Gubner A., (2005), *Non-isothermal and dynamic SOFC voltage current behavior*, Proceedings - Electrochemical Society, Pennington, NJ, ETATS-UNIS.

Gubner A., Saarinen J., Ylijoki J., Froning D., Kind A., Halinen M., Noponen M., Kiviaho J., (2006), *Dynamic co-simulation of a solid oxide fuel cell (SOFC) and the balance of plant (BoP) by combining an SOFC model with the BoP-modelling tool APROS*, 7th European Fuel Cell Forum; (EFCF 2006), Lucerne, Switzerland.

Hajimolana S.A., Soroush M., (2009), *Dynamics and control of a tubular solid-oxide fuel cell*, Industrial & Engineering Chemistry Research, Vol. 48 (2009), pp. 6112-6125.

Haykin S., (1999), *Neural Networks*, Prentice Hall.

Haynes C., (1999), *Simulation of Tubular Solid Oxide Fuel Cell Behavior for Integration Into Gas Turbine Cycles*, Ph.D. Thesis, Georgia Institute of Technology, Atlanta, GA, USA.

Hecht-Nielsen R., (1987), *Neurocomputing*, Addison-Wesley.

Huanga Q.A., Wanga B., Quc W., Huic R., (2009), *Impedance diagnosis of metal-supported SOFCs with SDC as electrolyte*, Journal Power Sources, Vol. 191 (2009), pp. 297-303.

Huo H.B., Zhu X.J., Cao GY. (2006), *Nonlinear modeling of a SOFC stack based on a least squares support vector machine*, Journal of Power Sources, Vol. 162 (2006), pp. 1220-1225.

Huo H.B., Zhu X.J., Hu W.Q., Tu H.Y., Li J., Yang J. (2008), *Nonlinear model predictive control of SOFC based on a Hammerstein model*, Journal of Power Sources, Vol. 185 (2008), pp. 338-344.

Isermann R., (2004), *Model-Based Fault Detection And Diagnosis, Status And Applications*, 16th IFAC Symp. on Automatic Control in Aerospace (ACA 2004), June 14-18, St. Petersburg, Russia.

Isermann R., (2006), *Fault Diagnosis System, An Introduction from Fault Detection to Fault Tolerance*, Springer, Verlag, Berlin Heidelberg, Germany.

Iwata M., Hikosaka T., Morita M., Iwanari, T., Ito K., Onda K., Esaki Y., Sakaki Y., Nagata S., (2000), *Performance analysis of planar-type unit SOFC considering current and temperature distributions*, Solid State Ionics, Vol. 132 (2000), pp. 297–308.

Jang J.S.R., (1993), *ANFIS: adaptive-network-based fuzzy inference system*, Systems, Man and Cybernetics, IEEE. Transactions, Vol. 23 (1993), pp. 665- 685.

Jiang W., Fang R., Khan J.A., Dougal R.A., (2006), *Parameter setting and analysis of a dynamic tubular SOFC model*. Journal of Power

Sources, Vol. 162 (2006), pp. 316-326.

Kang Y.W., Li J., Cao G.Y., Tu H.Y., Li J., Yang J., (2009), *A reduced 1D dynamic model of a planar direct internal reforming solid oxide fuel cell for system research*, Journal of Power Sources, Vol. 188 (2009), pp. 170-176.

Keegan K., Khaleel M., Chick L.A., Recknagle K., Simner S., Deibler J. (2002), *Analysis of a Planar Solid Oxide Fuel Cell Based Automotive Auxiliary Power Unit*, SAE Technical Paper Series No. 2002-01-0413.

Larminie, J., Dicks, A., (2003), *Fuel Cell Systems Explained*, John Wiley & Sons Ltd, The Atrium, Southern Gate, Chichester, West Sussex PO19 8SQ, England.

Larrain D., Van Herle J., Favrat D., (2006), *Simulation of SOFC stack and repeat elements including interconnect degradation and anode reoxidation risk*, Journal of Power Sources, Vol. 161 (2006), pp. 392-403.

Lee S.J., Siau K. (2001), *A review of data mining techniques*, Industrial Management & Data Systems, Vol. 101 (2001), pp. 41-46.

Ljung, L. (1999), *System Identification*, Theory for the User, 2nd ed.

Magistri L., Bozzo R., Costamagna P., Massardo A.F., (2004), *Simplified versus detailed solid oxide fuel cell reactor models and influence on*

the simulation of the design point performance of hybrid systems, Journal of Engineering for Gas Turbines and Power, Vol. 126 (2004), pp. 516-523.

Magistri L., Trasino F., Costamagna P.,(2006), *Transient analysis of solid oxide fuel cell Hybrids - Part I: fuel cell models*, Journal of Engineering for Gas Turbines and Power, Vol. 128 (2006), pp. 288-293.

Mai A., Iwanschitz B., Weissen U., Denzler R., Haberstock D., Nerlich V., Schuler A. (2011), *Status of Hexis' SOFC Stack Development and the Galileo 1000 N Micro-CHP System*, ECS Transactions Solid Oxide Fuel Cells 12, Vol. 35 (2011), pp. 87-96.

Marra D., Pianese C., Sorrentino M., (2010), *Development of a model-based methodology aimed at detecting faults and degradation in SOFC systems*, Poster presented at FUEL CELLS Science & Technology 2010, 6 - 7 October 2010, Zaragoza, Spain.

Marra D., Pianese C., Sorrentino M. (2011), *Implementation of a Model-Based Methodology Aimed at Detecting Degradation and Faulty Operation in SOFC Systems*, ASME 9th International Conference on Fuel Cell Science, Engineering and Technology, Vol. 22 (2011), pp. 449- 455.

Massardo, A. F., Lubelli, F., (2000), *Internal Reforming Solid Oxide Fuel Cell - Gas Turbine Combined Cycles (IRSOFC-GT). Part A: Cell*

Model and Cycle Thermodynamic Analysis, ASME Transactions, Journal of Engineering for Gas Turbines and Power, Vol. 122 (2000), pp. 27-35.

Milewski J, Swirski K. (2009), *Modelling the SOFC behaviours by artificial neural network*. International Journal of Hydrogen Energy, Vol. 34 (2009), pp. 5546-5553.

Moran, M.J., Shapiro, H.N., (2004), *Fundamentals of Engineering Thermodynamics*, John Wiley and Sons, Hoboken, NJ (USA), pp. 681-683.

Nelles O. (2000), *Nonlinear system identification: from classical approaches to neural networks and fuzzy models*, 1st edn. Springer, Berlin.

Nørgaard M., Ravn O., Poulsen N. L., Hansen L. K., (2000), *Neural Networks for Modeling and Control of Dynamic Systems*, Springer-Verlag.

Okano K., (2003), *Hydrogen and Fuel Cell Activities in Japan*, path hydrogen in Mexico, February, 14, 2003 (http://www.conae.gob.mx/work/secciones/2112/imagenes/japan_path.pdf)

Ormerod R.M., (2003), *Solid oxide fuel cells*, Chemical Society Review, Vol. 32 (2003), pp. 17-28.

Patan K. (2008), *Artificial neural networks for the modelling and fault diagnosis of technical process*, Lecture notes in control and information Sciences, Springer, Vol. 377 (2008), p. 206.

Patterson, D. W. (1995), *Artificial Neural Networks - Theory and Applications*, Prentice Hall.

Pianese C., Rizzo G. (1996), *Interactive Optimization of Internal Combustion Engine Tests by means of Sequential Experiment Design*, Proceefings of the 3rd Biennal Joint Conference on 'Engineering Systems Design and Analysis - Esda, Petroleum Division of ASME, Montpellier, France, July 1 - 4 , ASME PD, Vol. 80 (1996), pp. 57 - 64.

Rajashekara K., (2000), *Propulsion System Strategies for Fuel Cell Vehicles*, SAE Paper 2000-01-0369.

Recknagle K.P., Williford R.E., Chick L.A., Rector D.R., Khaleel M.A. (2003), *Three-dimensional thermo-fluid electrochemical modelling of planar SOFC stacks*, Journal of Power Sources, Vol. 14 (2003), pp. 113-119.

Recupero V., Pino L., Leonardo R.D., Lagana M., Maggio G., (1998), *Hydrogen generator, via catalytic partial oxidation of methane for fuel cells*, Journal of Power Sources, Vol. 71 (1998), pp. 208-214.

Ripley B. D., (2000), *Pattern Recognition and Neural Networks*,

Cambridge University Press.

Rizzoni G., Pisu P., Scattolini R., (2008), *Fault Detection and Diagnosis in Mechatronic Systems*, Graduate Course (ME 874), Center for Automotive Research, The Ohio State University, http://car.eng. ohio-state.edu/node/98.

Sedghisigarchi K, Feliachi A., (2004 a), *Dynamic and transient analysis of power distribution systems with fuel Cells-part I: fuel-cell dynamic model*, Energy Conversion, IEEE Transactions, Vol. 19 (2004), pp. 423-428.

Sedghisigarchi K, Feliachi A., (2004 b), *Dynamic and transient analysis of power distribution systems with fuel Cells-part II: control and stability enhancement*, Energy Conversion, IEEE Transactions, Vol.19 (2004), pp. 429-434.

Selimovic A., Kemm M., Torisson T., Assadi M., (2005), *Steady state and transient thermal stress analysis in planar solid oxide fuel cells*, Journal of Power Sources, Vol. 145 (2005), pp. 463-469.

Singhal S.C., Kendall, K., (2004), *High Temperatures Solid Oxide Fuel Cells: Fundamentals, Design and Applications*, Elsevier Ltd, The Boulevard, Langford Lane, Kidlington, Oxford OX5 1GB, UK.

Sohlberg B., (2003), *Grey box modelling for model predictive control of a heating process*, Journal of Process Control, Vol. 13 (2003), pp 225-

238.

Sorrentino M., (2006), *Development of a Hierarchical Structure of Models for Simulation and Control of Planar Solid Oxide Fuel Cells*, Ph.D. Thesis, University of Salerno, Italy

Sorrentino M., Pianese C., (2011), *Model-based development of low-level control strategies for transient operation of solid oxide fuel cell systems*, Journal of Power Sources, Vol. 196 (2011), pp. 9036-9045.

Sorrentino M., Pianese C., (2009 a), *Control Oriented Modeling of Solid Oxide Fuel Cell Auxiliary Power Unit for Transportation Applications*, ASME Journal of Fuel Cell Science and Technology, Vol. 6 (2009), n.4.

Sorrentino M., Pianese C., (2009 b), *Grey-Box modeling of SOFC unit for design, control and diagnostics applications*, European Fuel Cell Forum, June 29-July 2009, Lucerne, Switzerland.

Sorrentino M., Pianese C., Guezennec Y.G., (2008), *A hierarchical modeling approach to the simulation and control of planar solid oxide fuel cells*, Journal of Power Sources, Vol. 180 (2008), pp. 380-392.

Topsoe, (2002), *Wärtsilä and Topsoe Start Co-operation in Fuel Cell Development*, news appeared on Topsoe website (www.topsoe.com), October 16th 2002.

Traverso A., (2005), *TRANSEO Code for the Dynamic Performance Simulation of Micro Gas Turbine Cycles*, ASME Conference Proceedings 2005, pp. 45-54.

Tu H., Stimming U. (2004), *Advances, aging mechanisms and lifetime in solid-oxide fuel cells*, Journal of Power Sources, Vol. 127 (2004), pp. 284-293.

Wang K.,Hissel D., Pera M.C., Steiner N., Marra D., Sorrentino M.,. Pianese C, Monteverde M., Cardone P., Saarinen J., (2011), *A Review on solid oxide fuel cell models*, International Journal of Hydrogen Energy, Vol. 36 (2011), pp. 7212-7228.

Weber A., Tiffée E.I., (2004), *Materials and concepts for solid oxide fuel cells (SOFCs) in stationary and mobile applications*, Journal of Power Sources, Vol. 127 (2004), pp. 273-283.

Witczak M., (2003), *Identification and Fault Detection of Non-Linear Dynamic Systems*, University of Zielona Góra Press, Poland.

Xue X., Tang J., Sammes N., Du Y., (2005), *Dynamic modeling of single tubular SOFC combining heat/mass transfer and electrochemical reaction effects*, Journal of Power Sources, Vol. 142 (2005), pp. 211-222.

Yakabe H., Ogiwara T., Hishinuma M., Yasuda I. (2001), *3-D model calculation for planar SOFC*, Journal of Power Sources, Vol. 54

(2001), pp. 102-144.

Yokokawa H., Tu H., Iwanschitz B., Mai A., (2008), *Fundamental mechanisms limiting solid oxide fuel cell durability*, Journal of Power Sources, Vol.182 (2008), pp. 400-412.

Zhang X, Li J, Li G, Feng Z., (2006), *Development of a control-oriented model for the solid oxide fuel cell*, Journal of Power Sources Vol. 160 (2006), pp. 258-267.

Zhu J., Zhang D., King K.D. (2001), *Reforming of CH_4 by partial oxidation: thermodynamic and kinetic analyses*, Fuel, Vol. 80 (2001), pp. 899-905.